Experimental and Numerical Analysis of Thermal Insulation Technologies for Automotive Diesel Engine Applications

Doctoral Dissertation
Doctoral Program in Energy Engineering (31st Cycle)

Experimental and Numerical Analysis of Thermal Insulation Technologies for Automotive Diesel Engine Applications

Sabino Caputo
* * * * * *

Supervisor
Prof. Federico Millo

Doctoral Examination Committee:
Prof. Michael Bargende, Universität Stuttgart
Prof. Nicolò Cavina, Università degli Studi di Bologna
Prof. Claudio Dongiovanni, Politecnico di Torino
Prof. Lucio Postrioti, Università degli Studi di Perugia
Prof. Bianca Maria Vaglieco, Istituto Motori - C.N.R.

Politecnico di Torino
June 19, 2019

I hereby declare that, the contents and organisation of this dissertation constitute my own original work and does not compromise in any way the rights of third parties, including those relating to the security of personal data.

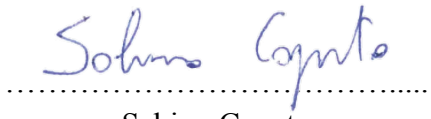

Sabino Caputo
Turin, June 19, 2019

Summary

The upcoming demanding targets in terms of CO_2 reduction and the increasingly stringent emission regulations are forcing the car manufacturers toward the adoption of innovative technologies left so far in the closet. In the future scenario, the diesel engine will still play a key role in the automotive market, especially for heavier applications, thanks to its higher efficiency respect to gasoline counterpart which can help to lower the average CO_2 emissions of the entire car fleet. Moreover, the estimated full electric cars penetration (only 21% in Europe by 2030 [1]) makes the diesel engine development fundamental for the remaining share of vehicles equipped by an internal combustion engine. Additionally, many cost-benefit analyses show that is more convenient to fully exploit the residual efficiency potential of combustion vehicles (including hybrid technologies) respect to transitioning immediately to fully electrified cars. Notwithstanding that, many obstacles (including NO_x and soot emissions, air quality regulations in metro-cities and diesel bans) are excluding diesel vehicles from the urban areas.

In this complex scenario, where CO_2 reduction technologies are becoming exponentially expensive, a high-priced solution, as engine thermal insulation, turns competitive, especially if combined with the exhaust aftertreatment systems on the new diesel engine generation. In particular, beyond the efficiency improvement, the thermal insulation technology can improve the aftertreatment system performance and accelerate the catalyst light-off, due to the produced higher exhaust gas temperature.

This *Thesis* investigates the potential of thermal insulation in reducing fuel consumption and CO_2 emissions of a 1.6 l automotive diesel engine.

The review on the state-of-the-art Thermal Barrier Coatings (TBCs), performed in collaboration with different Departments of Politecnico di Torino, has allowed

identifying a large number of mechanical, chemical and thermo-dynamical issues deriving from the technology. In addition to the traditional TBCs (i.e., ceramics), a new kind of coating (anodized aluminium), exploiting the thermal swing concept, has been studied.

Successively, numerical analysis, by utilizing a one-dimensional Computational Fluid Dynamics (CFD) engine simulation code, was carried out to investigate the most promising thermal insulation technologies for engine efficiency enhancement and heat loss reduction. The investigation of the complete and ideal insulation of the engine components (piston, firedeck, liner, and valves) has pointed out that piston insulation is the most efficient technology for improving efficiency and reducing heat transfer. Then, the numerical analysis has been addressed to the evaluation of the most efficient piston TBC, using a lumped-mass thermal model directly coupled with the engine model. The simulations have shown on average 0.8% in Brake Specific Fuel Consumption (BSFC) improvement and 5% in heat transfer reduction if a 100-μm-thick anodized aluminum TBC is used. The simulation outputs were successively used to set the guidelines for designing the theoretically most suitable piston coating, which was then tested on a real automotive application.

The last part of the *Thesis* focuses on the results of an experimental campaign carried out on a prototype automotive diesel engine, for evaluating the effects deriving from the use of full coated pistons, respect to the traditional ones (aluminum-made). Despite the promising potential for efficiency improvement highlighted by the numerical simulation, the experimental campaign has indicated a slight worsening of the engine efficiency (up to 2% at lower load and speed) adopting coated pistons. Moreover, the burn rate analysis has revealed that the coated configuration presents a slower mixing-controlled combustion phase, and a consequent combustion shift towards the late combustion, which are the leading causes of the indicated efficiency worsening. The higher surface roughness and porosity of the coating (R_a 8 μm of coating vs. R_a 3.2 μm of aluminium) are the critical factors for the combustion slowdown.

In conclusion, this research activity has led to the following outcomes:

- Piston results to be the component with the most significant potential in terms of heat transfer and BSFC reductions when it is thermally insulated. This result can be explained by the greater surface of the piston exposed to the in-cylinder gas during the combustion if compared with the other components. Furthermore, the combustion is intentionally directed towards the piston, causing higher turbulence and temperature near its surface and, consequently, a greater heat flux through this component.

- High coating surface roughness and porosity are detrimental for the engine efficiency and pollutant emissions (especially soot and unburned hydrocarbons). Surface roughness and porosity should therefore be reduced through an appropriate sealing of the coating pores.
- The use of TBC on the entire piston surface (including the bowl zone) can cause thermal efficiency worsening due to the interaction between the impinged fuel spray and the coating in case of increased surface roughness of the coating, therefore the use of TBC should be limited to the piston crown surface only.
- Thermal swing concept is fundamental for reducing the engine thermal losses without any penalties in term of volumetric efficiency and pollutant emissions. Thermal swing concept can be achieved with low-thermal-inertia and low-thermal-conductivity TBCs.

Acknowledgment

I would like to acknowledge General Motors – Global Propulsion Systems for sponsoring my PhD scholarship. I would also like to convey my gratitude to Mr. Giancarlo Cifali and Dr. Francesco C. Pesce for providing me their valuable suggestions. I would also like to express my sincere thanks to the Department of Mechanical and Aerospace Engineering (DIMEAS), Department of Applied Science and Technology (DISAT), Department of Management and Production Engineering (DIGEP) for their supports during the preliminary literary review analysis. Finally, I would also like to express my sincere thanks to the entire e^3 TEAM both for the precious technical help and for the good time spent together.

I would like to dedicate this thesis to my loving parents

Contents

1 Introduction 1
2 Engine thermal insulation review 10
2.1 Material properties 10
2.1.1 Material requirements 11
2.1.2 Yttria Stabilized Zirconia 13
Alternative stabilizers of Yttria in Zirconia 14
2.1.3 Mullite 14
2.1.4 SiRPA 15
2.2 Technological issues 18
2.2.1 Thermal spray process 18
Plasma spraying 19
High-Velocity Oxygen Fuel 19
2.2.2 Anodizing process 20
2.2.3 Time and cost of the processes 22
2.3 Low Heat Rejection Engines – Review 23
3 Numerical analysis on the Low Heat Rejection Engine technology 29
3.1 Engine model description 30
3.1.1 Case study 30
3.1.2 Simulation Matrix 31
3.1.3 Model validation 31
3.2 Ideal insulation of the engine components 32
3.2.1 Effects of Partial Insulation 35
3.3 Piston thermal barrier coatings 36
3.3.1 Anodized aluminum TBC 37
Effects of coating thickness 39
3.3.2 Yttria-Partially Stabilized Zirconia (Y-PSZ) TBC 41
4 Experimental analysis 43
4.1 Experimental setup 44

4.1.1 Engine layout 44
4.1.2 Facilities description 44
4.1.3 Tests description....46
4.2 Results and discussions....47
4.2.1 Injection timing effect....47
4.2.2 Exhaust gas recirculation effect 52
5 Conclusions 57
6 References 60
7 Appendix A 65
8 Appendix B....69

List of Tables

Table 2.1 - Thermal properties of YSZ and mullite at three different temperatures [19] 15
Table 2.2 - Thermo-physical properties of SiRPA at 500 K [17] 17
Table 2.3 - Anodizing process parameters [32] 21
Table 2.4 - Pore density vs. voltage with four different electrolytes [32] 21
Table 2.5 - Automotive Coatings Price Sheet. SOURCE: Swain Tech Coatings [34] 22
Table 3.1 – Engine specifications 31
Table 3.2 - Thermo-physical properties of anodized aluminum [17] and Y-PSZ [59] 41
Table 4.1 - Thermo-physical properties of the tested anodized aluminum 44
Table 4.2 - Instrumentation precisions and linearities 45
Table 4.3 – Test matrix 46

List of Figures

Figure 1.1 - Comparison of global CO_2 regulations for new passenger cars [2] 1
Figure 1.2 - Sales-weighted average type-approval CO_2 emissions from EU lower medium 2
Figure 1.3 - Diesel shares of new car registrations in France, Germany, Italy, Spain, and the UK [7] 3
Figure 1.4 – Average CO_2 emissions by market and fuel-type registered in 2018 (the data are NEDC correlated) [8].....4
Figure 1.5 - Key market vehicle sales prognosis 2030 (left), EU vehicle sales forecast (right) [1].....5
Figure 1.6 - Estimates of average fuel-saving potential of three technology routes for 5
Figure 1.7 – US share of Light Duty Vehicle sales (aggressive scenario) [9] ..6
Figure 1.8 - Estimated costs of emissions control technologies for European light-duty vehicle from Euro 4 to Euro 6 (assuming 1.5L 4-cylinder) [10] 6
Figure 1.9 - Comparison of rulemaking and ICCT/supplier estimates of direct manufacturing cost per percent fuel consumption reduction in 2025 [11].....7
Figure 1.10 - Additional costs (including direct and indirect manufacturing costs, excluding value added tax) of reducing the WLTP CO_2 emission of the average new car in 2030 relative to a 2013 baseline [12].....8
Figure 2.1 - Scheme of the general structure of a TBC with a qualitative temperature profile.....11
Figure 2.2 - Ashby map of thermal conductivity vs. linear thermal expansion coefficient (CTE) comparing the most suitable TBC materials 12
Figure 2.3 - Gas and wall temperature profiles during the engine cycle: conventional wall (blue line), conventional ceramic insulation coating (magenta line), temperature swing insulation coating (red line) and gas (black dotted line) 16
Figure 2.4 - Schemes of the general structure of SiRPA [16,17].....17
Figure 2.5 –Thermophysical properties of the most common TBC materials 18
Figure 2.6 - Schematic diagram of Atmospheric Plasma Spray [24].....19
Figure 2.7 - Schematic diagram of High-Velocity Oxygen Fuel [25] 20
Figure 2.8 – Expected process time and costs.....22
Figure 2.9 - p-V diagram around TDCF (left), Heat Release Rate (right). IP (Insulated Piston), SP (Standard Piston) [46] 25

Figure 2.10 - Apparent cumulative heat release of the steel piston and the YSZ piston at $\dot{m}_{fuel}$ = 54.1 mg/inj and λ = 3.2 [47] 26
Figure 2.11 - Temperature measurements around TDC at the bowl measurement location of the steel piston (left) and YSZ piston (right) for $\dot{m}_{fuel}$ = 54.1 mg/inj and λ = 3.2 [47] 26
Figure 2.12 – logP/logV diagram (left) and (ΔP-ΔP_{base})/V diagram (right) (ΔP=$P_{expansion}$-$P_{compression}$) [48]. 27
Figure 2.13 - Shape of piston cavity [50].....28
Figure 3.1 – Matrix of the simulated engine operating points 31
Figure 3.2 - Comparison of predictions and experimental data 32
Figure 3.3 – Maximum in-cylinder Heat Transfer reduction (top) and BSFC reduction (bottom) due to the component insulations 33
Figure 3.4 – Volumetric efficiency increment (top) and turbine inlet temperature variation (bottom) due to the component insulations 34
Figure 3.5 - In-cylinder heat transfer rate (top) and gas temperature (bottom) for baseline, piston insulation and valve insulation.....34
Figure 3.6 - Effects of insulation levels on the in-cylinder heat transfer.....35
Figure 3.7 - Correlations between in-cylinder heat transfer and BSFC for the different insulation strategies.....35
Figure 3.8 - Engine thermal model layout in GT-SUITE 37
Figure 3.9 - Piston wall temperature swings (baseline and anodized aluminum) 38
Figure 3.10 - Cycle-averaged piston wall temperature of baseline and anodized 38
Figure 3.11 - Effects of piston coating (100 μm - anodized aluminum) on....39
Figure 3.12 - Effects of piston coating thickness (anodized aluminum) on the in-cylinder heat transfer.....39
Figure 3.13 - Correlation between in-cylinder HT and BSFC reduction for anodized aluminum TBC.....40
Figure 3.14 - Piston wall temperature swings for different coating thicknesses 40
Figure 3.15 - Effects of piston coating thickness (anodized aluminum) on NO_x emissions.....41
Figure 3.16 - Piston wall temperature swings (anodized aluminum and Y-PSZ) 42
Figure 3.17 - In-cylinder Heat Transfer reductions (top) and BSFC reductions (bottom) in case of 100 μm anodized aluminum and Y-PSZ piston coatings 42

Figure 4.1 - Top views of the two piston configurations, after the experimental campaign 44
Figure 4.2 - Engine layout 45
Figure 4.3 - SOI sweep at 1500x5, 2000x8, 2750x12 and 2000x16. Average values over 5 tests performed on different days. Grey bands highlight the points which were analyzed through the burn rates 47
Figure 4.4 - Burn Rates at 1500x5, 2000x8, 2750x12 and 2000x16. Difference = PFC - BASE 48
Figure 4.5 - Burned Fuel Fraction at 1500x5, 2000x8, 2750x12 and 2000x16. Difference = PFC - BASE 49
Figure 4.6 – HC emissions as a function of the injection timing at 1500x5, 2000x8, 2750x12 and 2000x16. Average values over 5 tests performed on different days. Grey bands highlight the points which were analyzed through the burn rates 50
Figure 4.7 - NOx emissions as a function of the injection timing at 1500x5, 2000x8, 2750x12 and 2000x16. Average values over 5 tests performed on different days. Grey bands highlight the points which were analyzed through the burn rates 50
Figure 4.8 - Soot emissions as a function of the injection timing at 1500x5, 2000x8, 2750x12 and 2000x16. Average values over 5 tests performed on different days. Grey bands highlight the points which were analyzed through the burn rates 51
Figure 4.9 – Equivalence ratio by CFD simulations on a similar engine [58] 51
Figure 4.10 - CO emissions as a function of the injection timing at 1500x5, 2000x8, 2750x12 and 2000x16. Average values over 5 tests performed on different days. Grey bands highlight the points which were analyzed through the burn rates 52
Figure 4.11 - EGR sweep at 1500x5, 2000x8, 2750x12 and 2000x16. Average values over 5 tests performed on different days. Grey bands highlight the points which were analyzed through the burn rates 52
Figure 4.12 - Burn Rate at 1500x5, 2000x8, 2750x12 and 2000x16, w/EGR. Difference = PFC - BASE 53
Figure 4.13 – Burned Fuel Fraction at 1500x5, 2000x8, 2750x12 and 2000x16, w/EGR. 54
Figure 4.14 – ISNOx-ISHC trade-offs at 1500x5, 2000x8, 2750x12 and 2000x16. Average values over 5 tests performed on different days. Grey bands highlight the points which were analyzed through the burn rates 54

Figure 4.15 - $ISNO_x$-ISCO trade-offs at 1500x5, 2000x8, 2750x12 and 2000x16. Average values over 5 tests performed on different days. Grey bands highlight the points which were analyzed through the burn rates 55
Figure 4.16 - $ISNO_x$-ISSoot trade-offs at 1500x5, 2000x8, 2750x12 and 2000x16. Average values over 5 tests performed on different days. Grey bands highlight the points which were analyzed through the burn rates 55

Figure A.1 – Operating points selected for the DIPulse calibration 65
Figure A.2 - DIPulse combustion model results @ 5 different engine operating points – Experimental (black) and simulated (red) in-cylinder pressures (solid) and burn rates (dashed), injection mass flow rate (green dashed).....66
Figure A.3 - DIPulse combustion model results - Combustion parameters: IMEP (top-left), in-cylinder maximum pressure (top-right), crank angle of maximum pressure (bottom-left), crank angle at 50% fuel burned (bottom-right) (28 engine operating points).....67
Figure A.4 - DIPulse combustion model results – NOx emissions: all operating points (left) and low NOx zone (right) 68

Figure B.1 - Heat Transfer Coefficients (left) and Heat Transfer Rates (right) calculated with Flow and Woschni models 69
Figure B.2 - Piston wall temperature swings calculated with Flow and Woschni models.....70
Figure B.3 - BSFC benefits due to piston coating (100 μm - anodized aluminum) using Flow and Woschni models 70
Figure B.4 - Fraction of the piston heat loss respect to the total for the baseline condition 71

Abbreviations

0D	Zero Dimension
1D	One Dimension
3D	Three Dimensions
ACEA	European Automobile Manufacturers' Association
AFV	Alternative Fuel Vehicle
APS	Atmospheric Plasma Spray
ATDC	After Top Dead Center
BC	Bond Coat
BEV	Battery Electric Vehicle
BMEP	Brake Mean Effective Pressure
BSFC	Brake Specific Fuel Consumption
BTDC	Before Top Dead Center
CA	Crank Angle
CFD	Computational Fluid Dynamics
CHT	Conjugate Heat Transfer
CTE	Thermal Expansion Coefficient
DI	Direct Injection
DOC	diesel Oxidation Catalyst
DoE	Design of Experiment
DPF	diesel Particulate Filter
DT	Dwell Time
EC	European Commission
ECU	Engine Control Unit
EEA	European Economic Area
EGR	Exhaust Gas Recirculation
ET	Energizing Time
EU	European Union
FCEV	Fuel Cell Electric Vehicle
FSN	Filter Smoke Number
FSZ	Fully Stabilized Zirconia
HC	Hydrocarbons
HT	Heat Transfer
HEV	Hybrid Electric Vehicle

HP-ISFC	High Pressure - Indicated Specific Fuel Consumption
HP-EGR	High Pressure - Exhaust Gas Recirculation
HTC	Heat Transfer Coefficient
HVOF	High Velocity Oxygen Fuel
ICCT	International Council on Clean Transportation
ICE	Internal Combustion Engine
IMEP	Indicated Mean Effective Pressure
ISCO	Indicated Specific Carbon Monoxide
ISFC	Indicated Specific Fuel Consumption
ISHC	Indicated Specific Hydrocarbons
ISNOx	Indicated Specific NOx
ISSoot	Indicated Specific Soot
LCV	Light Commercial Vehicle
LDT	Light Duty Truck
LDV	Light Duty Vehicle
LHR	Low Heat Rejection
LHRE	Low Heat Rejection Engine
LP-EGR	Low Pressure - Exhaust Gas Recirculation
MFB	Mass Fraction Burned
MHEV	Mild Hybrid Electric Vehicle
MIIT	Ministry of Industry and Information Technology
MPV	Multi Purpose Vehicle
NEDC	New European Driving Cycle
OEMs'	Original Equipment Manufacturers'
PFC	Piston Full Coated
PGM	Platinum Group Metal
PHEV	Plug-in Hybrid Electric Vehicle
PHPS	Perhydropolysilazane
PI	Proportional Integral
PM	Particulate Matter
PSZ	Partially Stabilized Zirconia
R&D	Research & Development
RHCE	Retained Heat Conversion Efficiency
RMS	Root Mean Square
S&S	Start & Stop
SAE	Society of Automotive Engineers
SiRPA	Silica Reinforced Porous anodized Aluminium
SOI	Start of Injection
SUV	Sport Utility Vehicle

TBC	Thermal Barrier Coating
TC	Top Coat
TDC	Top Dead Center
TDCF	Top Dead Center Firing
TGO	Thermally Grown Oxide
TPM	Total Particulate Matter
UK	United Kingdom
VGT	Variable Geometry Turbine
VOF	Volatile Organic Fraction
WLTP	Worldwide harmonized Light vehicle Test Procedure
Y-PSZ	Yttria - Partially Stabilized Zirconia
YSZ	Yttria Stabilized Zirconia
ZLEV	Zero-and Low-Emission Vehicle
ZPS	Zirconia Plasma Spray

Chapter 1

Introduction

In the worldwide context, the European Union (EU) has traditionally been a leader in legislating CO_2 emission targets for the transportation sector. However, in recent years, the most important economies are setting new converging targets for new passenger vehicles [2]. Figure 1.1 shows a comparison of the worldwide CO_2 emission targets from 2000 until the next 2030. All the emission values are converted to the New European Driving Cycle procedure. Following the EU's 2020/21 target of 95 g CO_2/km, the United States (with 99 g CO_2/km by 2025), South Korea (with 97 g CO_2/km by 2020) and Canada (with 99 g CO_2/km by 2025) have enacted comparable targets. The European Commission's proposal for 2030 CO_2 standards makes the EU as the only market with 2030 goals.

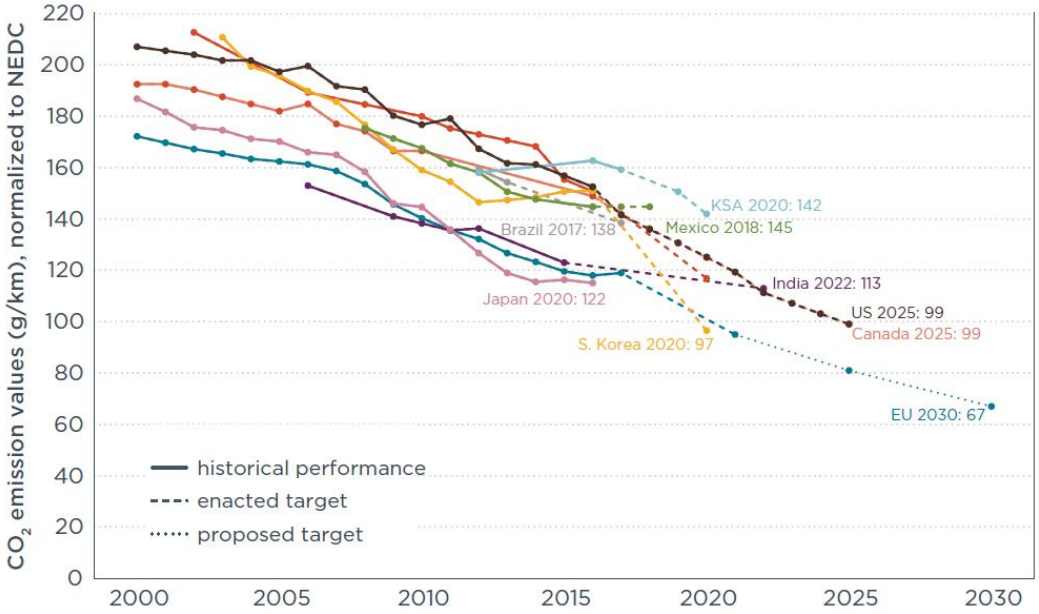

Figure 1.1 - Comparison of global CO_2 regulations for new passenger cars [2]

Moreover, in its "Made in China 2025" strategic initiative (MIIT, 2015), China government set a fleet efficiency target of 4 l/100 km (gasoline equivalent) for

passenger cars, reducing the 5 l/100 km goal for 2020. In the Technology Roadmap for Energy Saving and New Energy Vehicles, published by Society of Automotive Engineers of China (SAE China, 2016), the CO_2 target was decreased until 3.2 l/100 km by 2030 [3].

Figure 1.2 displays the sales-weight average type-approval CO_2 emissions for the European lower-medium vehicle segment: the blue line represents the gasoline vehicle, the red line represents the diesel vehicle, while the purple one represents the hybrid electric vehicle. Furthermore, the pie charts indicate the annual market share of the analysed vehicle segment. The market penetration of diesel vehicles has been continuously growing from 2001 to 2015, helping the car manufacturers in achieving the European CO_2 target on the entire vehicle fleet.

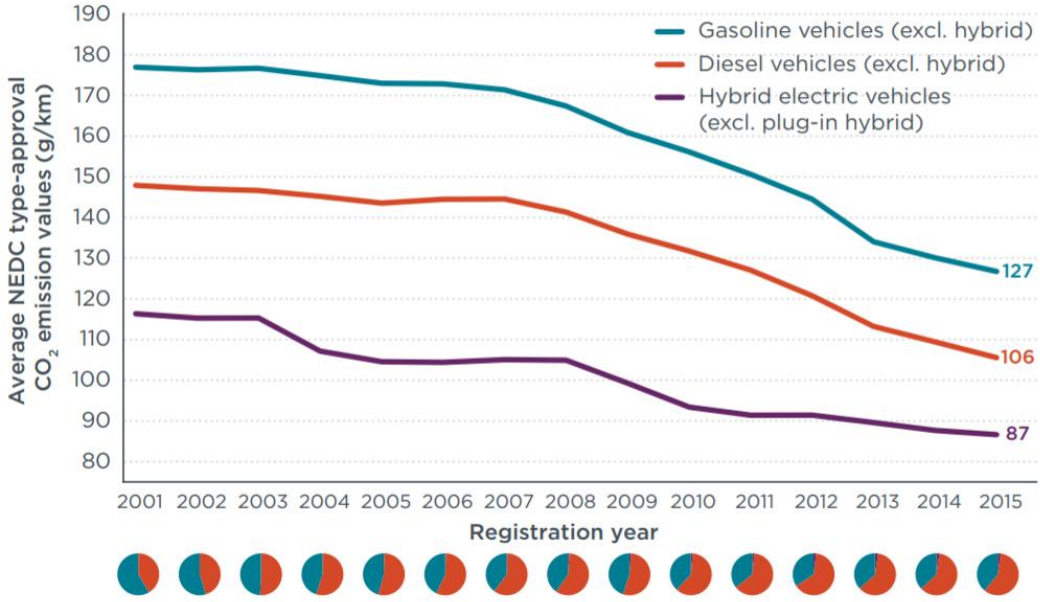

Figure 1.2 - Sales-weighted average type-approval CO_2 emissions from EU lower medium passenger cars by fueling technology. Pie charts indicate the market share of gasoline, diesel and, hybrid vehicles in each year [4]

After the so called "Dieselgate" (September 2015) the diesel shares of new vehicle registrations in Europe started to decrease, as shown in Figure 1.3. Combining the five bigger automotive European markets, diesel shares reduced by about 8 % since Dieselgate until the end of 2017. Diesel share in Germany lost about one-third of car registrations in December 2017, while in the UK about 38% in the same month. France has seen a steady decreasing in diesel sales since 2012, while Spain has shown the most significant drop in the five countries (16%) since Dieselgate broke. Although diesel sales in Italy were still growing during the 18 months after the Dieselgate, they seem to have flattened off in 2017.

The direct effect of diesel market decrease was an increase in CO_2 emissions, observed in 2017, for the first time since 2010 [5,6]. The European Automobile Manufacturers' Association (ACEA) Secretary General, Erick Jonnaert said *"As the European Economic Area (EEA) data show, the shift from diesel to petrol – together with the relatively low market penetration of alternative powertrains – is now having a tangible impact on the CO_2 performance of Europe's new car fleet"*.

In particular, the main outlines of the EEA can be summarized in the following points [5]:

- The average CO_2 emission of the cars sold in 2017 is 118.5 g/km, 0.4 g/km higher compared to 2016.
- For the first year since monitoring started, petrol cars were the most sold vehicles in the EU, with about 53% of sales, while diesel cars accounted for 45% of the new registrations. Diesel market decreased in all EU Member States except Italy (+0.6%) and Denmark (+6.9%). The countries with the greater diesel market in 2017 were Ireland (65%), Portugal (61%) and Italy (56%).
- The difference between average fuel efficiency of petrol cars (121.6 gCO_2/km) and diesel vehicles (117.9 gCO_2/km) reduced in 2017. In particular, diesel car efficiency decreased in 2017, compared to 2016 (116.8 gCO_2/km).

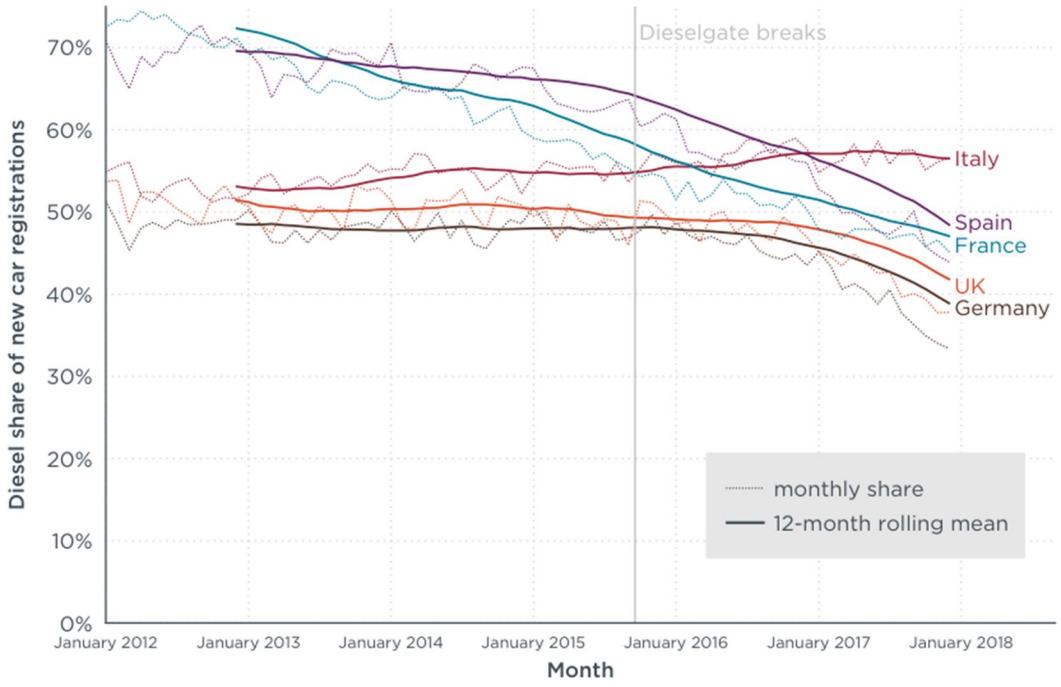

Figure 1.3 - Diesel shares of new car registrations in France, Germany, Italy, Spain, and the UK [7]

Moreover, EEA stated that the market penetration of plug-in hybrid electric vehicles (PHEVs) and battery-electric vehicles (BEVs) is still low (1.5%), although it was increased in 2017 (+ 42%).

The scenario is not different if we look at diesel car shares and CO_2 emissions registered in 2018 [8]. The analysis carried out by JATO Dynamics shows that CO_2 emissions, deriving from the European car market, increased by 2.4 g/km in 2018, reaching the highest average level of the last four years. At the same time, the diesel car registrations fell by 18% in 2018, reaching 36% of the total sales. Felipe Munoz, JATO's global analyst, commented, *"The positive effect of diesel cars on emissions has faded away as their demand has dropped dramatically during the last year. If this trend continues and the adoption of alternative fueled vehicles doesn't*

accelerate, the industry will need to take more drastic measures in order to meet the short-term targets".

The correlation between the decline in demand for diesel cars and the increase in CO_2 emissions was most evident when analyzing the data by country (Figure 1.4). Only three states saw improvements in CO_2 emissions: Norway, Netherlands and, Finland. In Norway, the growing popularity of electric and hybrid cars (57% market share) is massive enough to absorb the drop posted by diesel cars (-28%). In Netherlands, the improvement is due to an increase in demand for Alternative Fuel Vehicles – AFVs (+74%) which counted for 11% of the total market. The worst performance is seen in the UK, which has carried out one of the most aggressive campaigns against diesel [8].

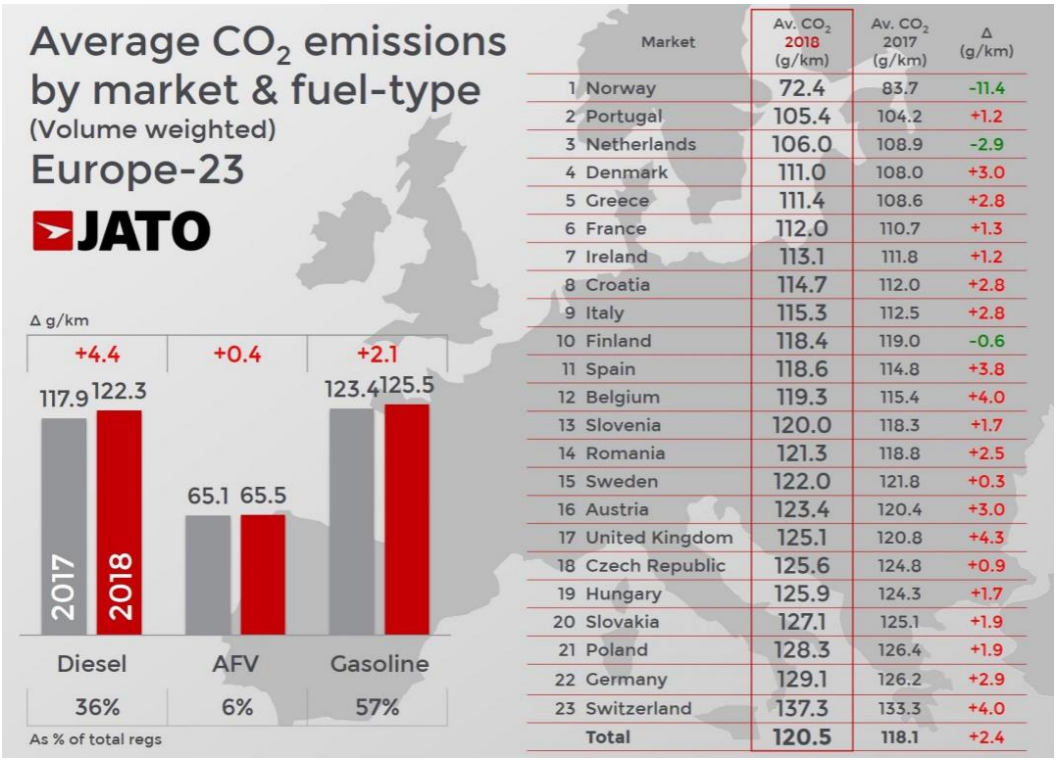

	Market	Av. CO_2 2018 (g/km)	Av. CO_2 2017 (g/km)	Δ (g/km)
1	Norway	72.4	83.7	-11.4
2	Portugal	105.4	104.2	+1.2
3	Netherlands	106.0	108.9	-2.9
4	Denmark	111.0	108.0	+3.0
5	Greece	111.4	108.6	+2.8
6	France	112.0	110.7	+1.3
7	Ireland	113.1	111.8	+1.2
8	Croatia	114.7	112.0	+2.8
9	Italy	115.3	112.5	+2.8
10	Finland	118.4	119.0	-0.6
11	Spain	118.6	114.8	+3.8
12	Belgium	119.3	115.4	+4.0
13	Slovenia	120.0	118.3	+1.7
14	Romania	121.3	118.8	+2.5
15	Sweden	122.0	121.8	+0.3
16	Austria	123.4	120.4	+3.0
17	United Kingdom	125.1	120.8	+4.3
18	Czech Republic	125.6	124.8	+0.9
19	Hungary	125.9	124.3	+1.7
20	Slovakia	127.1	125.1	+1.9
21	Poland	128.3	126.4	+1.9
22	Germany	129.1	126.2	+2.9
23	Switzerland	137.3	133.3	+4.0
	Total	120.5	118.1	+2.4

Figure 1.4 – Average CO_2 emissions by market and fuel-type registered in 2018 (the data are NEDC correlated) [8]

The limited BEV and PHEV penetrations in the automotive market make diesel engine still competitive for the short-term future. Diesel powertrain can still play a key role in the Original Equipment Manufacturers' (OEMs') strategies to meet the future CO_2 targets because the modern diesel engines keep the thermal efficiency advantage with respect to the gasoline counterpart, even though the more complex exhaust gas aftertreatment systems. If the time horizon is postponed to the next 10-15 years, the car sale shares may change due to the greater BEVs and PHEVs market penetration.

As shown in Figure 1.5, FEV forecasts of passenger car sales in China, USA and Europe for 2030 indicate that the share of vehicles equipped with an internal combustion engine (S&S, MHEV, HEV, PHEV) will remain still considerable, while a shift from diesel to gasoline hybrids and, then, to BEV's is predictable for the small car segment. The European vehicle sales forecast states that diesel engine

will equip 25% of cars, especially for heavier applications (Sport Utility Vehicle – SUV, Light Commercial Vehicle – LCV, Multi-purpose Vehicle – MPV, Light Duty Truck – LDT).

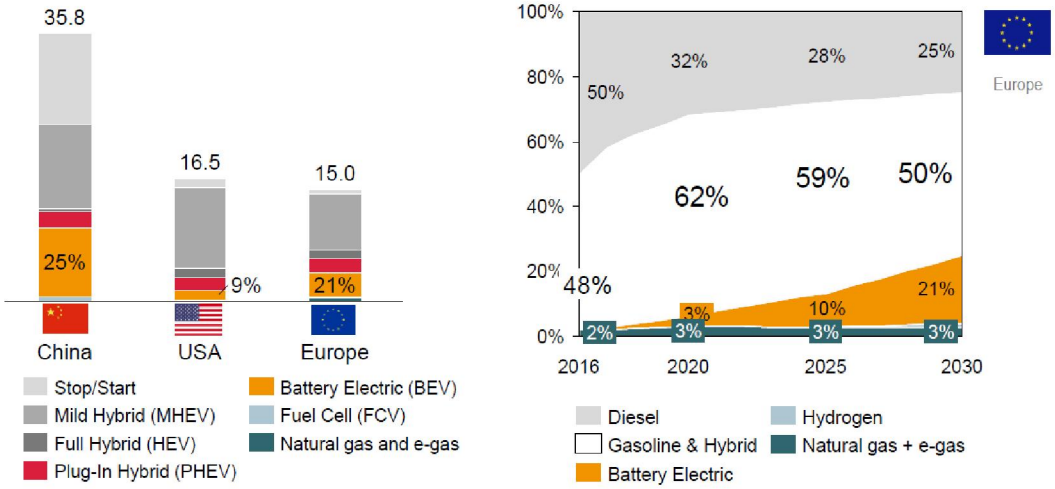

Figure 1.5 - Key market vehicle sales prognosis 2030 (left), EU vehicle sales forecast (right) [1]

In the Chinese automotive market, which is expected to be the biggest one by 2030, higher percentages of small and mild hybrid vehicles will still be sold in the future. In these market shares, the use of high-efficiency diesel engines is fundamental for reaching fuel consumption targets. As discussed in the ICCT report [3] and illustrated in Figure 1.6, the development of ICE is crucial for achieving the Chinese post-2020 standards for light-duty vehicles (LDVs), even more than hybrid electrification [3].

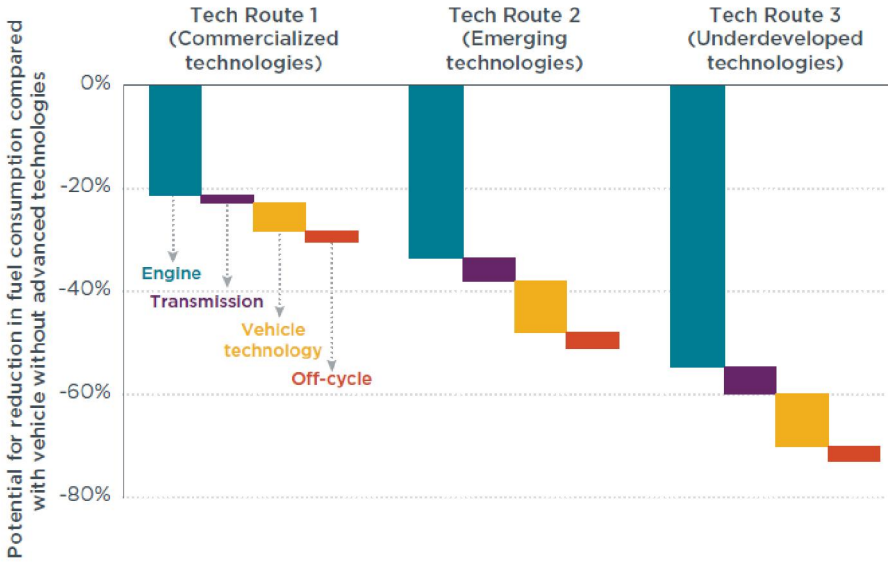

Figure 1.6 - Estimates of average fuel-saving potential of three technology routes for conventional passenger cars in China by technology type [3]

The same considerations are valid for the US market, as confirmed from the analysis performed by Fuels Institute [9] and reported in Figure 1.7. Despite the poor penetration of diesel engines in the US automotive market, the diesel share of LDV sales will remain constant until 2025, even in the aggressive scenario.

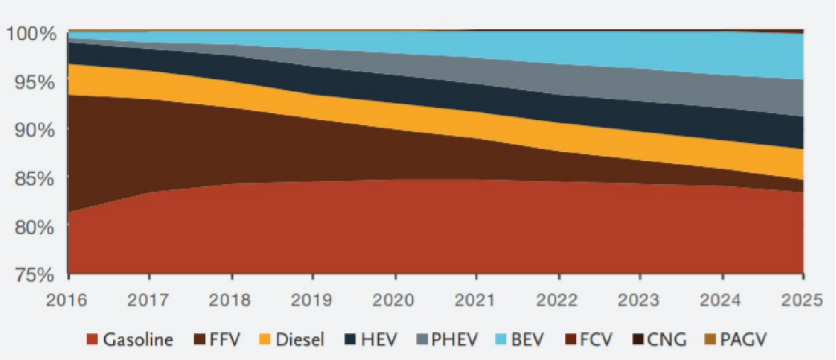

Figure 1.7 – US share of Light Duty Vehicle sales (aggressive scenario) [9]

Another critical variable to consider for future diesel engine generation is the manufacturing cost. Diesel engines are more expensive to manufacture than gasoline engines because of the need for increased structure to contain higher combustion pressures and because of their more-sophisticated, and higher-pressure, fuel injection systems. Also, diesel's particulate and nitrogen oxide (NO_x) emissions are more costly and more difficult to control.

Figure 1.8 shows the costs of the emissions control technologies from Euro 4 to Euro 6: the impact of the aftertreatment systems cost on the total has continually increased, while the prices for the engine-out emission control and R&D remained constant.

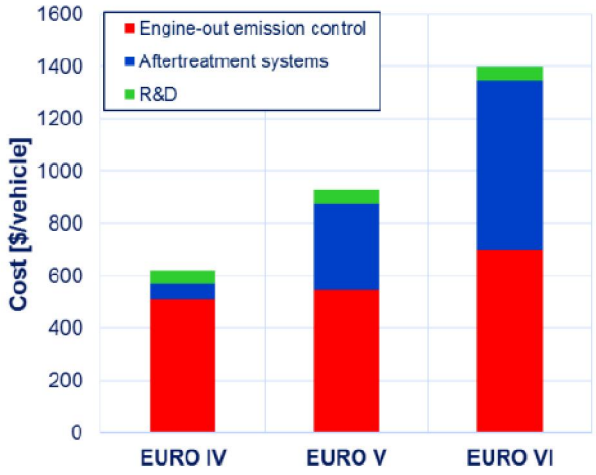

Figure 1.8 - Estimated costs of emissions control technologies for European light-duty vehicle from Euro 4 to Euro 6 (assuming 1.5L 4-cylinder) [10]

Because of the cost and complexity of currently available aftertreatment systems and future requirements for pollution reductions, diesel engines may be best suited for larger vehicle types. In the bigger classes, diesels' fuel economy benefits per incremental cost are comparable to, or better than, those of full hybrids.

Figure 1.9 compares the costs and benefits of advanced dieselization as estimated in the rulemaking (red box) with more recent calculations by suppliers (blue box). The rulemaking's cost-benefit analysis for the full hybrid is shown for reference. Future diesels are expected to cost less and have more significant benefits than forecast. The costs are lower because of less expensive emission control

systems, characterized by smaller amounts of Platinum Group Metals (PGMs), and improved engine components. Adding the costs and benefits of a 48V mild hybrid system and electric supercharging (orange box) leads to slightly higher prices per percent reduction in fuel consumption, but average total prices remain lower than for full hybrids. Cost reductions will improve diesels' competitiveness and may increase their market share in the future [11].

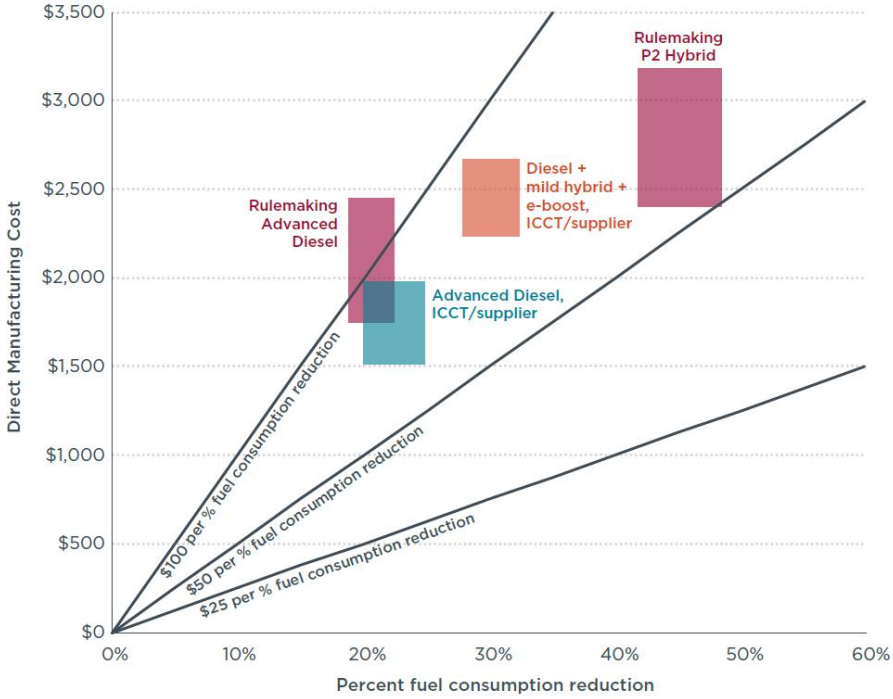

Figure 1.9 - Comparison of rulemaking and ICCT/supplier estimates of direct manufacturing cost per percent fuel consumption reduction in 2025 [11]

Moreover, looking at the ICCT plot shown in Figure 1.10, investments on ICE technologies (including hybridization) still prove to be advantageous to achieve the European 2030 goals, especially for car fleet average CO_2 reductions lower than 50% respect to 2013 baseline (126.8 gCO_2/km). Figure 1.10 reports three cost-benefit analysis, performed by the European Commission (EC), Ricardo and ICCT. The shape of the cost curves is similar: initially, conventional combustion engine vehicles are equipped with CO_2 reduction technologies with associated costs increase exponentially. When the CO_2 reduction potential of combustion vehicles is fully exploited (typically after all cars are equipped with full hybrid technology in combination with light-weighting and other measures), further CO_2 reductions can be achieved by deploying an increasing share of electrified vehicles (PHEVs, BEVs, and FCEV).

It is possible to reduce the compliance cost for intermediate CO_2 reduction targets by not fully exploiting the remaining efficiency potential of combustion vehicles and instead transitioning to electrified cars earlier. For some scenarios, the EC assumes a 2030 market share of electric vehicles of around 20% for passenger cars, which helps to reduce overall compliance costs but is still below the 30% ZLEV (zero-and low-emission vehicles) target for the same year. For its standard scenario though, the EC assumes a market share of electric vehicles of about 9% by

2030. The ZLEV targets essentially provide tolerance on the CO_2 targets (by up to 5%) for any OEM that reaches 15% electric vehicles in 2025 or 30% in 2030 [12].

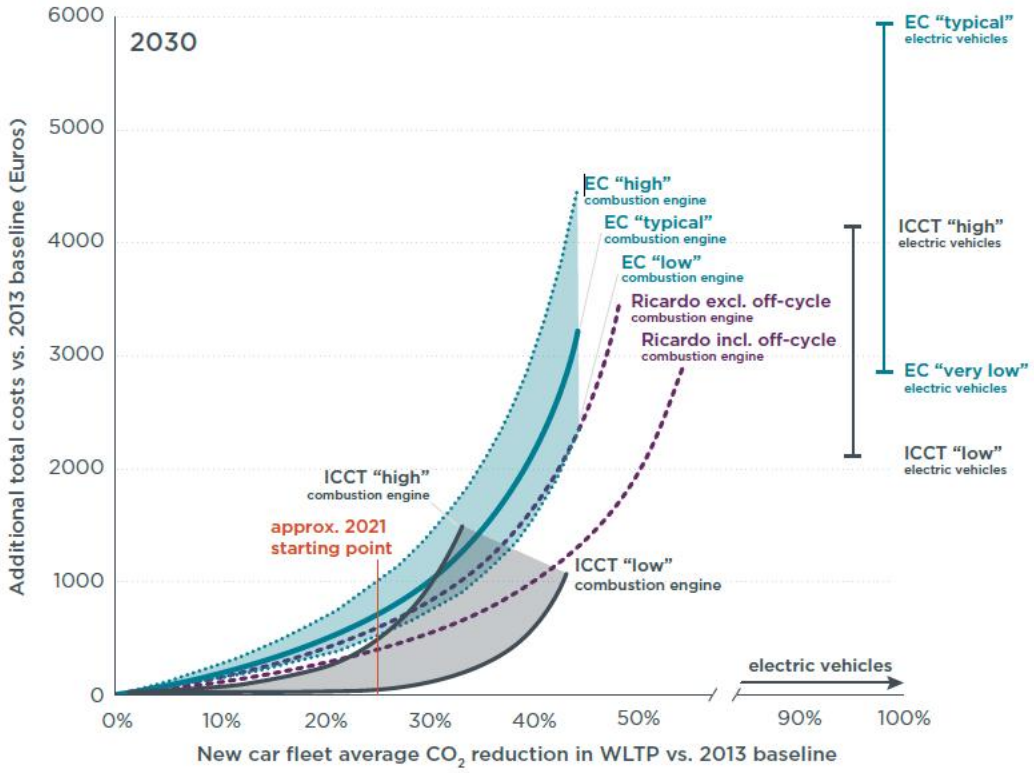

Figure 1.10 - Additional costs (including direct and indirect manufacturing costs, excluding value added tax) of reducing the WLTP CO_2 emission of the average new car in 2030 relative to a 2013 baseline [13]

In this very complicated scenario, the OEMs are pushing toward the adoption of more expensive engine technologies left so far in the closet, including engine thermal insulation. The idea of the so-called Low Heat Rejection Engines (LHREs), namely engines with reduced in-cylinder heat losses, is not new, since it was already introduced in the 80's to improve the internal combustion engine efficiency. In the past, LHREs were made by covering the combustion chamber surfaces (i.e., pistons, valves, ports) with ceramic materials, such as zirconia and silicon nitride, which present lower thermal conductivity than the conventional metals, and thereby can operate at higher temperatures, insulating the engine. The introduction of this concept on the engines in series production arose many issues, including cost, which limited this technology only to the research field.

Nowadays, the idea of repurposing the Low Heat Rejection technology, coupled with the aftertreatment systems, on the new generation of diesel engines can lead to benefits in terms of fuel consumption and emissions. Besides reducing CO_2 emissions, the insulation technologies can improve the aftertreatment performance and accelerate the catalyst light-off, due to the higher exhaust gas temperature. In addition, further improvements in fuel economy and emissions could be achieved by combining LHRE with new engine calibration strategies, exploiting the reduced need for catalyst heating thanks to the higher exhaust gas temperatures.

This *Thesis* is mainly focused on the effects of TBC technology on the engine efficiency and the pollutant emissions, leaving the possibility to exploit the increased exhaust gas temperatures combined with appropriate engine recalibrations for a future activity.

After this *Introduction*, in the *Second Chapter*, a review of the most effective engine thermal insulation technologies is given, from different perspectives (materials, production processes, energy, etc.).

The *Third Chapter* presents a preliminary analysis, through one-dimensional CFD engine simulations, on the potential of the combustion chamber insulation for a 1.6 l diesel engine for automotive applications.

Then, in the *Fourth Chapter*, the most promising insulation technology was selected using the simulation outputs, and, then, tested on a real engine application, utilizing a dyno test bench.

Finally, in the *Conclusions* section the main findings have been summarized.

Chapter 2

Engine thermal insulation review

One of the crucial tasks in current engine design is to ensure adequate cooling of combustion chamber surfaces even at the highest thermal loadings, i.e., at the rated power, controlling the amount of engine heat transfer. The consequence is that a considerable amount of fuel energy is wasted, reducing the engine indicated efficiency and the exhaust gas enthalpy. In diesel engines, the heat transfer from combustion chamber gasses typically ranges from 16% to 35% depending on the operating conditions [14]. One effective way to reduce the rate of in-cylinder heat rejected could be to increase the in-cylinder wall temperatures from the current values, near 500 K, to well over 1000 K [14]. Since the current levels of in-cylinder heat transfer are close to the lowest values achievable with typical metal engine parts, the use of high-temperature materials (i.e., ceramics), which need a lower amount of cooling, is necessary to obtain significant insulation results.

Insulating materials have been widely adopted in the past as TBCs mainly for research purposes. However, the introduction of these materials on the engines in series production arises a large number of material and production issues, including:

1. material strength, toughness, and stability at elevated temperature;
2. fatigue due to high cyclical thermal stress;
3. thermal expansion differences between the coatings and metallic materials;
4. impact on production process and cost.

In this *Chapter*, all these aspects will be analysed and discussed, reviewing different articles and papers published in literature, while the last part of the *Chapter* is focused on the thermo-fluidodynamic effects of thermal insulation on engine performance, efficiency, and emissions.

2.1 Material properties

A TBC is a particular superficial coating able to protect the metallic substrate against the thermal loads produced in high-temperature applications, the oxidation, and the hot corrosion.

Usually a TBC structure presents a thick ceramic layer called Top Coat (TC), which has a very low thermal conductivity and so acts as a thermal insulator element, and an intermediate metal alloy layer, called Bond Coat (BC), which is thinner than the TC and is used to reduce the difference of the linear Thermal Expansion Coefficient (CTE) between the metal substrate and the ceramic part of the coating.

The TC structure is typically characterised by a high porosity that drastically reduces the thermal conductivity and the elastic modulus of the layer, making it more compliant and able to accommodate the strains due to the thermal gradients. Conversely, the high porosity can allow the diffusion of the oxygen and the corrosive species towards the metal substrate, causing its oxidation. Therefore, another BC function is the protection of the substrate: the bond coat alloy is typically rich in Cr and Al, which form a passivation oxide at the TC/BC interface, called Thermally Grown Oxide (TGO). The scheme of the above described general structure of a TBC is reported in Figure 2.1.

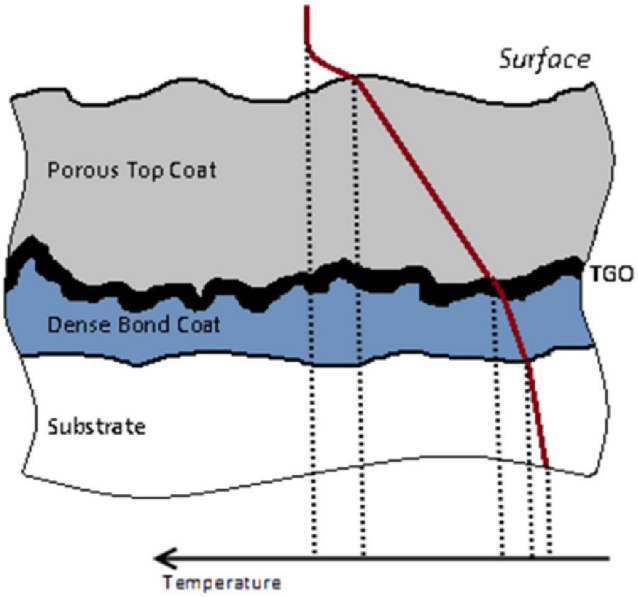

Figure 2.1 - Scheme of the general structure of a TBC with a qualitative temperature profile

Two different failure modes can occur in a TBC. The first one is due to the stresses deriving from high thermal gradients along the top coat and the stresses resulting from the CTE mismatch between the top and bond coats. These stresses can cause crack propagations and delamination of the coating. The second failure source is a consequence of the stress that forms for the excessive growth of the TGO. However, in the thicker coatings, like those used in the majority of the automotive applications, the temperature at the TC/BC interface is low enough to give a negligible TGO growth, and the first failure mode is the most critical.

2.1.1 Material requirements

The bond coat is usually made by a metallic Cobalt-based (CoNiCrAlY) or Nickel-based (NiCoCrAlY) superalloy, which contain Chromium and Aluminum elements, useful for the TGO formation at the TC/BC interface, and Yttrium to facilitate the adhesion of the TGO layer to the bond coat.

The top coat is often constituted by a ceramic material that is able to fulfill the following requisites:

1. high melting point;
2. chemical stability (avoid reactions);

3. phase stability (avoid phase transformations);
4. low thermal conductivity;
5. low heat capacity;
6. good thermomechanical properties;
7. good adherence to the BC;
8. low sintering rate;
9. toughness;
10. hardness and good resistant to erosion wear.

As above said in the automotive applications, where thicker TBCs are used, the differences in linear Thermal Expansion Coefficients (CTE) between the top/bond coats and bond coat/substrate are fundamental for the internal stress formation. In particular, a high CTE of the bond coat can reduce the mismatch in the thermal expansion with the metallic substrate, reducing the interfacial stress; but, if the thermal gradient along the thickness is high, the differential dilatation causes a stress profile inside the coating.

In the automotive research, zirconia (ZrO_2) has been the most extensively employed material, in particular with a yttria content of about 7-8% by wt., obtaining the so-called Yttria Stabilized Zirconia (YSZ).

Other materials, as the refractory mullite and the pyrochlore, were taken into consideration by recent researches [15,16] as valid alternatives to YSZ. Furthermore, perovskites, layered perovskites, hexaluminates, quasicrystals and other materials with very complexes structures are currently under investigation at a research level thanks to their low thermal diffusivity. In Figure 2.2, these materials are reported in the Ashby map and compared with the CTE ranges (vertical bands) of the most common substrates and bond coats.

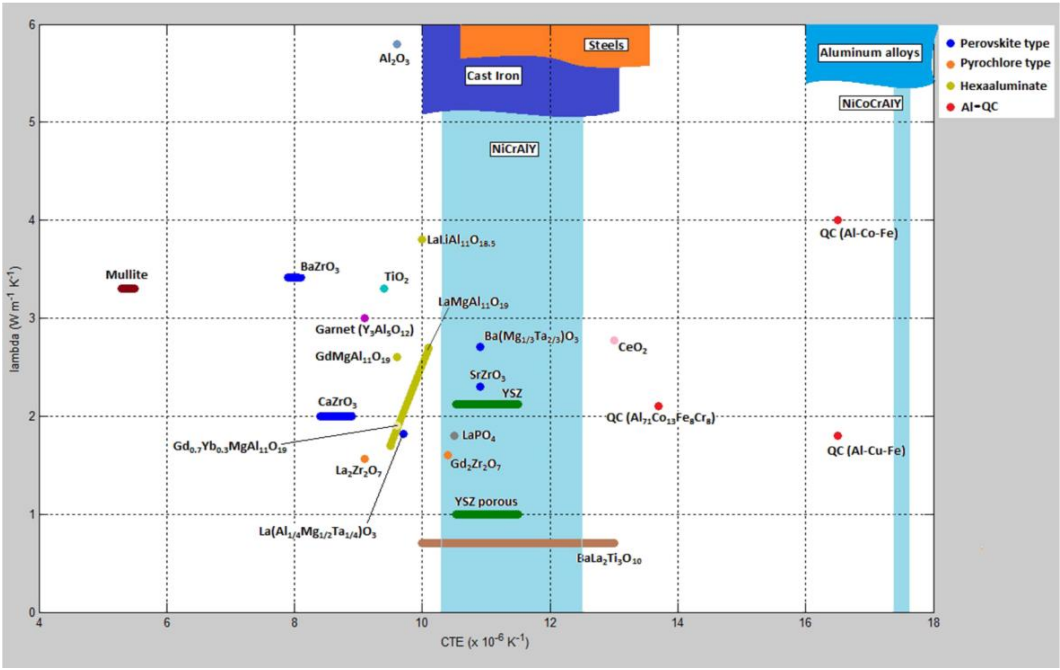

Figure 2.2 - Ashby map of thermal conductivity vs. linear thermal expansion coefficient (CTE) comparing the most suitable TBC materials

In addition to traditional TBCs, a new kind of coatings for automotive applications, based on the so called “thermal swing” concept was recently studied. In particular, this concept consists in the reduction of the temperature difference between the gas and the coated surfaces during the entire engine cycle, decreasing the engine thermal losses. In order to exploit the thermal swing concept, the TBC must have a very low thermal inertia and conductivity to be able to heat and cool very quickly following the gas temperature.

One well known material compliant with these characteristics is Silica Reinforced Porous Anodized aluminium (SiRPA), developed by Toyota [17,18]. The features and microstructure of SiRPA will be discussed in *Section 2.1.4*.

2.1.2 Yttria Stabilized Zirconia

Zirconia is the most widely adopted material in engine thermal insulation research field. It is a ceramic material made by a solid solution of zirconium oxide (ZrO_2) with a certain amount of dissolved doping elements, usually Magnesium (Mg), Calcium (Ca) or Yttrium (Y).

Zirconia is a polymorphic material because it can exist in three different crystal structures: monoclinic (m), tetragonal (t) and cubic (c). The monoclinic structure is stable from room temperature until 1170 °C, the tetragonal is stable until 2370 °C, and the cubic one is stable up to the material melting point (2690 °C). The function of the dopants (or stabilizers) is to stabilize or meta-stabilize the high-temperature structures even at room temperature avoiding the so-called martensitic transformation in the monoclinic phase which is characterized by a volume increment. Fully Stabilized Zirconia (FSZ) has a dopant quantity too high to stabilize the material, therefore Partially Stabilized Zirconia (PSZ) is more frequently employed. The martensitic transformation (t→m) can also occur with external stress (typically a mechanic load) which cause an unusual high fracture toughness of PSZ.

Yttria (Y_2O_3) is more used for the zirconia stabilization respect to the other dopants (magnesia, calcia, etc.) because it is a more efficient stabilizer and the quantities required for the process are lower. The characteristics of Yttria Stabilized Zirconia (YSZ) are high fracture toughness, low thermal conductivity, and relatively high CTE, closer to that of the metallic substrate. Besides, YSZ cannot be used in the applications that require temperatures higher than 1200 °C, because of the destabilization of the material and the consequent internal stress formation. In particular, the thermally sprayed YSZ coating is constituted by a tetragonal metastable phase (t’) that is formed from the non-diffusive transformation of the cubic phase due to the fast cooling of the splat. At high temperatures (from about 1200 °C) the t’ phase decomposes into a cubic phase c with high yttria content and in a tetragonal phase t with low yttria content. The latter has less dissolved stabilizer and so, can transform in monoclinic phase (martensitic transformation) when the temperature falls down. Moreover, the presence of impurities, as silica, also in small quantities (below 1% by wt.), can strongly reduce the YSZ performance, because they dissolve yttria with consequent destabilization.

In diesel engine applications, where thick coatings are employed, the failure mechanisms are typically triggered by the stress relaxation due to the creep deformation at high temperature [19,20]. Other usual failure mechanisms of the material are related to the sintering, that reduces the thermal conductivity, increases the stiffness and can cause shrinkage cracks. Therefore, the tensile stress along the YSZ top coat depends by complex interactions between thermal fatigue, sintering, creep and destabilization phenomena.

An optimization study of a thermal barrier of ZrO_2 – 8% by wt. Y_2O_3 on an aluminium alloy substrate is reported in the literature [21]. The authors indicated an optimal thickness of 300 μm of TC and 150 μm of BC.

Alternative stabilizers of Yttria in Zirconia

The conventional YSZ cannot be used above 1100 – 1200 °C due to the destabilization issues described in the previous paragraph. Alternative or adjuvant materials are currently studied to overcome these limitations.

The scopes of the alternative stabilizers are:

- reduce the intrinsic thermal diffusivity of the material;
- reducing the sintering rate at high temperature;
- enhance the stability, preventing the decomposition of the t' phase at high temperature.

The most studied alternative materials are lanthana La_2O_3 and Rare Earth Oxides (REO) (in particular, the lanthanides between cerium and ytterbium).

2.1.3 Mullite

Mullite is a stable intermediate compound of alumina and silica with stoichiometry $3Al_2O_3 \cdot 2SiO_2$. It is a stable refractory material that may be an attractive alternative solution to the zirconia TBC in diesel engine applications, where the temperatures are not extreme (differently from gas turbines), but the temperature gradient inside the coating may be high. In comparison with YSZ, mullite has a lower Thermal Expansion Coefficient and a higher thermal conductivity. The very low CTE leads to a higher thermal expansion mismatch with the metal substrate but also allows to strongly reduce the stresses due to the thermal gradient generated throughout the layer. In a diesel engine, the latter feature is decisive because the coating thicknesses are greater and the stresses generated can cause failures. Furthermore, the higher thermal conductivity of the material requires thicker top coat respect to YSZ to ensure the same thermal resistance. The thermal properties of YSZ and mullite are reported in Table 2.1.

The main reason that makes mullite a very suitable alternative to YSZ is its superior resistance to creep, that, as seen in *Section 2.1.2*, is the primary cause of superficial traction tensions and damages of zirconia [19,22]. The greater creep resistance gives to the mullite coatings a better thermal shock resistance and a more

prolonged thermal fatigue life than the YSZ in the operating conditions of diesel engine components.

Table 2.1 - Thermal properties of YSZ and mullite at three different temperatures [20]

	T [°C]	Thermal conductivity [$Wm^{-1}K^{-1}$]	Specific heat [J/mol K]	CTE [$x10^{-6}$ K^{-1}]
YSZ	27	0.67	420	7.5
	727	0.58	547	9
	1227	0.56	569	9.7
Mullite	27	1.32	838	5.1
	727	1.32	1202	5.2
	1227	1.34	1219	5.5

Thermally sprayed mullite tends to form an amorphous glass-like phase, due to its fast cooling, that then crystalizes after the exposure to temperatures between about 750 °C to 1000°C with consequent volume shrinkage and generation of internal stresses. This characteristic reduces the thermal shock resistance of the mullite coatings and limits their usage at temperatures above 1000 °C at which the recrystallization takes place.

Some YSZ/mulite mixed solutions have been proposed to combine the advantage of both ceramic materials. In the YSZ/mullite coatings, the two elements can be dispersed in constant ratio along the entire top coat [22], or they can be layered, in which the composition varies along the coating, starting from totally YSZ in contact with the substrate up to totally mullite on the external surface [20].

2.1.4 SiRPA

Beyond the traditional ceramic TBCs, new research works are focused on innovative materials able to exploit the so-called wall "temperature swing" property. In more detail, the convective heat flux $\dot{Q}$ from the in-cylinder gas through the combustion chamber walls can be calculated by Eq. 1:

$$\dot{Q} = A \cdot h_g \cdot (T_{gas} - T_{wall}) \quad (1)$$

where A is the combustion chamber surface, h_g is the convective heat transfer coefficient, T_{gas} is the in-cylinder gas temperature and T_{wall} is the wall temperature. The "Temperature Swing" concept is a heat loss reduction technology that reduces the temperature difference between in-cylinder gas and surrounding walls, by quickly changing the wall temperature, following the transient gas temperature. A sketch of gas and surface temperatures during the entire engine cycle, for different combustion chamber wall materials is reported in Figure 2.3.

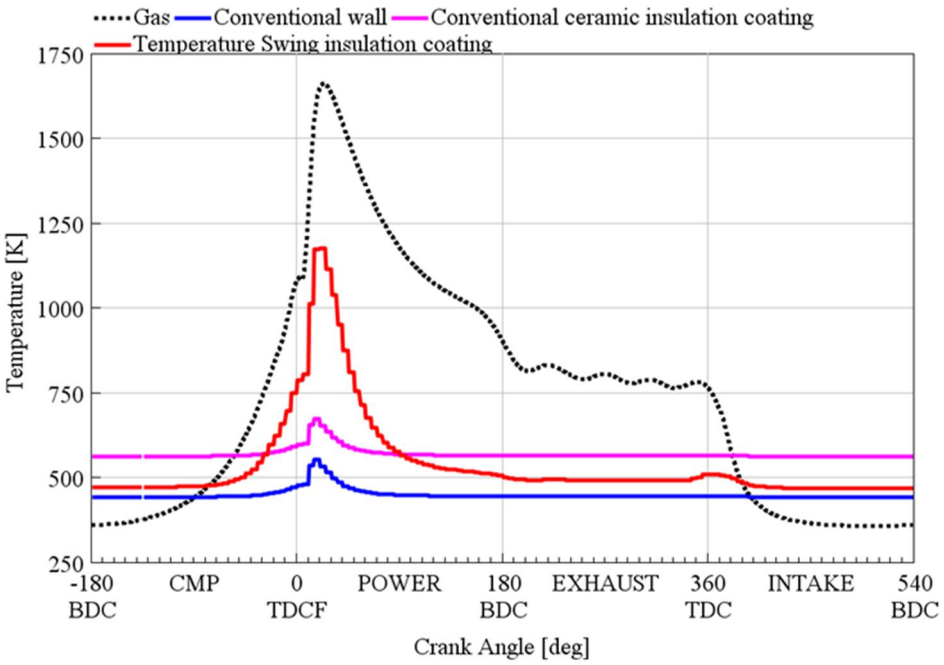

Figure 2.3 - Gas and wall temperature profiles during the engine cycle: conventional wall (blue line), conventional ceramic insulation coating (magenta line), temperature swing insulation coating (red line) and gas (black dotted line)

Three surface temperatures are plotted, corresponding to a conventional wall (metal), a conventional ceramic insulation wall (i.e., YSZ) and a "temperature swing" insulation wall.

The surface temperatures for the metals commonly used for combustion chamber (aluminum or iron alloy), which are characterized by high thermal conductivity, remain almost constant during the entire engine cycle. Conventional ceramic insulations present higher temperatures during the entire engine cycle, including the intake stroke. This fact results in reducing heat transfer during the combustion, but also in a decrease in the volumetric efficiency, deterioration in power, increase in the working gas temperature and exhaust emissions.

In the case of "temperature swing" insulation, the surface temperature of the coating, which is characterized not only by low thermal conductivity but also by low heat capacity, is able to fluctuate following the in-cylinder gas temperature.

With this technology, not just the heat losses during the combustion and expansion strokes can be reduced, thanks to the higher coating surface temperature, but also the intake air heating and the volumetric efficiency decreasing are avoided, due to the cooled coating temperature during the intake and compression phases.

Silica Reinforced Porous anodized Aluminium (SiRPA) is a particular coating developed by Toyota and obtained by anodization of an aluminium alloy (Al-12% silicon) [17,18,23]. The anodization is an electrolytic process that allows growth of a layer of aluminium oxide with a structure containing cylindrical channels with diameters of nanometer size (10-30 nm) oriented perpendicularly to the surface and constituting the structure nanometer porosity. In the structure, silicon crystals are also present, that disturb the nano-channel growth and form the micrometer porosity (1-10 μm). Moreover, through a post-treatment, a surface layer of perhydropolysilazane (PHPS) is applied as a sealant, to prevent the penetration of

the hot in-cylinder gasses inside the channels. Successively, the PHPS is converted to silica and forms a layer of few microns over the porous aluminium. Figure 2.4 shows the structure of SiRPA.

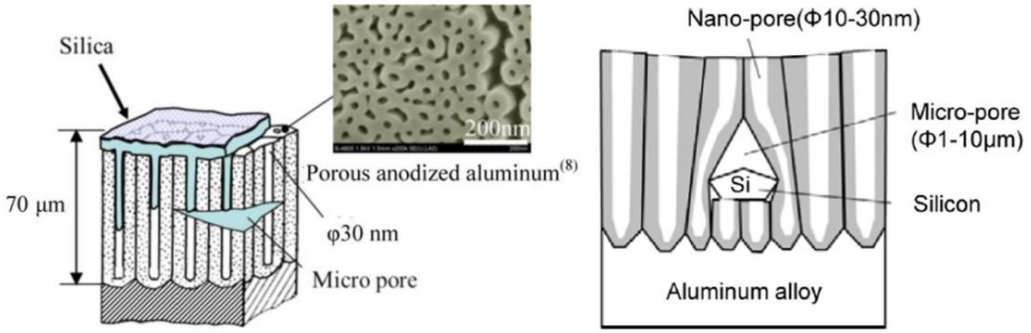

Figure 2.4 - Schemes of the general structure of SiRPA [17,18]

The silica sealant also has a strengthener effect: the PHPS infiltrates in the channels, reaches the micropores and, then, it transforms itself into silica, filling the infiltrated channels and coating the internal surfaces of the micropores; in this way, the hardness of the anodized layer results increased.

The high porous structure makes the coating density very low, which is a key factor for the "temperature swing" concept. As shown in Eq. 2 and 3, both the thermal conductivity (λ) and the volumetric specific heat capacity (c_v) directly depend on the material density (ρ). As above discussed, the conductivity and the specific heat capacity of the TBC must be as low as possible to obtain good thermal swing properties.

$$\lambda = \rho \cdot C \cdot \kappa \quad (2)$$

$$c_v = \rho \cdot C \quad (3)$$

In these equations, λ represents the thermal conductivity, ρ is the density, C is the mass-specific heat, κ the thermal diffusivity and c_v the volumetric specific heat capacity [24]. The declared thermo-physical properties of SiRPA at 500 K are reported in Table 2.2. In Figure 2.5 the SiRPA properties are compared with those of the other TBC materials.

Table 2.2 - Thermo-physical properties of SiRPA at 500 K [18]

Bulk density	1.4±0.15 [g·cm^{-3}]
Volumetric specific heat capacity	1300±140 [kJ·m^{-3}·K^{-1}]
Thermal diffusivity	0.52 [mm^2·s^{-1}]
Thermal conductivity	0.67±0.07 [W·m^{-1}·K^{-1}]

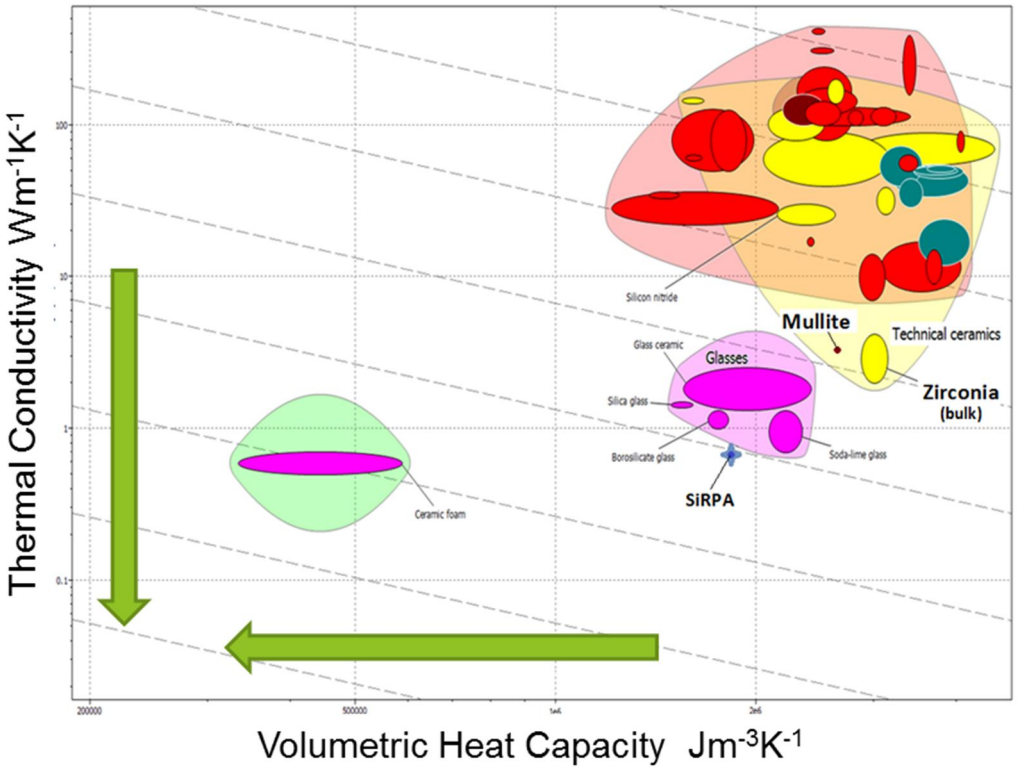

Figure 2.5 –Thermophysical properties of the most common TBC materials

2.2 Technological issues

In this *Section*, a brief overview of the technological processes, which are necessary for the application of the TBC on engine parts, is provided. In particular, two main techniques are described and analysed: thermal spraying and anodizing. In the last part of the section, costs and times of the process are also presented.

2.2.1 Thermal spray process

Thermal spray processes are coating techniques in which melted (or heated) materials are sprayed onto a surface. The feedstock of the process is heated by electrical (plasma or arc) or chemical systems (combustion flame). Thermal spraying techniques can provide coating thicknesses ranging from 20 µm to several mm, depending on process and feedstock – over a large area at high deposition rate (if compared with other coating techniques). The materials that can be used in the process are metals alloys, ceramics, plastics, and composites. They are fed in powder or wire form, heated to a molten or semi-molten state, and accelerated towards the substrate in the form of micrometer-size particles. The energy for the spraying is usually provided by combustion or electrical arc. The accumulation of numerous sprayed particles forms the final coatings.

Plasma spraying

Plasma spraying technique utilizes the heat derived from the ionization of plasma-gasses as argon, nitrogen, hydrogen, helium, or mixtures of these. The gun is made by an electrode (cathode) and a nozzle (anode) which generate a high-frequency electric arc. The arc ionizes the plasma-gasses coming from the nozzle in the form of a flame. The fill material is introduced (in powder form) into the flame flow, producing micro-particles that are, then, projected against the substrate at a speed of 200-400 m/s. The deposit rate of the process is generally in the range of 35-100 g/min. The Atmospheric Plasma Spray (APS) process is sketched in Figure 2.6.

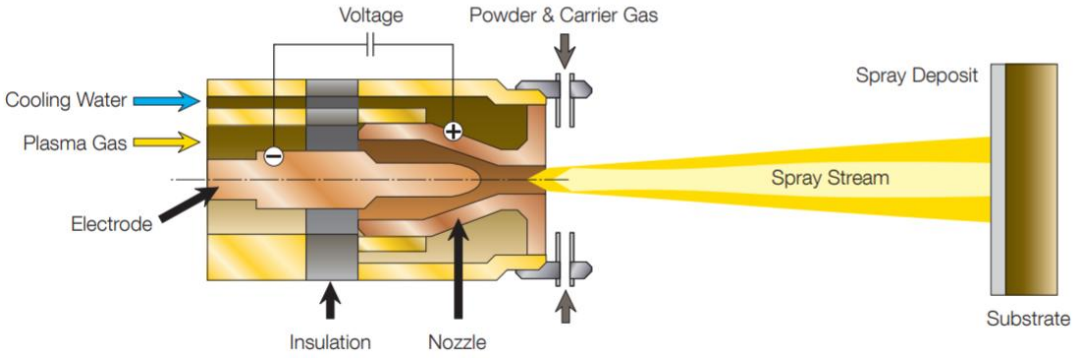

Figure 2.6 - Schematic diagram of Atmospheric Plasma Spray [25]

Various process parameters influence the characteristics of the coating:

- powders: size, shape and grain size distribution, feed flow rate;
- flame: type of gas, gas quantity, current, and voltage;
- the distance between the gun and the substrate.

The most frequently used powder materials are: (1) oxides (ceramics) of alumina, chromium, titanium, zirconium, etc.; (2) carbides of tungsten, chromium, etc.; (3) metals; (4) mixtures of oxides, carbides, metals with synthetic materials. The TBC thicknesses range between 200 to 1000 µm or more. The coating structure is generally high-porous with discreet anchoring to the substrate property.

Several variations of the plasma spray process can be found:

- Atmospheric Plasma Spray (APS): is the most used;
- Vacuum Plasma Spray (VPS);
- Inert Plasma Spray (IPS);
- Suspension Plasma Spraying (SPS);
- Solution Precursor Plasma Spraying (SPPS).

High-Velocity Oxygen Fuel

Another deposition technique used for TBCs is the High-Velocity Oxygen Fuel (HVOF). In this technique, the gas flow is generated by the mixture and successive ignition of oxygen (not necessarily pure) and fuel (gas or liquid) into a combustion

chamber. The high-pressure combustion gas is then accelerated through a nozzle and used for spraying the powder. The HVOF process is shown in Figure 2.7.

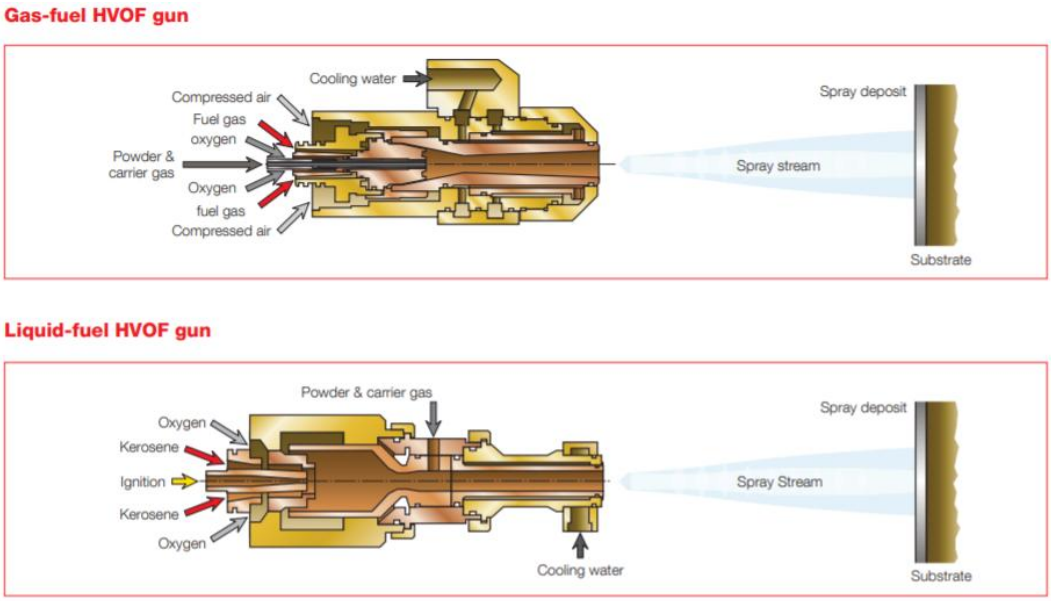

Figure 2.7 - Schematic diagram of High-Velocity Oxygen Fuel [26]

The process is characterized by high deposition rates (70-200 g/min with liquid fuels and 40-150 g/min with gas fuels) and usually does not interfere with the mechanical and structural characteristics of the substrate. Due to the high deposition rates, the TBCs are characterized by high density, high bond strength, high hardness, low porosity, low surface roughness (R_a less than 2 µm) and high resistance to wear. The thicknesses are between 20-200 µm.

HVOF technique can be used for deposing several materials:

- ceramics: alumina, chromium oxides, titanium oxides, and zirconia;
- cermets;
- MCrAlY coatings: used for bond coats.

2.2.2 Anodizing process

The anodizing process is already a well-established (for instance as anti-wear coating of piston ring grooves) and studied technology that allows the formation of a certain thickness of oxide on an aluminum surface [27–29]. Toyota has recently employed it for TBC application on diesel engine pistons [23]. Anodized aluminum for TBCs (called SiRPA by Toyota), differently from the anti-wear coating, presents a thicker and porous structure.

The technology is based on the principle of the electrolytic cell: the aluminum substrate represents the anode of the cell and is immersed in an electrolytic solution. When a specific potential is applied to the cell, the O^{2-} anions present in the solution migrate towards the anode and form an aluminum oxide (Al_2O_3) on its surface, sometimes doped with other anions present in the solution. At the industrial level, typical electrolytic solutions are made by: chromic acid, sulfuric acid, or oxalic.

Two parts make the anodic oxide layer: (1) an outer porous region and (2) a much thinner (maximum 2% of the thickness of the entire layer), dense and compact barrier layer. The latter is the first to be formed, and, although it is not conductive nor porous, it is helpful for the electrical current circulation.

The TBC characteristics depend on several process parameters such as voltage, type of electrolyte used, temperature, composition and pH of the solution, and eventual mechanical stirring. In particular, the pH of the solution is the most crucial factor for the coating structure: very thick and porous layers are obtained with acid pH (i.e., phosphoric acid solution), while compact and thin layers are obtained with phosphates. Then, the greatest pore diameters can be obtained with phosphoric acid, and smaller pores are obtained with oxalic and sulfuric acid; finally, the tiny and dispersed pore are obtained by the chromic acid due to the low solubility of the oxide formed [30].

Moreover, the applied voltage influences the TBC porosity: high voltage generates high pore size and low pore number [31,32].

Table 2.3 and Table 2.4 show the main parameters of the anodizing process.

Table 2.3 - Anodizing process parameters [33]

Electrolyte	**Chromic acid**	**Sulfuric acid**	**Oxalic acid**
Water solution	CrO_3, 2.5-3%	H_2SO_4, 20%	$(COOH)_2$, 5-10%
Current density [A/dm^2]	0.1-0.5 (cc)	14-22 (cc)	50-65 (cc)
Voltage [V]	0-40	14-22	50-65
Temperature [°C]	40	18-25	30
Treatment time [min]	20-50	10-60	10-30
Thickness [µm]	2-15	5-35	15

Table 2.4 - Pore density vs. voltage with four different electrolytes [33]

Electrolyte	Volt	Pore density (10^9 pore/cm^2)
Sulfuric acid, 15% 10 °C	15	76
	20	52
	30	18
Oxalic acid, 2% 25 °C	20	35
	40	11
	60	6
Chromic acid, 3% 50 °C	20	22
	40	8
	60	4
Phosphoric acid, 4% 25 °C	20	19
	40	8
	60	4

2.2.3 Time and cost of the processes

The technological processes previously presented can be classified into three groups (Figure 2.8). Traditional thermal spray processes are the most consolidated because the equipment and the process parameters were already robustly investigated. Recent thermal spray processes need a preliminary investigation for their development to have a successful impact on the coating realization. Critical problems with the material and the additional instrumentations can appear. For this reason, their cost could be higher in comparison with the old technologies.

Finally, the anodizing process is the most expensive technology for TBC. Problems with the treatment of the waste liquid electrolyte can arise. The time needed for the realization of the thicker coatings is much higher than that of other processes. The usage of the High-frequency Switching Anodizing (HSA) technology, instead of the traditional Direct Current Anodizing (DCA) could be a good compromise for reducing the process time [34].

The TBC prices for different engine components are shown in Table 2.5.

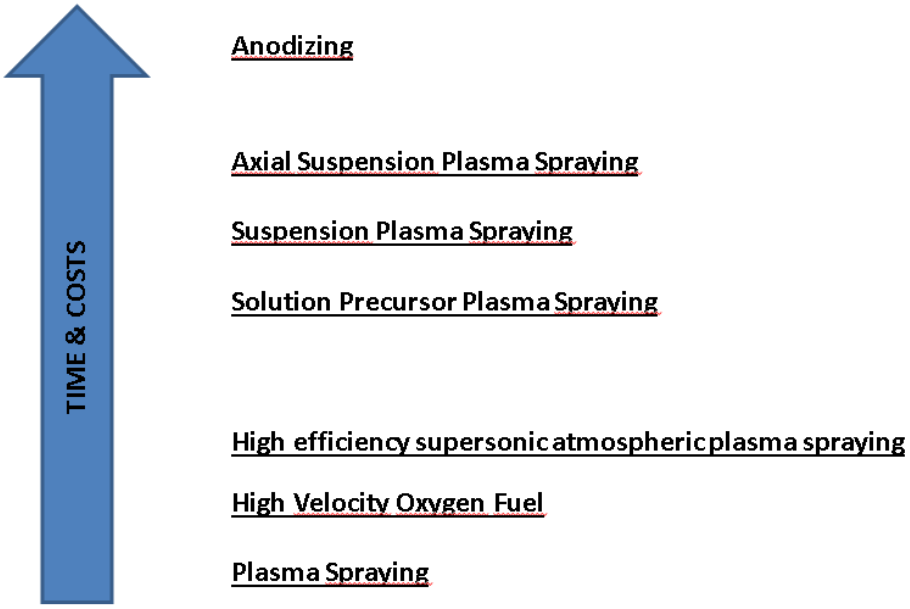

Figure 2.8 – Expected process time and costs

Table 2.5 - Automotive Coatings Price Sheet. SOURCE: Swain Tech Coatings [35]

Engine parts	Costs
Piston Top Only	$26.50 each
Cylinder Heads & Valve Faces (4 Cylinder Inline)	$200.00 each
Turbo Charger Housing	$90 – 125
Cast Iron Exhaust Manifold (4, 6 or 8 cyl.)	$150 – 275
Intake Manifold - Inside Runners	$200
Valve Face Only	$10.00 each
Single Exhaust Ports	$12.00 each

2.3 Low Heat Rejection Engines – Review

This *Section* of the Thesis presents the results, from the thermo-fluidodynamic point of view, of the previous research studies into LHRE concept, and illustrates the effects of insulation on engine performance, efficiency, and emissions.

The improvement of the engine thermal efficiency through the reduction of the in-cylinder heat losses has always been a controversial theme in the internal combustion engine Research and Development (R&D). In the past, a lot of researches were conducted on LHREs, especially using ceramic coatings, the so-called TBCs, on the combustion chamber walls, but the results have been often inconsistent and conflicting, not always leading to the expected advantages in terms of engine efficiency. Frequently, ceramic TBCs caused detrimental effects on the combustion (slowdown, combustion tail, etc.), producing efficiency losses and pollutant emissions increments. Other times, the issues were related to the durability, tribology, process time and costs, which did not allow the market penetration of this technology.

Nowadays, the idea of repurposing LHRE technology is based on two reasons:

- The new demanding CO_2 targets are requiring more expensive technologies and a high-priced solution, as thermal insulation, can become competitive.
- The more complex aftertreatment systems, used on the new generation of diesel engines, require higher exhaust gas temperatures, especially during their warm-up phase. Engine thermal insulation can be a good solution for increasing the engine-out gas enthalpy, thus reducing the fuel waste during the aftertreatment warm-up.

Early researches on LHREs started in the 1980s and were focused exclusively on ceramic materials, as zirconium oxide, chromium oxide, aluminum oxide, mullite, and coating thicknesses ranged from 0.05 to 2 mm.

T. Morel et al. [36–40] worked on a heavy-duty, turbocharged, diesel engine (Cummins NH) using different TBCs: 1.5 mm of Zirconia Plasma Spray (ZPS) coated all in-cylinder surfaces; ports were lined with 5.5 mm of alumina titanate; liner below the top ring reversal point was insulated by monolithic zirconia (5 mm thick). Authors also developed a numerical model to simulate the heat transfer process in the engine and the wall temperature swings along the combustion chamber surfaces. The results of T. Morel et al. indicate an improvement of about 5% in engine thermal efficiency in the case of ZPS coating on pistons and head with a cooled metal liner. The liner insulation created only a little increment in the thermal efficiency, with the disadvantages of lower volumetric efficiency, lower power and higher piston/ring/liner temperatures, causing durability and lubrication issues. In addition, numerical evaluations were performed on a passenger car Direct Injection (DI) engine with a swirl type combustion chamber. Higher BSFC benefits (10-12 %) were obtained compared to the heavy-duty because of the higher heat transfer caused by the swirl.

On the same engine, D. N. Assanis and J. B. Heywood [41] numerically studied the effects of 1.5 mm layer of plasma-sprayed zirconia on the engine head and pistons. They found out that the surface temperature swings within the engine cycle are more significant for coatings made by low-conductivity materials, like ceramics. The surface temperature swings of the TBC resulted in the order of 250 K, producing low degradation of volumetric efficiency and thermal efficiency increments up to 4%.

Y. Miyairi [42] developed a LHR diesel cycle simulation model for assessing the potentialities of different materials (such as Iron, PSZ, ZrO_2) used as TBCs. The results indicate improvement in thermal efficiency (from 2% to 2.7%), but also NO_x emissions increments. However, the materials with low thermal conductivity and low heat capacity showed advantages in the efficiency/NO_x trade-off.

D. D. Anderson [43] experimentally investigated the ceramic port insulation of a 10 liters diesel engine. In this analysis, the aluminum titanate was used to coat the grey iron substrate of the ports, producing a reduction of its temperature. Additionally, volumetric efficiency and exhaust gas temperature increments were also found.

More recently, P. Tamilporai et al. [44] used a cycle simulation code to study a 6 cylinders LHR diesel engine, characterized by 0.5 mm and 1 mm PSZ coatings on the cylinder head, piston top surface and water jacket side of the cylinder liner. Despite the smaller total heat transfer, the thermal efficiency of the LHRE was lower (6 to 8%) than the conventional engine. Moreover, the greater insulation of the thicker coating (1 mm) produces only increment in the exhaust temperature and not in the piston work.

In a recent article, H. Jaaskelainen and W. A. Majewski [45] described a Particulate Matter (PM) reduction system, developed by Engelhard, that uses zirconia TBCs on a 9 liters 2-stroke diesel engine. Metal alloy and YSZ were used respectively as Bond Coat and Top Coat on the piston crowns, head firedecks, and exhaust valves. The carbon fraction of the Total Particulate Matter (TPM) was decreased by 50%, but the Volatile Organic Fraction (VOF) resulted increased. However, the synergy between the zirconia coatings and Diesel Oxidation Catalyst (DOC) leads to a 59% reduction in TPM over the US Federal Test Procedure (FTP) driving cycle, without any impact on NO_x emissions and fuel penalty.

G. De Paola et al. [46] studied the effects of the combustion chamber insulation using a 3D Computational Fluid Dynamic (CFD) code, coupled with a 0D thermal model of the engine structure. They found out that the piston is the engine component with the greater potentialities in reducing the High Pressure Indicated Specific Fuel Consumption (HP ISFC), up to 3%, when it is insulated. The liner insulation seems to be inefficient because of the small area facing the combustion around the Top Dead Center Firing (TDCF), where the heat transfer mostly occurs. While the head insulation brings only about 1% in HP ISFC benefit for two reasons: the head surface is significantly smaller than the piston one, and the combustion is intentionally directed near the piston surface.

In their experimental activity on a turbocharged, heavy duty, diesel engine (Volvo/Mack MD-11), J. R. Serrano at al [47] discovered a 3% increment in BSFC

using 1 mm of agglomerated-sintered Y_3O_2-ZrO_2 as piston TBC. They have attributed this worsening to the increased duration of the combustion process. Furthermore, they found out that, combining the piston with the manifold insulation, the BSFC improves of about 1%. In Figure 2.9, the p-V diagram around TDCF and the heat release rate of both Standard and Insulated Piston configurations are reported. As one can observe, the presence of TBCs on the pistons slows down the early stage of the combustion process.

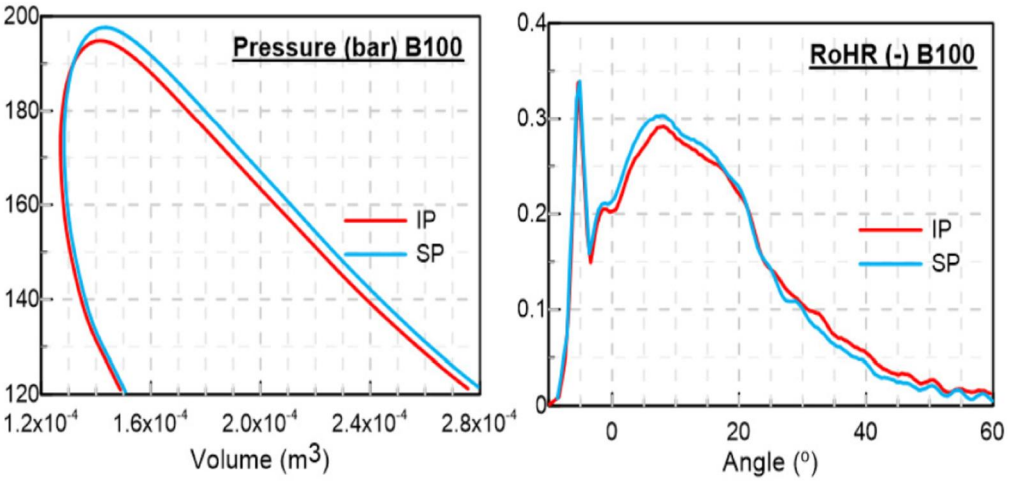

Figure 2.9 - p-V diagram around TDCF (left), Heat Release Rate (right). IP (Insulated Piston), SP (Standard Piston) [47]

Toyota Central R&D Labs and Toyota Corporation [17,18,23,24] recently developed and proposed a new material, called Silica Reinforced Porous anodized Aluminium (SiRPA), as piston TBC (see *Section 2.1.4*). Its main characteristics are the low thermal conductivity and heat capacity, which allow exploiting the thermo-swing property. Y. Wakisaka et al. [18] discovered, through an optically accessible engine, that the temperature swings of SiRPA result to be in the order of 140 K, under mid-load conditions at 1200 rpm. Furthermore, Toyota proposed to use a 100 µm layer of SiRPA on the pistons of the 2.8 liters ESTEC 1 GD-FTV diesel engine, reaching about 2 % in fuel savings [23]. However, the Indicated Specific Fuel Consumption (ISFC) deterioration caused by higher surface roughness of SiRPA (approximately Ra 3 – 5 µm) limited this application only on the piston crown, suggesting to avoid its use on the piston bowl.

C. Binder et al. [48] used the phosphor thermometry on a heavy duty, single-cylinder, optically accessed diesel engine to investigate the effects of 850-µm-thick YSZ coating (with 8 mol% of Y_2O_3). An additional 150-µm-thick of NiCrAlY as the bond coat was used. The TBC was applied on the entire surface of the steel-made piston. The main conclusion of this research are:

- the TBC slows down the combustion process (see Figure 2.10);
- the volumetric efficiency decreases in the coated configuration, due to the higher averaged surface temperature of the piston (see Figure 2.11);
- the surface temperature oscillations of both configurations are comparable (see Figure 2.11);

- the local instantaneous heat flux is much higher in the steel piston configuration with respect to the coated one, and this difference is partially due to the bigger thermal effusivity of the steel ($e = \sqrt{\lambda \rho c_p}$).

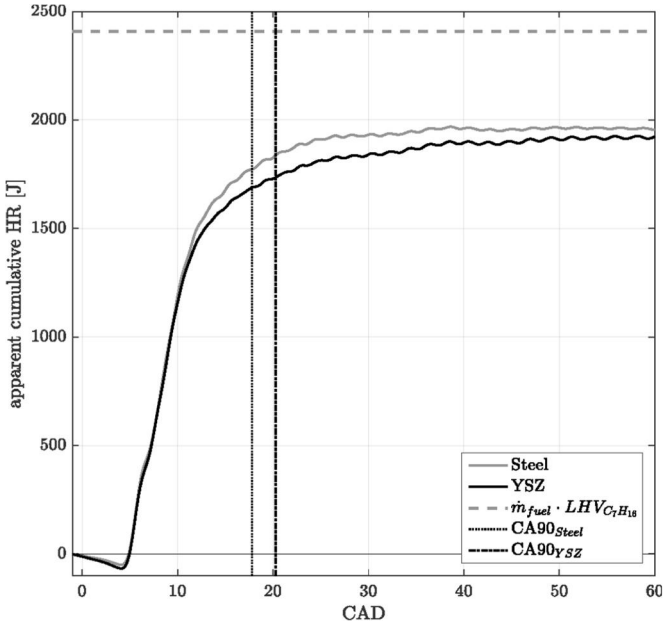

Figure 2.10 - Apparent cumulative heat release of the steel piston and the YSZ piston at $\dot{m}_{fuel}$ = 54.1 mg/inj and λ = 3.2 [48]

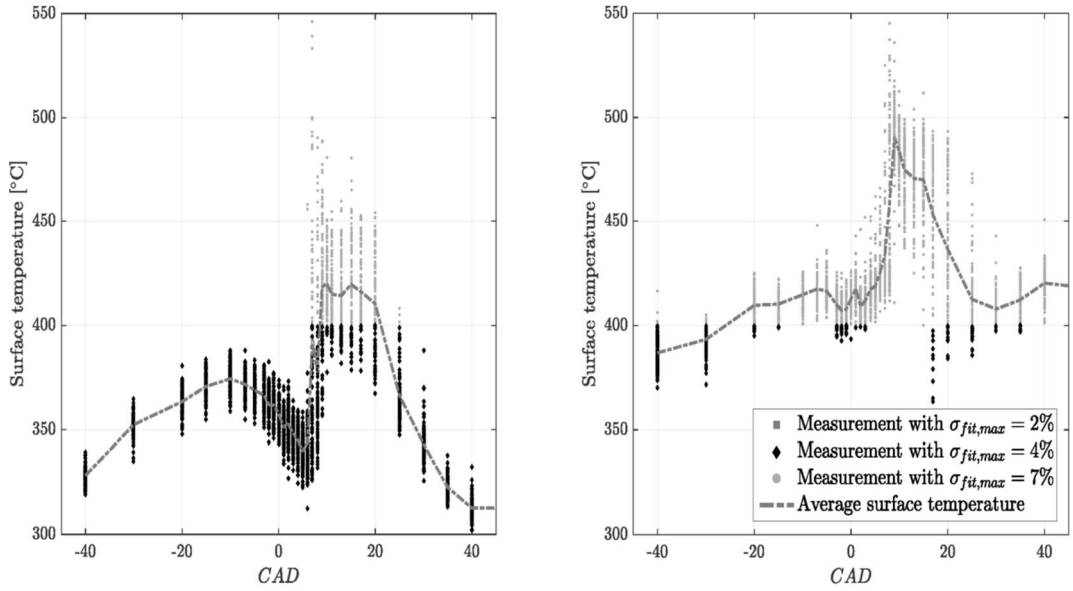

Figure 2.11 - Temperature measurements around TDC at the bowl measurement location of the steel piston (left) and YSZ piston (right) for $\dot{m}_{fuel}$ = 54.1 mg/inj and λ = 3.2 [48]

Additional analysis of zirconia TBC applied on a steel piston was performed by N. Uchida and H. Osada [49]. They found out that the high porosity and roughness of the zirconia cause a reduction of the thermal boundary layer and a consequent increase in the heat transfer coefficient. To avoid this problem, they designed a multi-layer zirconia TBC (thickness of 300 µm), composed by: (1) 50 to 80 µm of bonding layer, (2) 200 µm of high porosity layer, used to reduce the delay time for surface temperature swing and (3) 50 to 80 µm of dense layer at the

top to reduce the superficial roughness and porosity of the coat. They compared the multi-layers configuration with the baseline steel piston and with a back-side zirconia coating piston, where zirconia was used to masking the oil cooling gallery of the piston (at the back side cavity). The findings of this research were:

- The averaged piston surface temperatures resulted increased in both configurations, demonstrating potentialities in reducing the heat losses.
- Back-side coating showed potentiality by increase in the engine indicated work while multi-layers coating exhibited a deterioration in the in-cylinder pressure and combustion efficiency. $\Delta P=P_{expansion} - P_{compression}$ relative to the baseline steel piston is reported in Figure 2.12. The multi-layers piston showed a particularly deep pressure loss near the TDCF, partially recovered in the middle of the expansion. On the other hand, the back-side coating exhibited lower pressure loss, which helped in the indicated work increase.
- Material with much lower thermal conductivity and heat capacity than zirconia is necessary to obtain an effective temperature swing insulation.

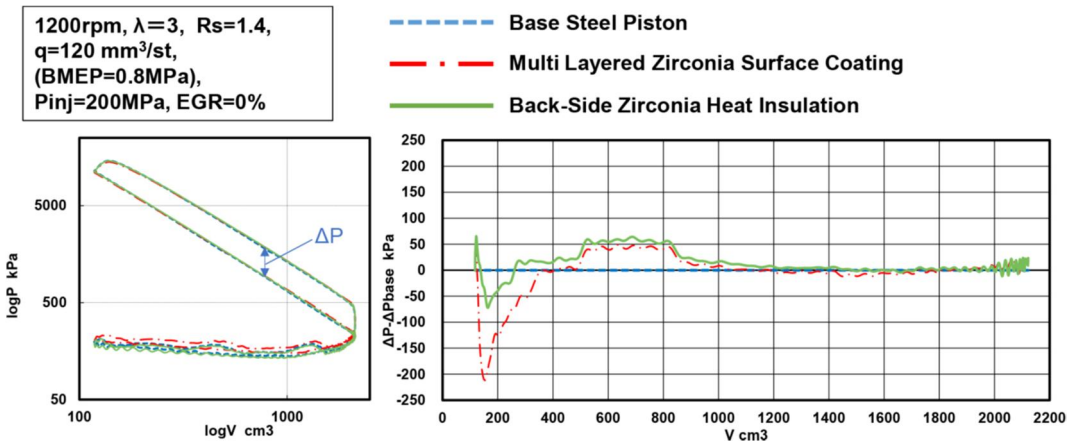

Figure 2.12 – logP/logV diagram (left) and ($\Delta P-\Delta P_{base}$)/V diagram (right) ($\Delta P=P_{expansion}-P_{compression}$) [49].

D. Gatti and M. Jansons [50] used a 1D numerical conjugate heat transfer model to analyze the performance of a military LHRE. Through a parametric study, they demonstrated that coatings with low conductivities and heat capacities have higher potentials in heat transfer reduction and efficiency improvement. Moreover, the thick coatings provide additional heat loss reductions, while the optimal thickness for improving the engine efficiency is in the 50 – 100 µm range (using a zirconia coating). Finally, it is also suggested that the Heat Transfer Coefficient (HTC) reduction has a more visible effect on heat transfer than any change in cylinder wall properties, so future research efforts should be directed towards the HTC reduction techniques as piston geometry design.

K. Uchihara et al. [51] assessed the thermal insulation effects of the different piston areas: center cone, side wall, lip, and crown, using both 3D CFD simulations and tests (see Figure 2.13). The adopted coating layers were 440 µm of zirconia and

60 µm of CoNiCrAlY, as Bond Coat. It was found that the piston crown insulation causes: intake air heating, decrease in volumetric efficiency and increase in smoke emissions, while the lip and side wall insulations are the most advantageous for reducing cooling losses and smoke emissions.

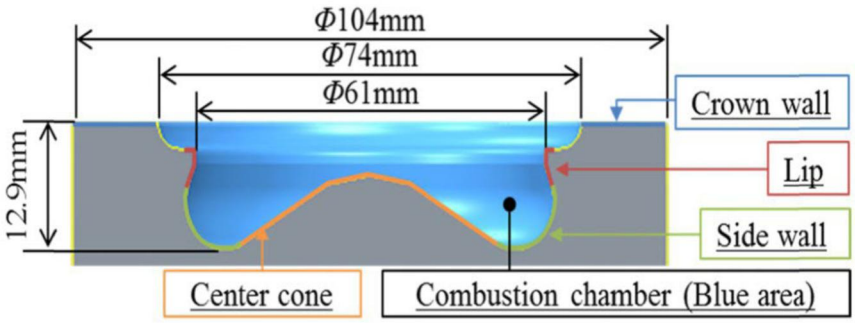

Figure 2.13 - Shape of piston cavity [51]

Besides, A. Poubeau et al. [52] investigated the thermal insulation potentialities using 3D CFD techniques with Conjugate Heat Transfer (CHT) model. CHT is used for coupling the fluid-dynamics and combustion with the conduction in the solid structure of the engine. They proved that the piston cavity is the surface with the highest normalized heat losses, followed by the piston top and dome because the flame impingement directly involves the cavity and the top areas. Successively, using CHT model and considering the coating thermal inertia, they assessed the performance of a 100 µm TBC on the entire piston surface, obtaining:

- 1.6 % in gross Indicated Mean Effective Pressure (IMEP) improvement (at 2500 rpm and 12 bar of IMEP);
- 17.2 % increment in the wall to gas heat transfer during the intake phase, with a consequent reduction (0.6 %) of the intake mass, in the above mentioned operating point.

3D CFD simulations were also used by A. Broatch et al. [53] for evaluating the impact of the coating surface roughness on the combustion process in a turbocharged spark-ignited engine. In general, the effect of the surface roughness is more evident with higher values of roughness (greater than 14 µm) and at higher speed and load (3000 rpm and 13 bar of IMEP). In particular, the maximum Rate of Heat Release (RoHR), the Heat Transfer (HT) and the indicated efficiency resulted reduced. Moreover, a comparison between uncoated and coated configurations was performed. The TBC thickness was 100 µm, its thermal conductivity was 1.5 W $m^{-1}K^{-1}$, its thermal capacity was 3500 kJ $m^{-3}K^{-1}$, and its surface roughness was 14 µm. HT reductions of about 3.5 – 4.5% can be achieved with TBCs on the piston and head surfaces, getting an indicating efficiency improvement of 0.1 - 0.3%.

Chapter 3

Numerical analysis on the Low Heat Rejection Engine technology

Part of the work described in this Chapter has been previously published in:

- S. Caputo, F. Millo, G. Cifali, F.C. Pesce, Numerical Investigation on the Effects of Different Thermal Insulation Strategies for a Passenger Car diesel Engine, SAE Int. J. Engines. 10 (2017). doi:10.4271/2017-24-0021.

This *Chapter* presents a preliminary analysis, through the one-dimensional CFD engine simulations, on the effects of the combustion chamber insulation in a passenger car, diesel engine application. Firstly, the complete and ideal insulation of the different engine components (i.e., pistons, liner, firedeck and valves) has been studied and discussed. Afterward, the analysis has been focused on the impact of different piston TBCs on engine performance and efficiency, using a 0D thermal model representative of the engine structure. In particular, the effect of different coating materials and thicknesses has been assessed.

Finally, the most promising TBC for piston application was selected using the simulation outputs, and then, successively tested in a real application.

3.1 Engine model description

A one-dimensional (1D) commercially available numerical code, developed by Gamma Technologies, GT-SUITE, was employed for the simulations. The numerical code can solve the Navier-Stokes equations (the conservation of continuity, momentum, and energy) in the one-dimensional formulation [54]. A predictive multi-zone combustion model, DIPulse [55], developed by Gamma Technology, was used for the burn rate calculation (more-in-depth combustion model description is reported in Appendix A). A flow-based heat transfer model, developed by T. Morel and R. Keribar [36] was implemented for the calculation of the Heat Transfer Coefficient (HTC). In particular, this model provides for a better estimation of the heat fluxes through the different engine components respect to the traditional heat transfer models (i.e., Woschni, Annand), because it is based on the in-cylinder flow field, including swirl motion and turbulence. This characteristic makes the model suitable to address the LHRE issues [36]. A comparison between the Flow and Woschni heat transfer models was performed and described in Appendix B.

Furthermore, the engine wall temperatures (including pipe temperatures) were calculated through thermal models, which solve the one-dimensional, steady-state equation of conduction heat transfer in the solid layers adjacent to the gasses.

As far as the fuel injection is concerned, a previously developed Common Rail Injector model [56] was employed for the calculation of the injection rate profiles, starting from the Energizing Times (ETs), Dwell Times (DTs) and injection pressures.

Moreover, the injected fuel quantity, the turbine rack position (Variable Geometry Turbine), and the EGR valve respectively control the engine load, the boost pressure and the EGR ratio through three different model-based controllers. Finally, the input variables of the engine model are the engine operating conditions (speed and load), the injection timing (SOI, ETs, DTs, injection pressure), the boost pressure, the EGR rate, and the boundary conditions (as ambient conditions, coolant and oil temperatures).

3.1.1 Case study

The engine under investigation was a turbocharged, direct injection, four-cylinder automotive diesel engine with high/low pressures cooled EGR system. The engine specifications are reported in Table 3.1.

Table 3.1 – Engine specifications

Engine Type	Direct-Injection diesel
Configuration	In-Line 4 Cylinder
Maximum Torque	320 Nm (at 2000 rpm)
Maximum Power	100 kW (at 4000 rpm)
Displacement	1598 cm^3
Compression Ratio	16:1
Bore x Stroke	79.7 mm x 80.1 mm
Injection system	Common Rail
Turbocharger	Single-stage (intercooled) with VGT
EGR system	High-Pressure & Low-Pressure (cooled)

3.1.2 Simulation Matrix

Five different engine operating points have been chosen for the simulations (engine speed [rpm] x BMEP [bar]): 2000x2, 1500x8, 2000x8, 2500x8, 2000x16 (see Figure 3.1). This matrix, characterised by load and speed sweeps, was designed for assessing the influence of the engine speed and load on the thermal insulation performance, in the most interesting operating conditions for an automotive application.

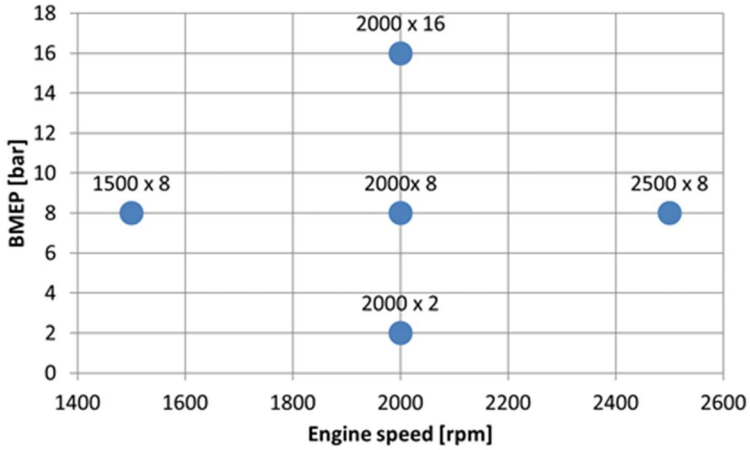

Figure 3.1 – Matrix of the simulated engine operating points

3.1.3 Model validation

Comparisons between the numerical and the experimental results are shown in Figure 3.2. The simulation results reached a satisfactory accuracy in BSFC prediction, with an averaged error of about 2.5%.

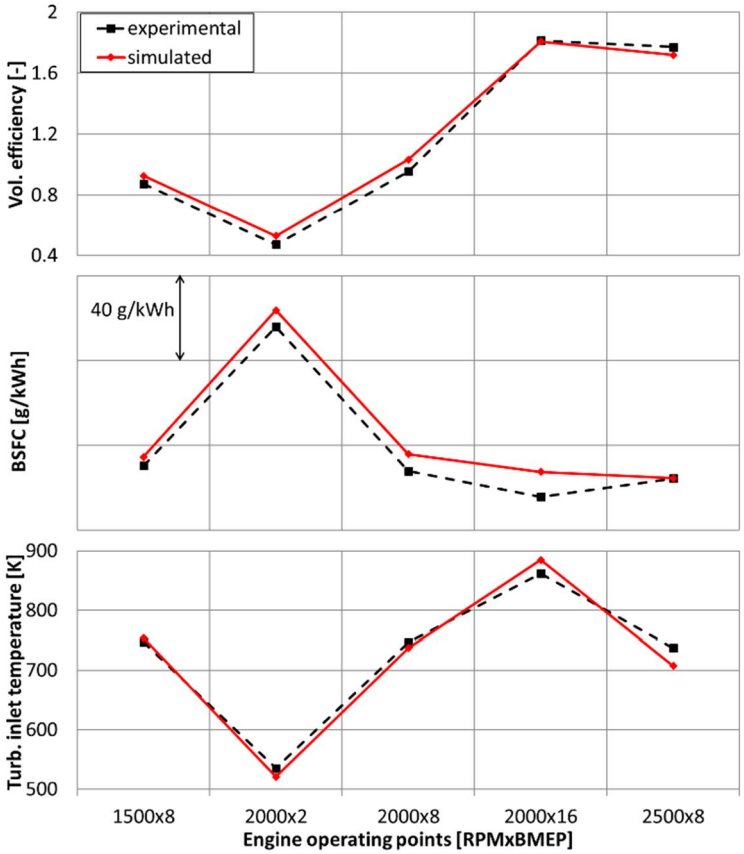

Figure 3.2 - Comparison of predictions and experimental data

3.2 Ideal insulation of the engine components

The objective of this *Section* is to assess, through the 1D CFD engine model, the maximum theoretical potential in heat transfer and BSFC reductions derived from the complete thermal insulation of the different engine components (pistons, firedeck, valves, and liner) in order to fix a sort of thermo-dynamic limit that cannot be overcame. The ideal and complete insulation of the component from the in-cylinder gas has been realized through the zeroing of the respective heat transfer coefficient. The in-cylinder heat transfer and BSFC reductions derived from the complete insulation of the engine components are shown Figure 3.3. The results show that the higher amount of the in-cylinder heat transfer is lost through the piston, followed by firedeck, liner, and valves. Consequently, more than 45% of the total heat transfer can be theoretically reduced with the piston insulation only, and more than 20% can be reduced with the firedeck insulation. Moreover, the piston insulation can ideally lead to 10% in BSFC reduction (5% in the case of firedeck insulation). These results are ascribable to the fact that firedeck and piston surfaces are more exposed to the in-cylinder gas during the combustion, which is the phase of the cycle with the highest heat loss. Furthermore, the combustion is intentionally directed towards the piston, causing high turbulence and high temperature near the walls and, consequently, great HTC and heat flux through the component [46]. Differently, the liner insulation is not so efficient in heat transfer and BSFC reductions, because of the limited liner area facing the combustion chamber at

TDCF, as affirmed in [37]. Most of the research works confirm that the piston is the component with the most significant potential in heat transfer and BSFC reductions when it is thermally insulated [37,41,46,57].

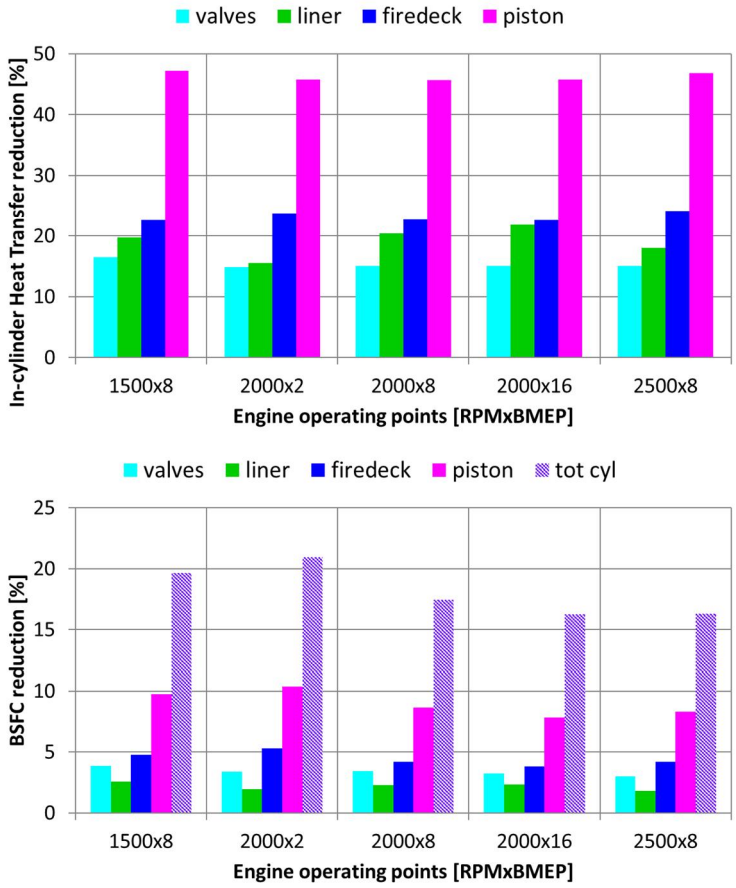

Figure 3.3 – Maximum in-cylinder Heat Transfer reduction (top) and BSFC reduction (bottom) due to the component insulations

The effects of thermal insulation on the volumetric efficiency and the turbine inlet temperature are shown in Figure 3.4. All the component insulations are useful for the volumetric efficiency increase since the zeroing of the heat transfer from the component to the inducted air during the intake results in a reduction of the in-cylinder gas temperature in this phase. In particular, the valve insulation resulted to have more potential in the volumetric efficiency increase due to the higher amount of heat transferred from the intake valves toward the intake air.

As far as the exhaust temperature is concerned, all the component insulations, except for the valves insulation, provide an increment in the turbine inlet temperature, because of the reduced heat losses. In the case of the valves insulation, the effect of lower intake air temperature (about 20 K lower at 2000x16) prevails, causing lower in-cylinder temperature during the entire engine cycle, including the exhaust phase. For better clarification of these phenomena, the trends of the heat transfer and the gas temperature within the engine cycle are shown in Figure 3.5.

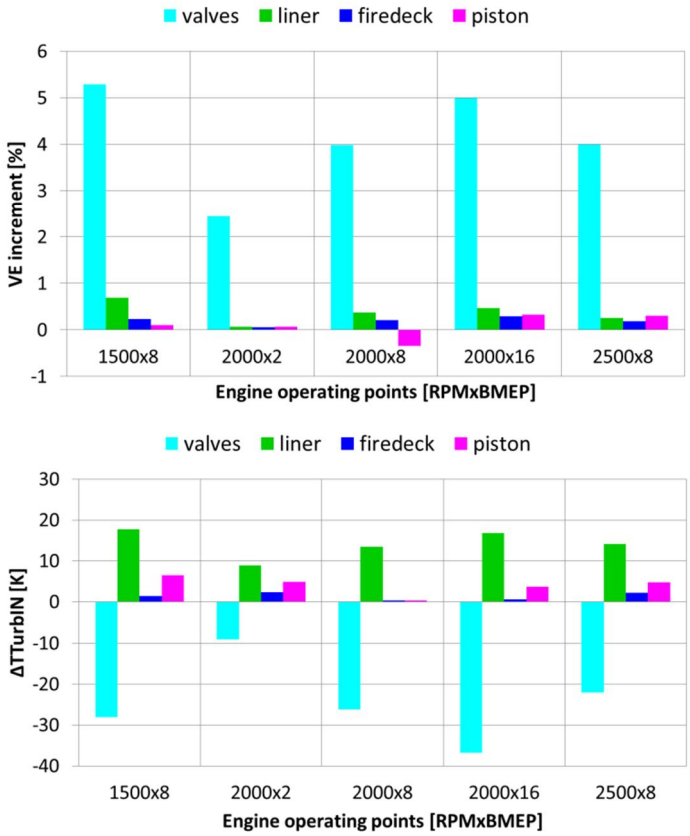

Figure 3.4 – Volumetric efficiency increment (top) and turbine inlet temperature variation (bottom) due to the component insulations

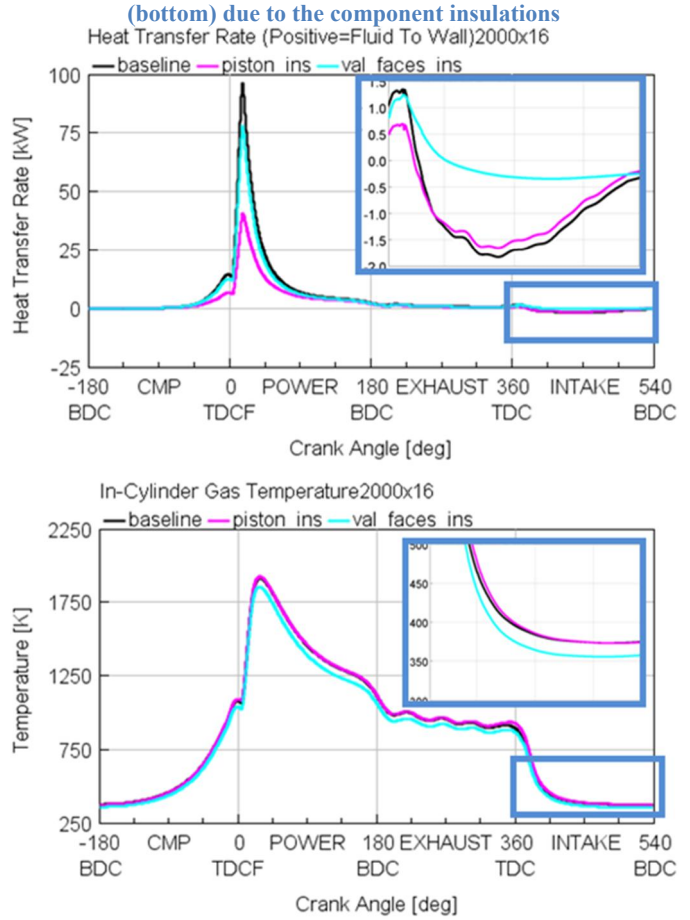

Figure 3.5 - In-cylinder heat transfer rate (top) and gas temperature (bottom) for baseline, piston insulation and valve insulation

3.2.1 Effects of Partial Insulation

The engine model was also used for assessing the effects of different levels of insulation of the engine components. For this scope, the heat transfer coefficients between in-cylinder gas and each engine component have been reduced by 25%, 50%, 75%, and 100%. The simulations have been repeated for all the operating points of the matrix. Figure 3.6 illustrates that the relation between the heat transfer reduction and the insulation level of each component is linear. The slopes of the curves are proportional to the effectiveness of the component insulation in reducing the heat transfer.

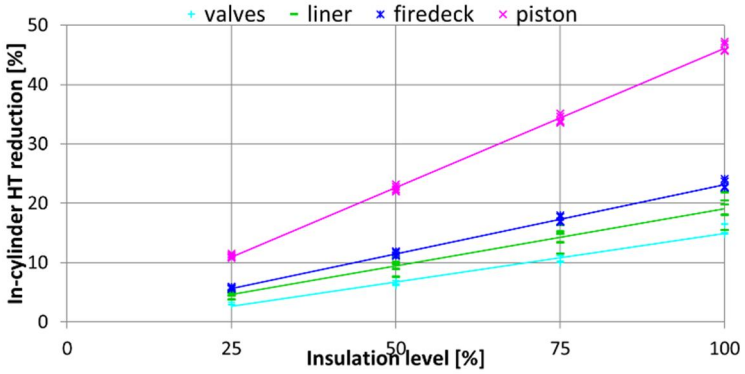

Figure 3.6 - Effects of insulation levels on the in-cylinder heat transfer

Moreover, as shown in Figure 3.7, the correlation between the BSFC reduction and the heat transfer reduction is also linear and, in this case, the slopes of the curves are proportional to the conversion efficiency of the in-cylinder retained energy, due to the insulation, into useful work, namely the Retained Heat Conversion Efficiency (RHCE) as defined in [40]. RHCE depends on the improvements in the engine indicated efficiency due to both the heat loss reduction and the volumetric efficiency increment.

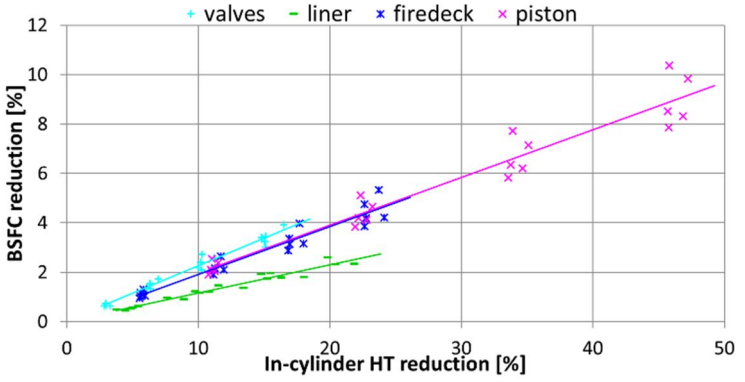

Figure 3.7 - Correlations between in-cylinder heat transfer and BSFC for the different insulation strategies

Valve insulation results to be the technology with the highest RHCE because it produces not only a reduction of heat losses during the combustion and expansion strokes, but it is also capable of increasing the volumetric efficiency of the engine and consequently reducing its pumping losses. Piston and firedeck insulations exhibit lower RHCE because these technologies have a limited impact on the intake

air temperature and volumetric efficiency, while the liner insulation turns out to be the worst strategy for RHCE, due to the restricted area exposed to the combustion gasses near the TDCF. Indeed, the liner insulation starts having positive effects only in the late phase of expansion, when the combustion is almost finished, bringing an increase only in the exhaust gas temperature (see Figure 3.4).

The obtained results are in agreement with the outcomes of past research works reported in literature. For example, De Paola et al. [46] found out that using a 0.5 mm TBC applied on piston, head, and liner, it is possible to obtain heat transfer reductions of 18%, 6%, 3% respectively, and BSFC reduction respectively of 3%, 1.4%, and 0.3% respectively.

3.3 Piston thermal barrier coatings

The first stage of the numerical analysis, regarding the ideal insulation of the engine components, has shown that piston insulation is the most promising technology for reducing heat transfer and enhancing the engine efficiency. Consequently, the second stage of the analysis was addressed to the evaluation of the real performance of the piston insulation technology, in particular when it is exploited using TBCs. In this *Section*, the effects of the thermo-physical properties of the coatings (thermal conductivity, heat capacity, and thickness) are analyzed and discussed.

For this purpose, a thermal model, representing the engine structure, was created and coupled with the engine model. The thermal model is zero-dimensional: the engine components (i.e., pistons, liners, head, valves) are discretized in nodal thermal masses, each characterized by its thermo-physical properties (heat exchange area, density, mass, thermal conductivity, specific heat, and temperature). The thermal masses are then connected through thermal resistances, representing the contact resistances; moreover, the masses are connected to the fluids (in-cylinder gas, coolant, and oil) through convection heat transfer coefficients (Figure 3.8). The 0D thermal model is directly coupled with the 1D engine model inside the GT-SUITE simulation platform. In this way, the wall temperatures, which are calculated through the thermal model, are imposed to the engine model as boundaries, and vice versa, the in-cylinder gas temperature and the gas-wall HTCs, which are calculated using the engine model, are used as boundaries in the thermal model. This procedure runs iteratively until the two models reach the numerical convergence.

The developed thermal model is also capable of calculating the temperature swings of the engine surfaces, through the solution of the non-steady-state conduction equations. This feature is fundamental for the TBC assessment because for low-thermal-conductivity and low-thermal-inertia materials, the wall temperature swings are much higher than those generated by the traditional metal materials [41,52,58].

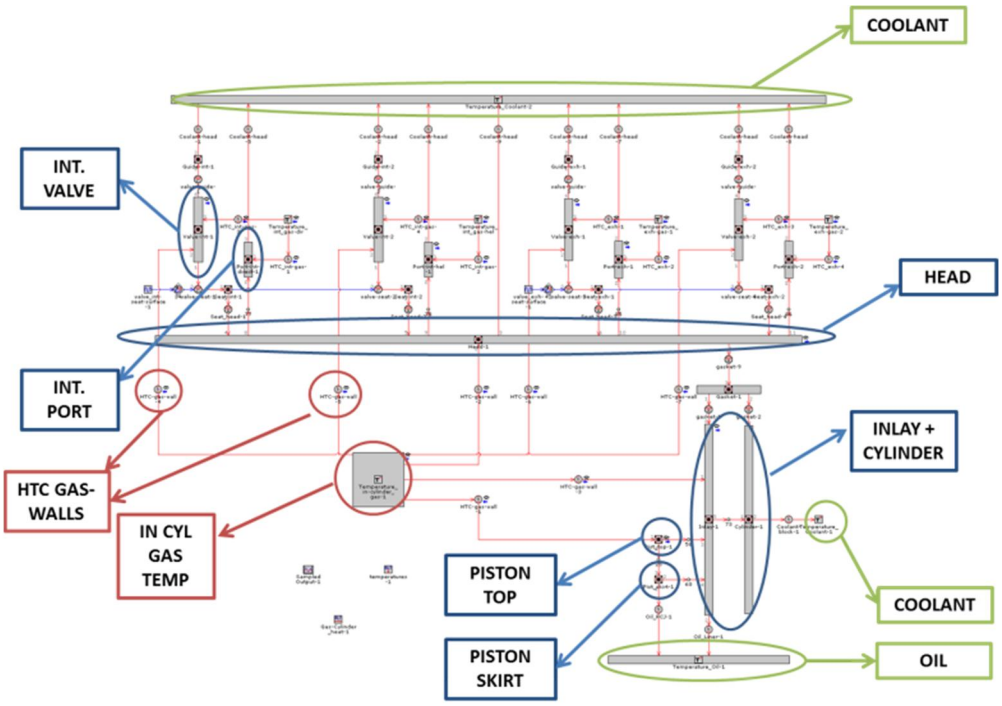

Figure 3.8 - Engine thermal model layout in GT-SUITE

3.3.1 Anodized aluminum TBC

As described in *Section 2.1.4*, the anodized aluminum is characterized by a very porous structure, due to the presence of cylindrical nano-channels and micro-pores. Due to its porosity, the material is characterized by very low density, thermal conductivity, and heat capacity, which ensure higher surface temperature swings respect to the traditional coatings (i.e., ceramics).

The simulation model was used for assessing the potential of the anodized aluminum as piston TBC. The model input data (i.e., the thermo-physical properties of the coating) were taken from literature, and they are reported in Table 2.2. As far as the coating geometry is concerned, an optimal thickness of 100 µm was chosen [50,52,59] and the complete piston area, including bowl and crown, was selected for the insulation.

Figure 3.9 illustrates the model predictions of the piston wall temperature swings at 2000 rpm and 8 bar of BMEP. The coated piston configuration has higher wall temperature oscillations within the engine cycle then the baseline configuration. Consequently, due to the higher peak of wall temperature near the TDCF, the heat losses during combustion can be reduced, while, due to the sufficiently lower wall temperatures during the intake and compression strokes, the intake air mass and volumetric efficiency are maintained constant. Moreover, Figure 3.9 shows in red, dotted line, the temperature of the surface immediately under the coating. It results lower than the temperature of the baseline piston due to the thermal barrier effect of the coating on the aluminum substrate.

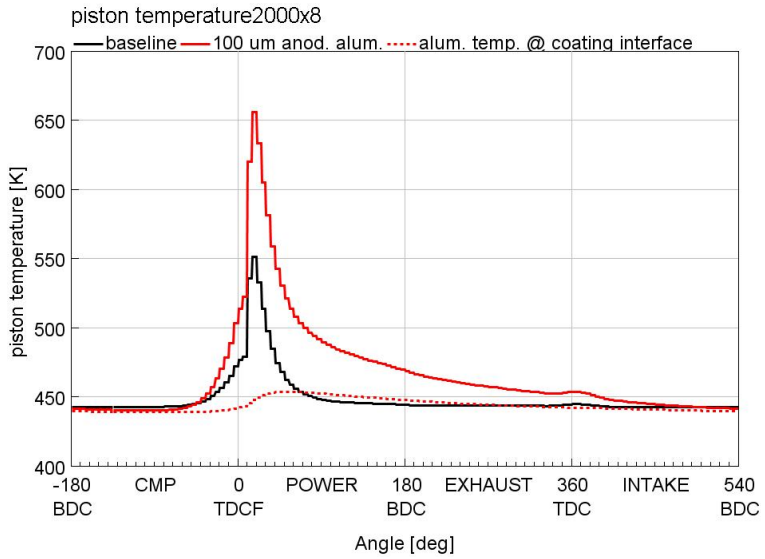

Figure 3.9 - Piston wall temperature swings (baseline and anodized aluminum)

The cycle-averaged piston temperatures are displayed in Figure 3.10: the piston wall temperature is increased of about 20 K using the TBC. Furthermore, the aluminum substrate temperature is decreased of 10 K at higher loads and speeds, reducing the thermal stress and fatigue of the metal.

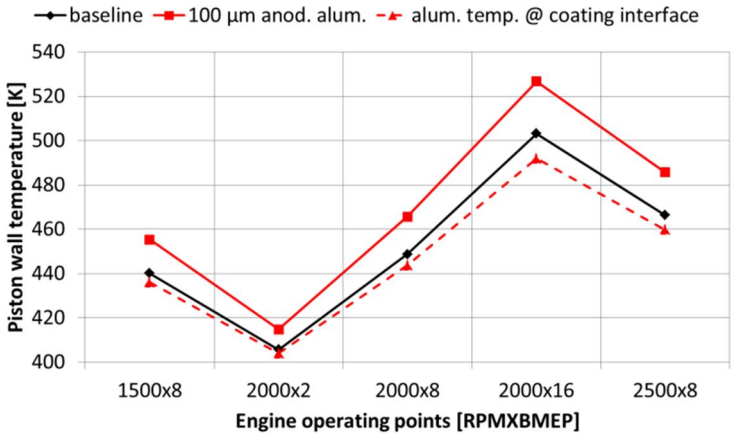

Figure 3.10 - Cycle-averaged piston wall temperature of baseline and anodized aluminum

The coating potentialities in heat transfer and BSFC reductions are shown in Figure 3.11. Thanks to the higher wall temperature, and the greater wall temperature swing, the coated piston technology is able to reduce total in-cylinder heat transfer, enhancing the engine efficiency. Although this trend is confirmed in all the operating points of the matrix, the thermal insulation is more effective at the higher loads and speeds (5.6% in heat loss reduction and 0.9% in BSFC improvement at 2000x16), due to the elevated gas temperature reached in these points. Therefore, the thermal insulating effect of the coating is more effective when the temperature difference between the in-cylinder gas and the coolant/oil is higher.

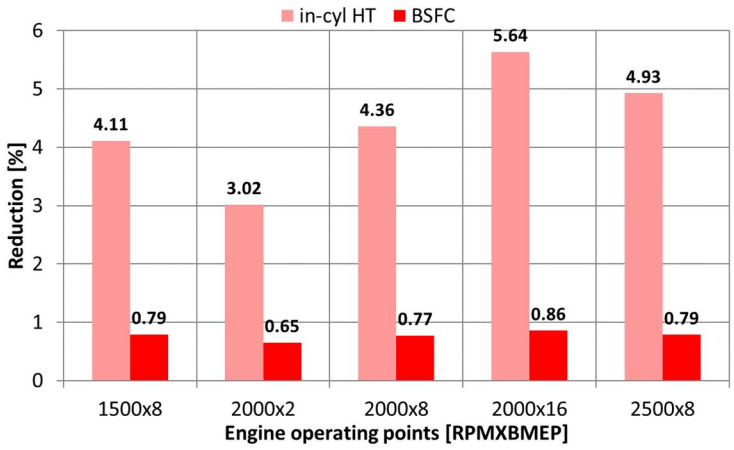

Figure 3.11 - Effects of piston coating (100 µm - anodized aluminum) on in-cylinder heat transfer and BSFC

Effects of coating thickness

The influence of the TBC thickness on the engine efficiency has been evaluated through the numerical model. For this scope, different thicknesses (ranging from 60 µm to 2000 µm) of anodized aluminum were simulated. Figure 3.12 shows that the relationship between the coating thickness and the reduction in heat transfer is asymptotic, tending towards the ideal case (reported in grey). Moreover, the higher loads and speeds exhibit greater potential in heat loss reductions because of their elevated differences between the in-cylinder gas and the coolant/oil temperatures.

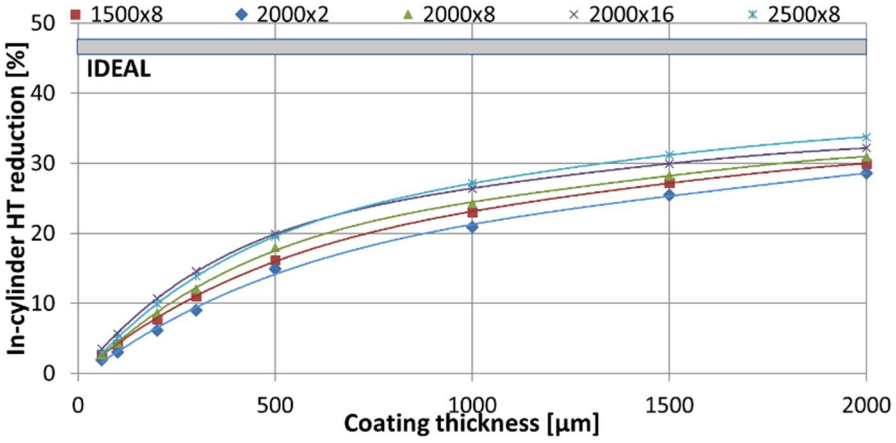

Figure 3.12 - Effects of piston coating thickness (anodized aluminum) on the in-cylinder heat transfer

As illustrated in Figure 3.13, the relation between heat transfer and BSFC reductions is linear for all the engine operating points. In particular, the curve slopes, which are proportional to the conversion efficiency of the in-cylinder retained energy into useful work (namely, RHCE), result greater for the lower loads and speeds. This trend can be explained by the greater share of heat loss over the total fuel energy at low-speed and low-load operating points. Accordingly, the same percentage of heat loss reduction can lead to higher BSFC benefit at low loads and speeds.

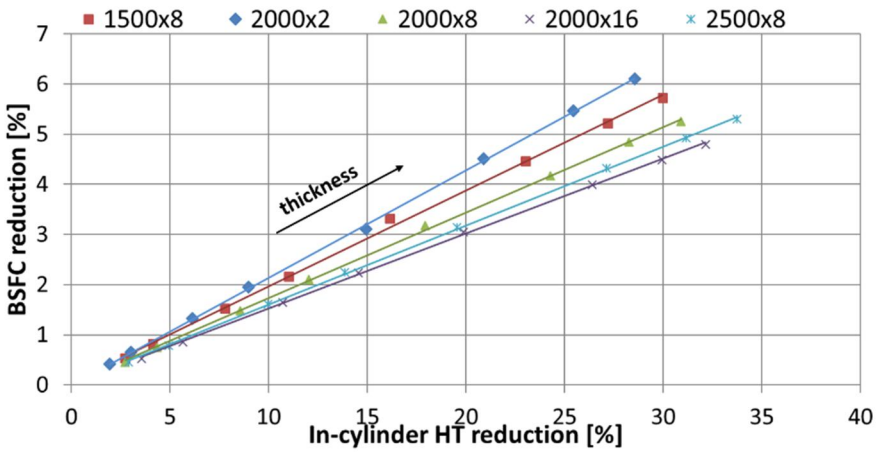

Figure 3.13 - Correlation between in-cylinder HT and BSFC reduction for anodized aluminum TBC

In Figure 3.14 the piston wall temperature swings, obtained with different thicknesses, are shown.

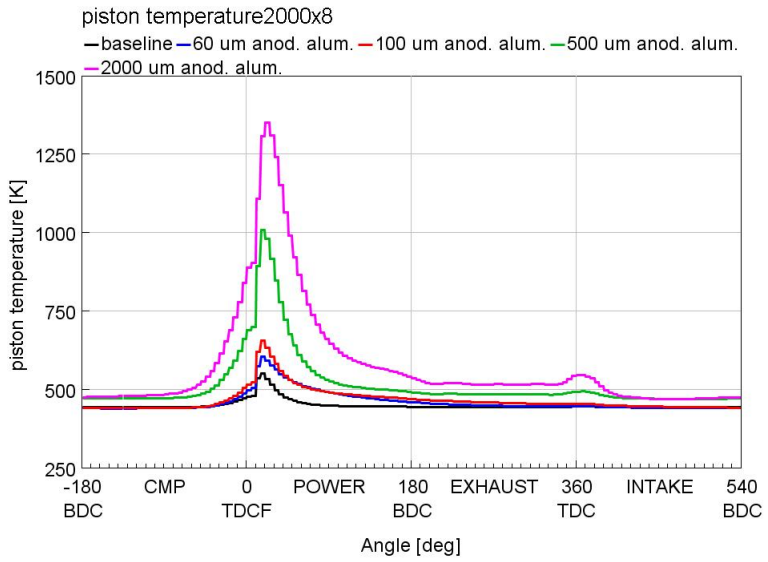

Figure 3.14 - Piston wall temperature swings for different coating thicknesses

Greater peak wall temperatures are obtained with thicker coatings (500 µm and 2000 µm), which promote heat loss reductions during the combustion and BSFC improvements. However, the thicker coatings present also higher wall temperatures during the intake and compression phases which can cause an increment in the inducted air temperature and deterioration in engine emissions. On the other hand, thinner coatings (60 µm and 100 µm) present minor potential in heat loss reduction, due to their lower wall temperatures during combustion, but a limited risk of the intake air heating.

Figure 3.15 displays the trend of the increment in NO_x emissions as a function of the coating thickness. NO_x emissions tend to increase using thicker coatings, because of the higher wall temperatures. Accordingly, the optimal thickness of the anodized aluminum TBC should be in the range of 60 µm – 200 µm, as confirmed in [50,52,59].

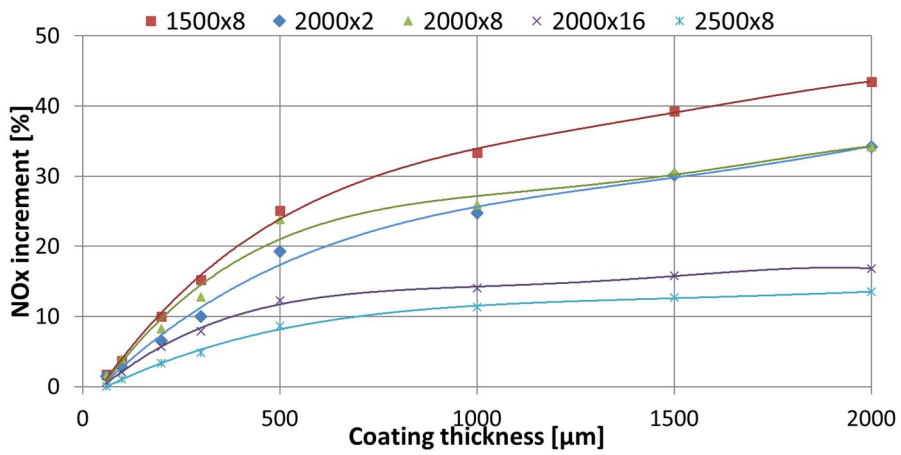

Figure 3.15 - Effects of piston coating thickness (anodized aluminum) on NO_x emissions

3.3.2 Yttria-Partially Stabilized Zirconia (Y-PSZ) TBC

As described in *Section 2.1.2*, Partially Stabilized Zirconia (PSZ) has been the most widely used ceramic material in past research works as TBC. Usually, it was employed in a doped form, with the addition of Y_2O_3 or MgO, to stabilize the ZrO_2 base material.

Using the 1D CFD engine model, the Y-PSZ potential as piston TBC has been investigated and compared with that of the anodized aluminum. The thermo-physical characteristics of Y-PSZ and anodized aluminum used in the numerical study, are reported in Table 3.2.

Table 3.2 - Thermo-physical properties of anodized aluminum [18] and Y-PSZ [60]

	Anodized aluminum	Y-PSZ
Density [$kg \cdot m^{-3}$]	1400	5650
Volumetric specific heat capacity [$kJ \cdot m^{-3} \cdot K^{-1}$]	1300	3500
Thermal conductivity [$W \cdot m^{-1} \cdot K^{-1}$]	0.67	1.4
TBC thickness [µm]	100	100

Figure 3.16 shows the piston wall temperature swings, resulting from the simulations at 2000 rpm and 8 bar of BMEP. Y-PSZ coating presents much lower wall temperature variations within the engine cycle respect to the anodized aluminum one. In particular, Y-PSZ produces lower wall temperature during the combustion phase, because of its higher conductivity, and it presents higher temperature during the intake stroke due to its greater heat capacity in comparison with the anodized aluminum.

The potentialities in Heat Transfer and BSFC reductions of both coatings are shown in Figure 3.17. The anodized aluminum TBC brings to more significant reductions in HT (until 5.6%) and BSFC (until 0.9%) due to its higher surface

temperature swings, and, for this reason, it was selected for the successive experimental research work.

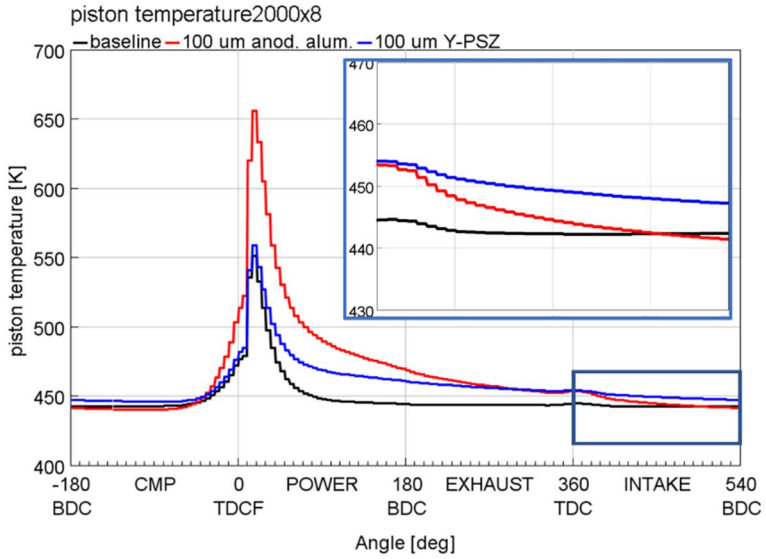

Figure 3.16 - Piston wall temperature swings (anodized aluminum and Y-PSZ)

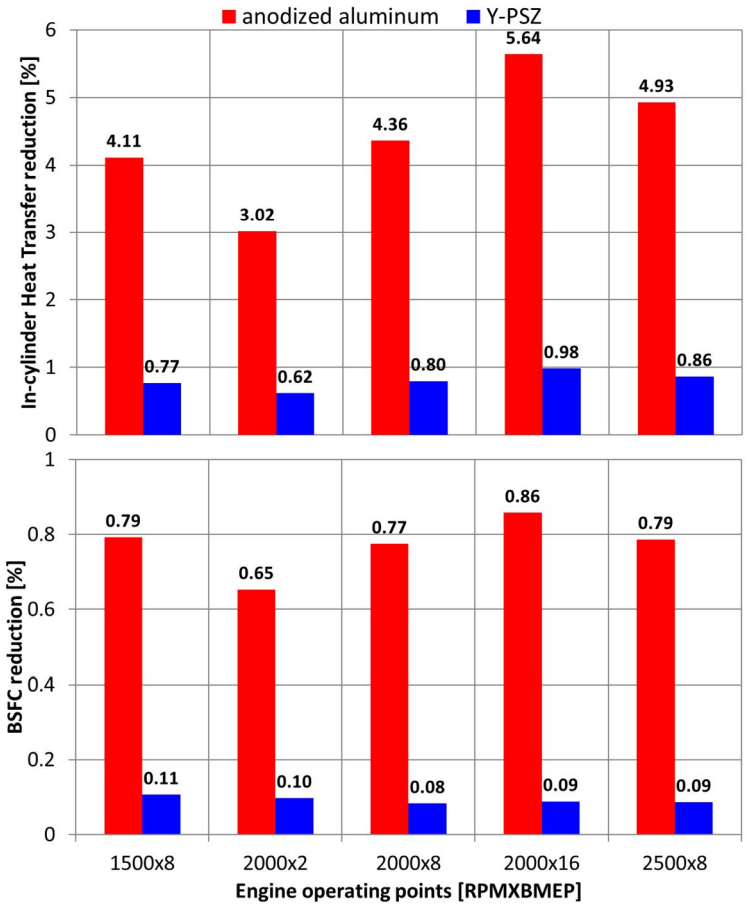

Figure 3.17 - In-cylinder Heat Transfer reductions (top) and BSFC reductions (bottom) in case of 100 µm anodized aluminum and Y-PSZ piston coatings

Chapter 4

Experimental analysis

Part of the work described in this Chapter has been submitted to "Applied Thermal Engineering", and at the time the Thesis was written it was in peer-review phase.

This *Chapter* includes the results of an experimental campaign carried out at the dyno test bench for assessing the potential of the piston coating technology applied on a 1.6-liter automotive diesel engine.

Anodized aluminum (with a thickness of 90 μm) has been chosen as piston TBC because of the promising results from the simulations. Piston Full Coated (PFC) configuration has been compared with a Baseline configuration equipped by standard aluminum pistons.

Two different tests were performed: Start of Injection (SOI) and Exhaust Gas Recirculation (EGR) Sweeps, for assessing the impact of the injection timing and EGR percentage respectively on the insulation technology effectiveness.

Fuel consumption and engine out emissions for both configurations are compared and discussed, analyzing the engine burn rates calculated from the in-cylinder pressure traces.

4.1 Experimental setup

4.1.1 Engine layout

The test engine is a prototype turbocharged automotive diesel engine with a dual loop (high + low pressures) cooled EGR system. The engine version used in this research presents an electronically actuated Variable Geometry Turbine (VGT), a Common Rail fuel injection system capable of 2000 bar maximum injection pressure, a chain-driven dual overhead camshaft. Engine block, cylinder head, and pistons are all made of aluminum alloy. The main specifications of the test engine are reported in Table 3.1 on page 31.

Two different sets of pistons were tested: a conventional aluminum non-insulated configuration (Baseline) and a fully insulated configuration (Piston Full Coated – PFC), where the full piston surface, including the bowl and the crown, was coated with anodized aluminum. The properties of the tested coating, reported in Table 4.1, are comparable to those used for the simulations, compatibly with the manufacturer availability. The TBC surface roughness was considerably higher than the original aluminum (R_a 8 µm vs. R_a 3.2 µm), because of its greater porosity.

Table 4.1 - Thermo-physical properties of the tested anodized aluminum

Material	Anodized Aluminum
Thermal conductivity	0.9 [$W \cdot m^{-1} \cdot K^{-1}$]
Surface roughness (R_a)	8 [µm]
TBC thickness	90 [µm]

The top views of the two piston configurations are shown in Figure 4.1.

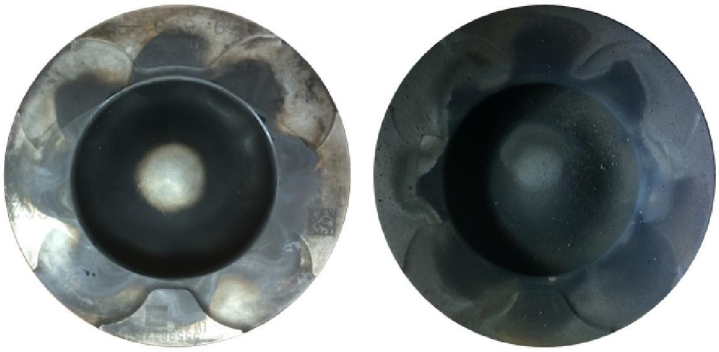

Figure 4.1 - Top views of the two piston configurations, after the experimental campaign

4.1.2 Facilities description

The experimental campaign was carried out at the Energy Department laboratory of Politecnico di Torino. The engine was tested in a dynamic test bench

featuring a three-phase asynchronous dynamometer with controlled cabin intake air temperature (25°C) and intake air humidity (50% RH).

The engine fuel consumption was measured by means of a continuous fuel mass flow meter (AVL ® KMA 4000); the engine-out and intake gas compositions (NO, NOx, HC, CO, CO_2, and O_2) were measured using AVL ® AMA i60, while a smoke meter (AVL ® 415S) was employed for the measurement of Filter Smoke Number (FSN) of the engine-out gas. Pressure sensors and thermocouples are also used in several points of the engine as intake and exhaust pipelines, EGR lines, coolant, oil and fuel circuits. The engine cooling was ensured by a coolant-to-water heat exchanger in which the cooling water flow was modulated by a Proportional Integral (PI) controlled valve to reach 90°C at the engine outlet. Similarly, an air-to-water intercooler was employed between the compressor and the intake manifold, to target a pre-defined cooler outlet temperature. A sketch of the engine layout is displayed in Figure 4.2.

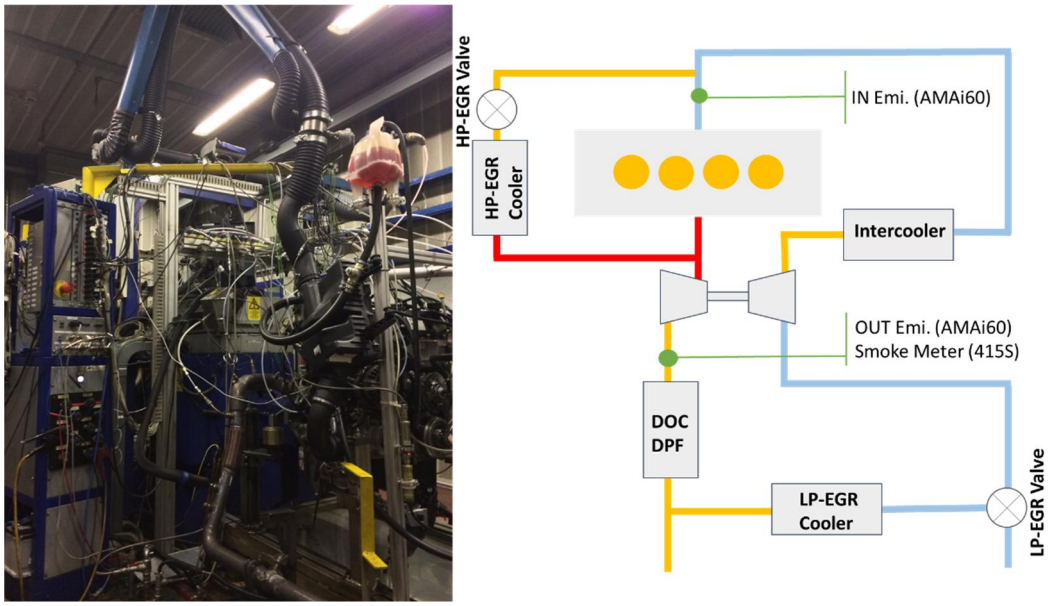

Figure 4.2 - Engine layout

Table 4.2 - Instrumentation precisions and linearities

Variable to measure	Sensors	Precision	Linearity
Fuel mass flow	AVL KMA 4000	0.1%	-
Torque	Dynamometer	0.3% FSO (525 Nm)	-
Gas analysis	AVL AMA i60	-	2%
FSN	AVL 415S	0.005 FSN + 3% meas. value	-
In-cylinder pressure	AVL GH13G	-	0.3% FSO

Furthermore, piezoelectric pressure sensors, mounted into the glow plug housings, are used for the measurement of the in-cylinder pressures, which are, then, acquired and post-processed employing AVL ® IndiCom software. All the engine parameters were modified by a PC, connected to the Engine Control Unit (ECU), using ETAS ® INCA software.

The precisions and linearities of the instrumentations are reported in Table 4.2.

4.1.3 Tests description

Two different tests were performed on both engine configurations and in different engine operating points, selected for covering the middle-high speeds and loads of the engine map: Start of Injection (SOI) sweep and Exhaust Gas Recirculation (EGR) sweep. Each test was repeated several times on different days to improve the robustness of the results.

The SOI sweep was used for evaluating the impact of the injection timing on the thermal insulation technology. It consists of a sweep of five SOI values, keeping constant the other calibration parameters (i.e., intake pressure, rail pressure). Furthermore, the pilot injection quantities and EGR rate were set to zero to lower uncertainties in the measurements.

The EGR sweep was used for assessing the effect of the Exhaust Gas Recirculation rate on the efficiency and the pollutant emissions of the LHRE. For all the operating points the SOI and the other calibration parameters were kept constant, and a sweep of five different EGR rates was performed. Regarding the injection event, the pilot quantities were set to zero. The test parameters are summarized in Table 4.3.

Table 4.3 – Test matrix

	Speed *[rpm]*	**BMEP** *[bar]*	**SOI Main** *[°CA bTDCF]*	**EGR** *[%]*
SOI SWEEP	1500	5	3.2 → 9.2	0
	2000	8	8.0 → 14.0	0
	2750	12	13.0 → 19.0	0
	2000	16	5.0 → 11.0	0
EGR SWEEP	1500	5	7.7	21 → 32
	2000	8	12.5	19 → 30
	2750	12	19.0	17 → 23
	2000	16	11.0	13 → 20

4.2 Results and discussions

4.2.1 Injection timing effect

Figure 4.3 shows the effect on the Indicated Specific Fuel Consumption (ISFC) of varying the injection timing for baseline and PFC configurations. In the experimental analysis, the indicated quantities are used, rather than the brake ones, for excluding the effects of small friction variations which could occur due to the pistons change. The average results over five tests are plotted in Figure 4.3. Tests were performed in different days and the relative standard deviations were calculated as:

$$\sqrt{\frac{\sum_{i=1}^{N}(x_i - \bar{x})^2}{(N-1)}} \tag{4}$$

where x_i are the measured values, $\bar{x}$ is the mean value and N is the number of measurements.

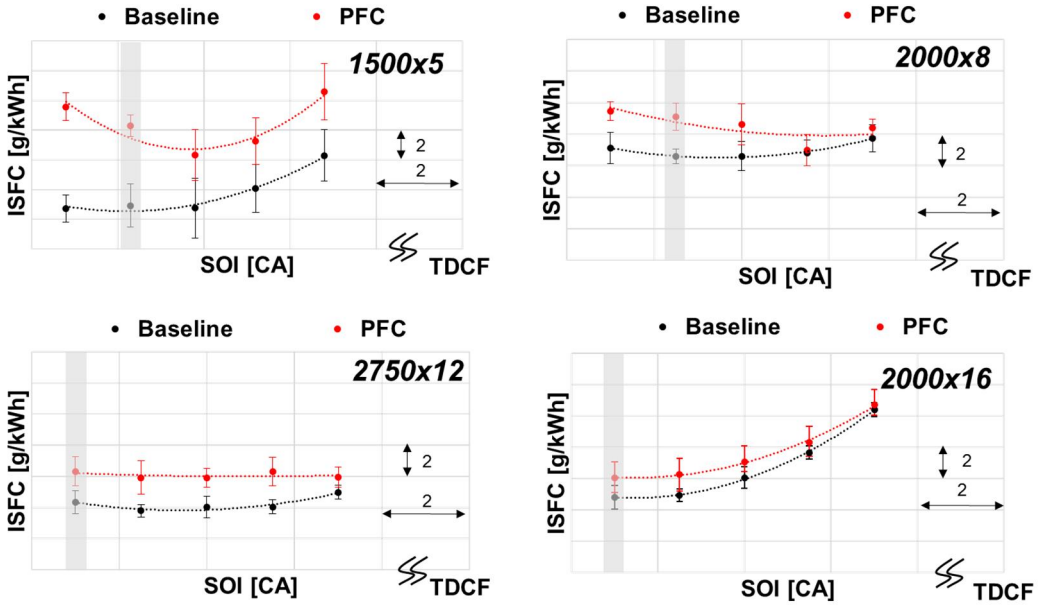

Figure 4.3 - SOI sweep at 1500x5, 2000x8, 2750x12 and 2000x16. Average values over 5 tests performed on different days. Grey bands highlight the points which were analyzed through the burn rates

Differently from the simulations, the worse indicated efficiency was obtained with the PFC configuration, particularly at the lower load and speed (1500x5), with ISFC increments greater than 2%. Increasing the load and speed, the gap between the two configurations decreases below 1%. Furthermore, Figure 4.3 displays that the optimum SOI (with the lower ISFC) shifts towards the Top Dead Center Firing (TDCF), passing from baseline to PFC configuration, or that in other words, PFC configuration exhibits a better tolerance to the late injection timings. For better understanding these phenomena, a deeper analysis of the burn rates was performed. Figure 4.4 shows the burn rates, calculated through the Cylinder Pressure Only Analysis (CPOA) of GT-POWER code, using the acquired in-cylinder pressures as input [61]. The burn rate differences between PFC and baseline configurations are also displayed. All the tested operating points exhibit a slight increase in the burn

rate at the first stage of combustion (during the premixed phase) when coated pistons are used. This behavior is caused by the reduced ignition delay of PFC probably due to the higher in-cylinder temperature at the beginning of combustion. Faster-premixed combustion can compensate for the adverse effect of a retarded injection timing, improving the tolerance to the late injection. Besides, in the cases of advanced injection timings, the burn rate increments take place when the piston is still in the compression phase, and so they are detrimental for the indicated efficiency improvement. Vice versa, in the cases of retarded injections, the burn rate increments occur during the expansion, promoting efficiency recoveries.

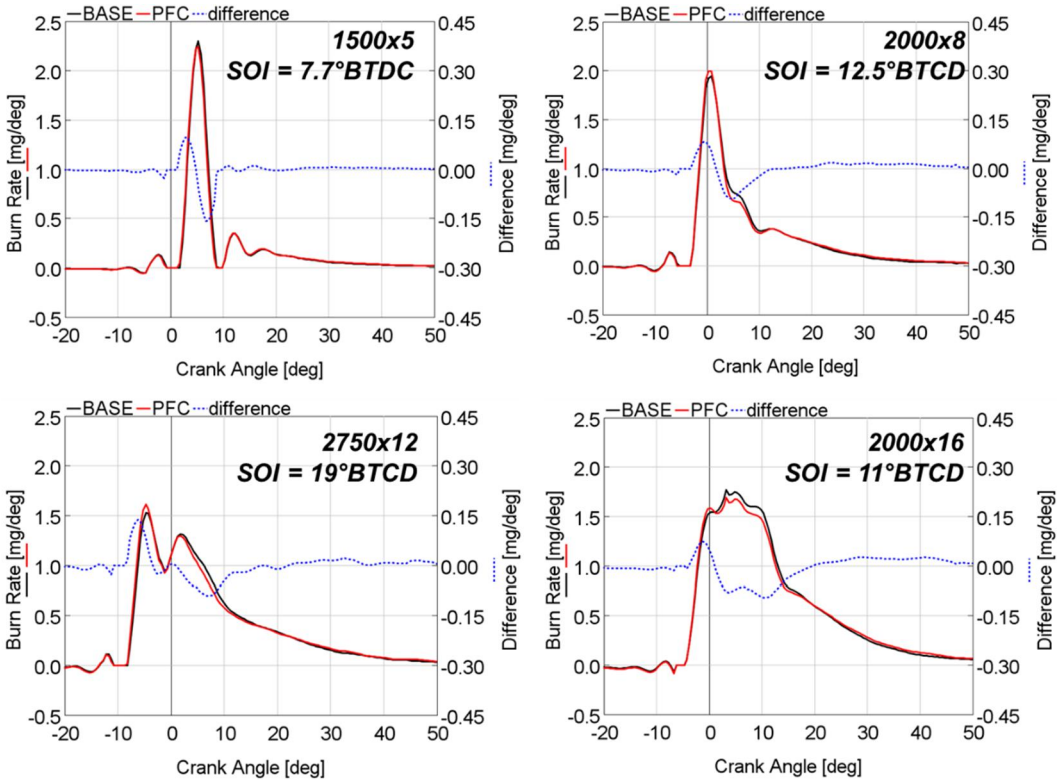

Figure 4.4 - Burn Rates at 1500x5, 2000x8, 2750x12 and 2000x16. Difference = PFC - BASE

Figure 4.4 also shows that PFC configuration presents a slower mixing-controlled combustion phase (explained by the negative burn rate differences in the first crank angles of the expansion stroke), and a consequent combustion shift towards the late phase. The slowdown of the mixing-controlled combustion, which is the main cause of the lower indicated efficiency of PFC, is probably due to the interaction between the flame and the rough walls of the TBCs. In detail, a high piston surface roughness provokes a slow-down of the mixture motion near the walls, increasing the mixture residence time in the piston bowl. Accordingly, high-temperature combustion gasses stay more time near the piston wall, increasing the engine heat loss [59].

Moreover, the porosity of the anodized aluminum TBC, especially if it is not conveniently sealed, can be detrimental for the engine efficiency for three main reasons, as discussed in [62]:

- Porous heat losses due to the mass flow of hot gasses inside the pores, generated from the high in-cylinder pressure during the compression and combustion. Moreover, a very high surface to volume ratio characterizes the pores which causes an increase in the heat flux.
- Extended heat release tails, due to the trapped fuel within or on the surface of the coating, which is avoided from burning until much later in the engine cycle.
- Reduced compression ratio generated from the porosity permeability.

Figure 4.5 shows the burned fuel fractions, calculated from the integration of the burn rates.

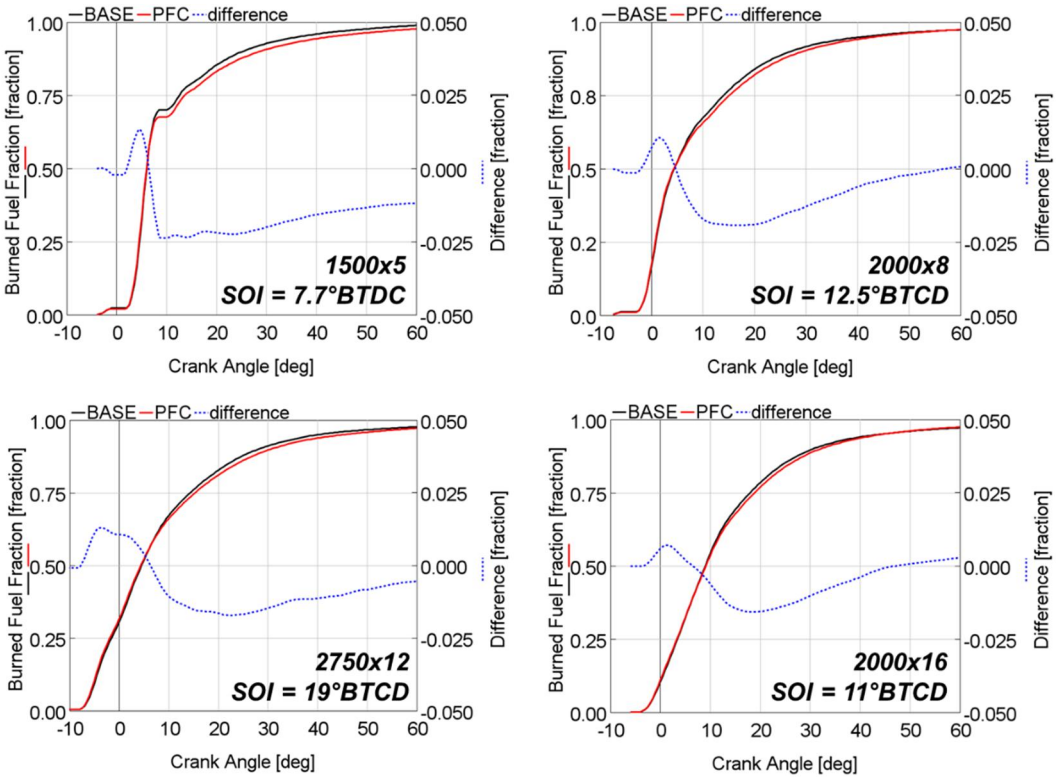

Figure 4.5 - Burned Fuel Fraction at 1500x5, 2000x8, 2750x12 and 2000x16. Difference = PFC - BASE

All the tested operating points exhibit faster-premixed combustion of PFC, due to the shorter ignition delay, and a slower mixing controlled combustion phase, due to the flame-wall interaction. Moreover, the final burned fuel fractions (at the end of combustion) are equivalent for both pistons configurations, and in all operating points, except for the 1500x5. Consequently, an increase in the unburned hydrocarbons (HC) emissions occurs at the lower-load operating point, as confirmed in Figure 4.6.

The trapped fuel within the pores of the coating can cause increased HC emissions at the lower-load operating point (1500x5).

In addition, indicated specific NO_x and soot emissions are reported respectively in Figure 4.7 and Figure 4.8. The soot concentrations (in mg/m^3) were calculated from the FSN values using the AVL empirical correlation [63].

Piston TBC technology does not influence the NO_x emissions, despite the supposed higher piston wall temperatures. This effect can be caused by the shorter ignition delay of PFC which can compensate for the increased wall temperature.

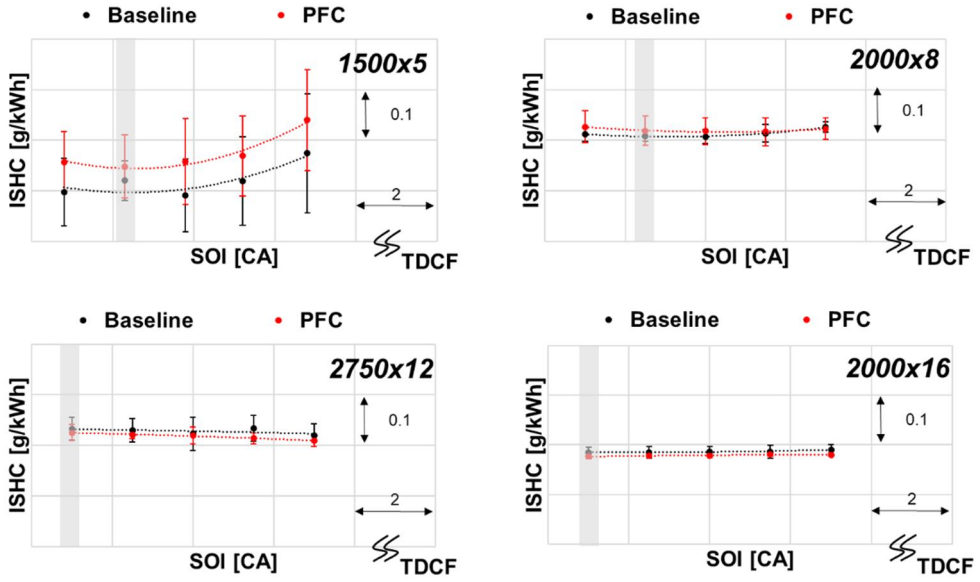

Figure 4.6 – HC emissions as a function of the injection timing at 1500x5, 2000x8, 2750x12 and 2000x16. Average values over 5 tests performed on different days. Grey bands highlight the points which were analyzed through the burn rates

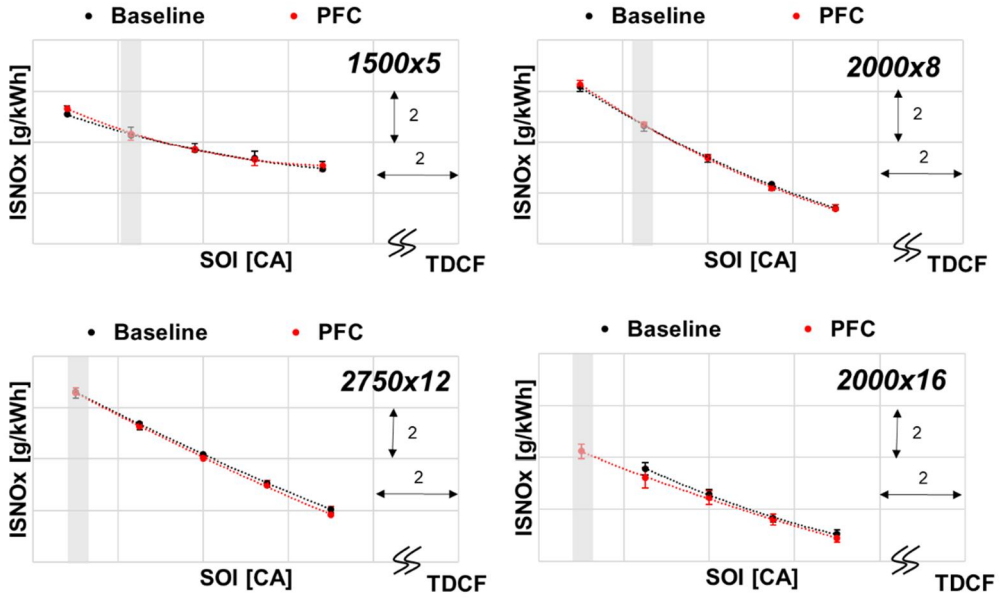

Figure 4.7 - NOx emissions as a function of the injection timing at 1500x5, 2000x8, 2750x12 and 2000x16. Average values over 5 tests performed on different days. Grey bands highlight the points which were analyzed through the burn rates

As far as the particulate emissions are concerned, the coated configuration presents higher Indicated Specific Soot values, especially at low-medium loads, probably caused by the interaction between the impinged spray and the rough surface of the coating, as shown in Figure 4.9. In case of a rough surface, the residence time of the mixture in the piston bowl becomes longer due to the lower

flow velocity at the wall. This phenomenon promotes an elevated equivalence ratio near the wall, with a consequent increase in soot emission [59].

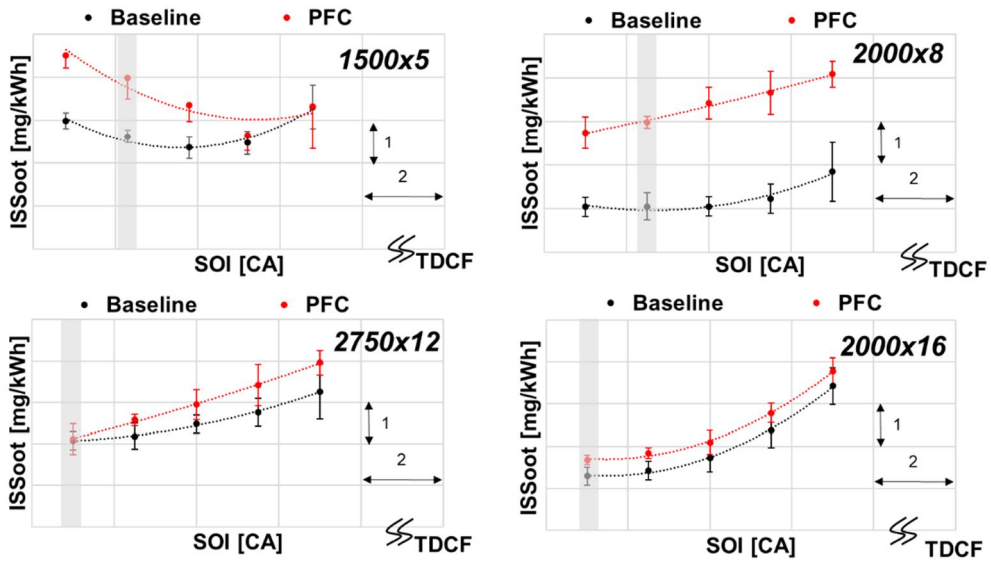

Figure 4.8 - Soot emissions as a function of the injection timing at 1500x5, 2000x8, 2750x12 and 2000x16. Average values over 5 tests performed on different days. Grey bands highlight the points which were analyzed through the burn rates

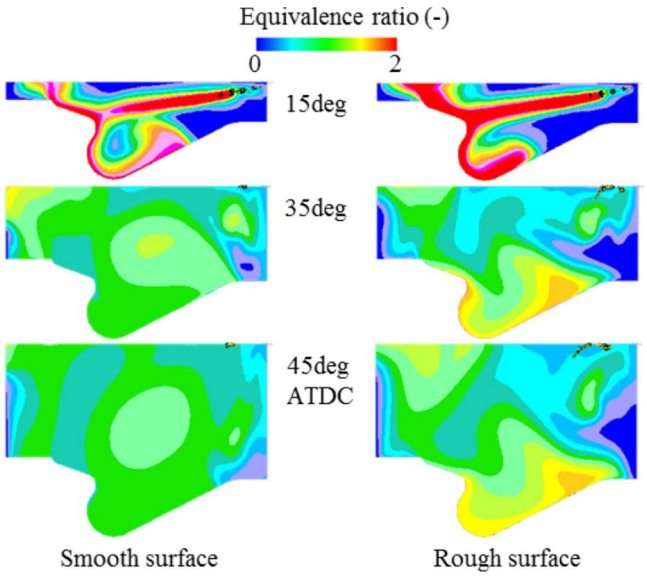

Figure 4.9 – Equivalence ratio by CFD simulations on a similar engine [59]

Finally, the trend of CO emissions is similar to that of HC, see Figure 4.10. A significant increase in CO emissions occurs only at lower load, where the combustion worsening and the reduction of the burned fuel fraction are more evident, while at medium and higher loads, CO emissions are almost constant.

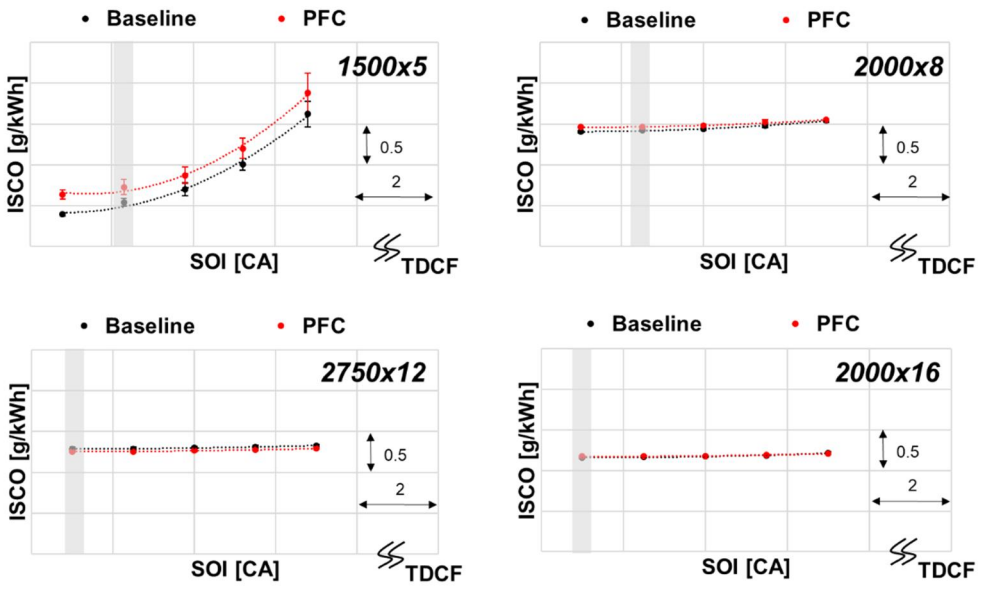

Figure 4.10 - CO emissions as a function of the injection timing at 1500x5, 2000x8, 2750x12 and 2000x16. Average values over 5 tests performed on different days. Grey bands highlight the points which were analyzed through the burn rates

4.2.2 Exhaust gas recirculation effect

EGR sweeps were conducted to assess the impact of the Exhaust Gas Recirculation on the piston insulation technology. Figure 4.11 displays the trade-off curves ($ISNO_x$-ISFC) obtained with EGR sweeps.

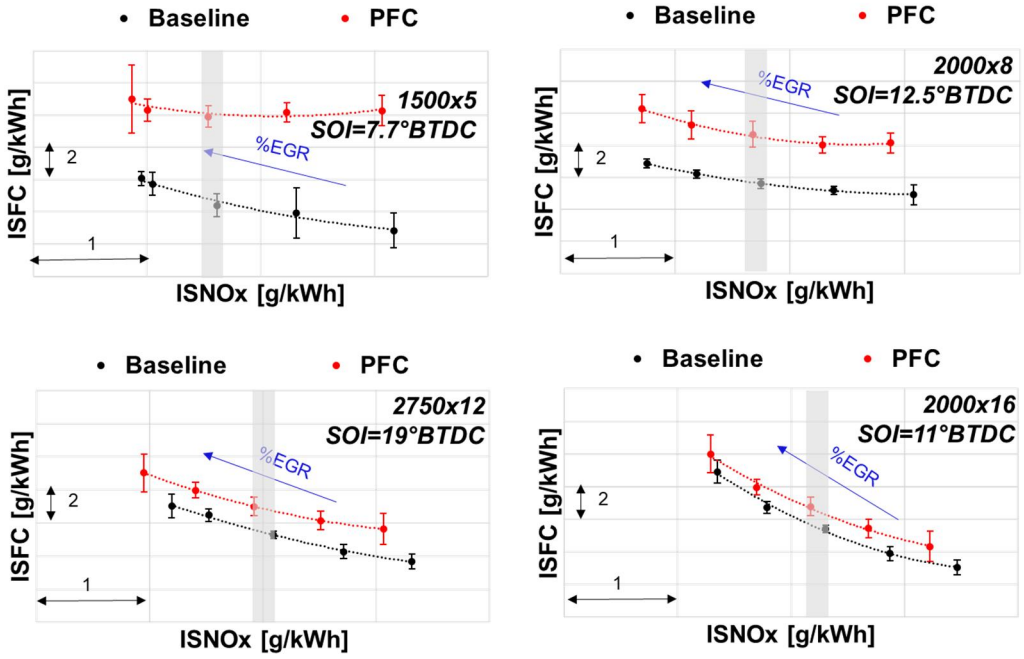

Figure 4.11 - EGR sweep at 1500x5, 2000x8, 2750x12 and 2000x16. Average values over 5 tests performed on different days. Grey bands highlight the points which were analyzed through the burn rates

As for the SOI sweeps, the indicated efficiency gets worse using the coated pistons, especially at lower load where the ISFC raises up to 7 g/kWh. At 2000x16,

the ISFC increments turn out to be in the order of 1 g/kWh. Furthermore, PFC seems to be more tolerant to the EGR at lower load, since the ISFC increment is less pronounced at higher EGR rates. A more in-depth analysis of the burn rates is presented in Figure 4.12. The PFC configuration presents a shorter ignition delay and a faster initial stage of combustion (premixed), probably due to the hotter piston surface. Therefore, it can partially compensate for the increased ignition delay caused by the recirculated burned gas, promoting its better tolerance to the EGR. The EGR tolerance is more evident only at the lower load (1500x5) probably for the retard injection event (SOI = 7.7°BTDC) which makes the timing losses more important.

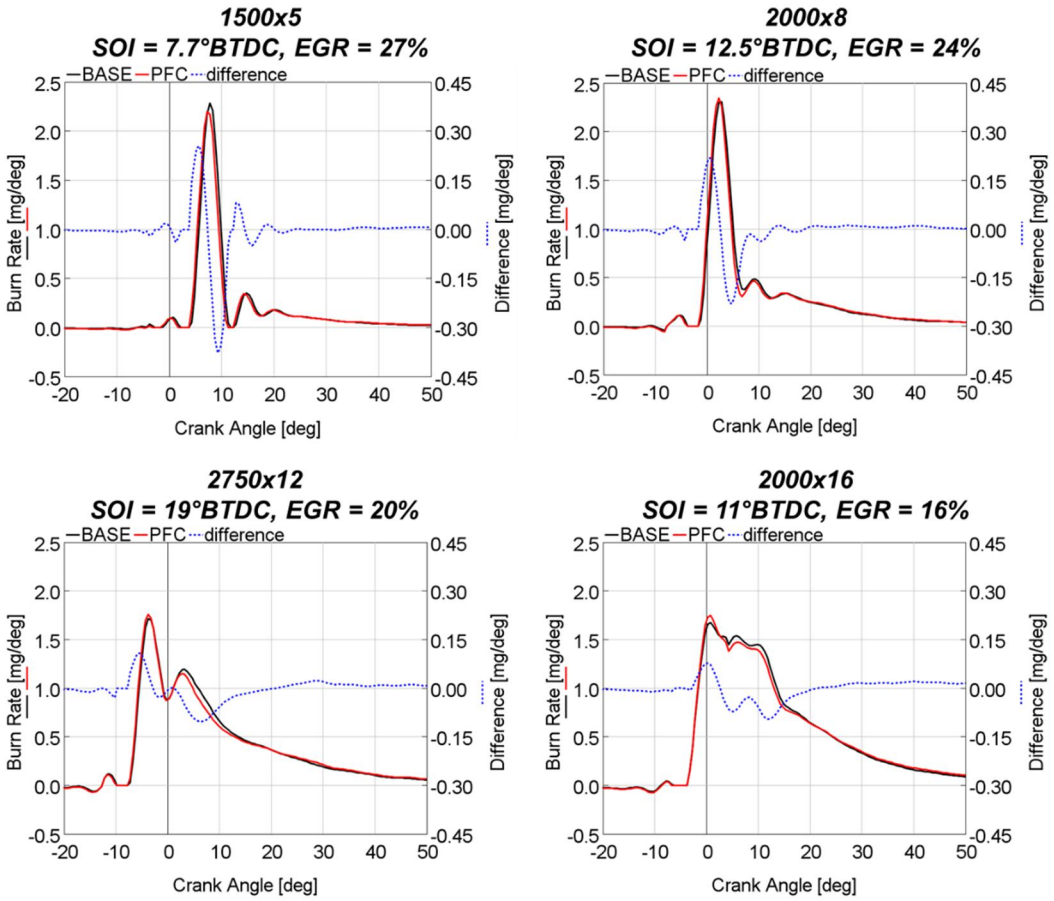

Figure 4.12 - Burn Rate at 1500x5, 2000x8, 2750x12 and 2000x16, w/EGR. Difference = PFC - BASE

In addition to the faster initial stage of combustion, PFC also exhibits a slow-down in the premixed combustion and a shift of the burned fuel fraction towards the late combustion phase, which are detrimental for the indicated efficiency. As described above, the main causes of the delayed combustion can be attributed to the coating characteristics, in terms of roughness and porosity.

A comparison of the burned fuel fractions is shown in Figure 4.13. At 1500x5, a noticeable difference in burned fuel fraction is still present during the late combustion phase (around 60°ATDC), causing increases in unburned hydrocarbons and CO emissions, as confirmed in Figure 4.14 and Figure 4.15.

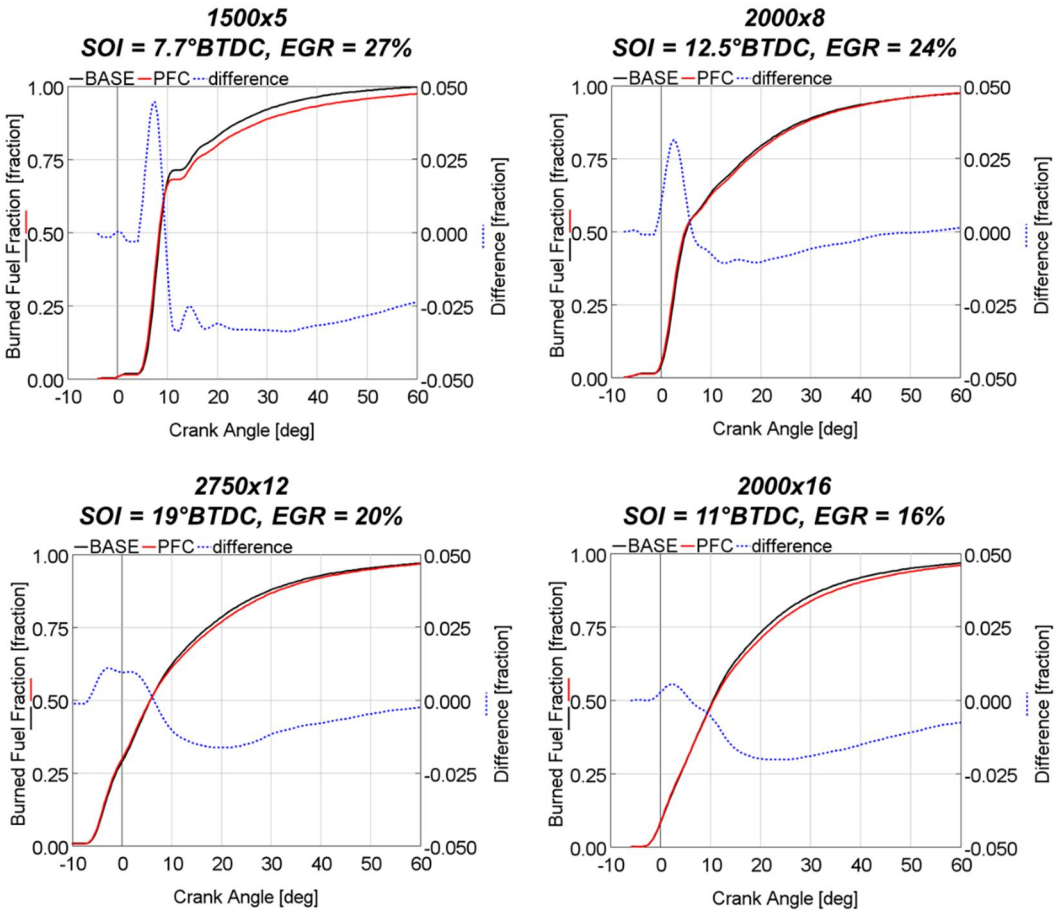

Figure 4.13 – Burned Fuel Fraction at 1500x5, 2000x8, 2750x12 and 2000x16, w/EGR. Difference = PFC – BASE

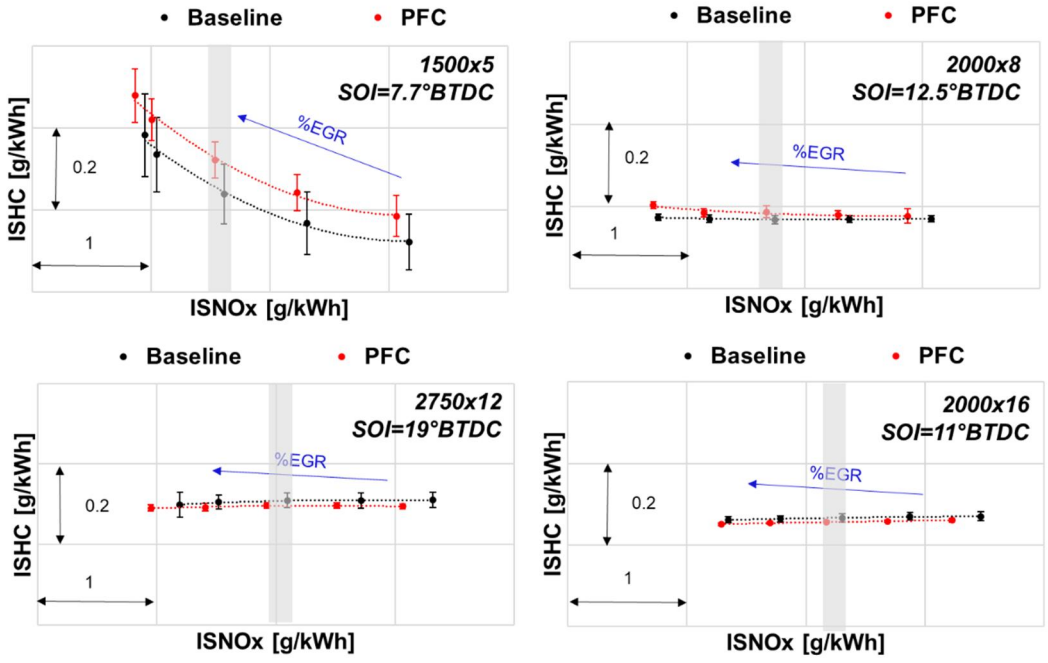

Figure 4.14 – ISNOx-ISHC trade-offs at 1500x5, 2000x8, 2750x12 and 2000x16. Average values over 5 tests performed on different days. Grey bands highlight the points which were analyzed through the burn rates

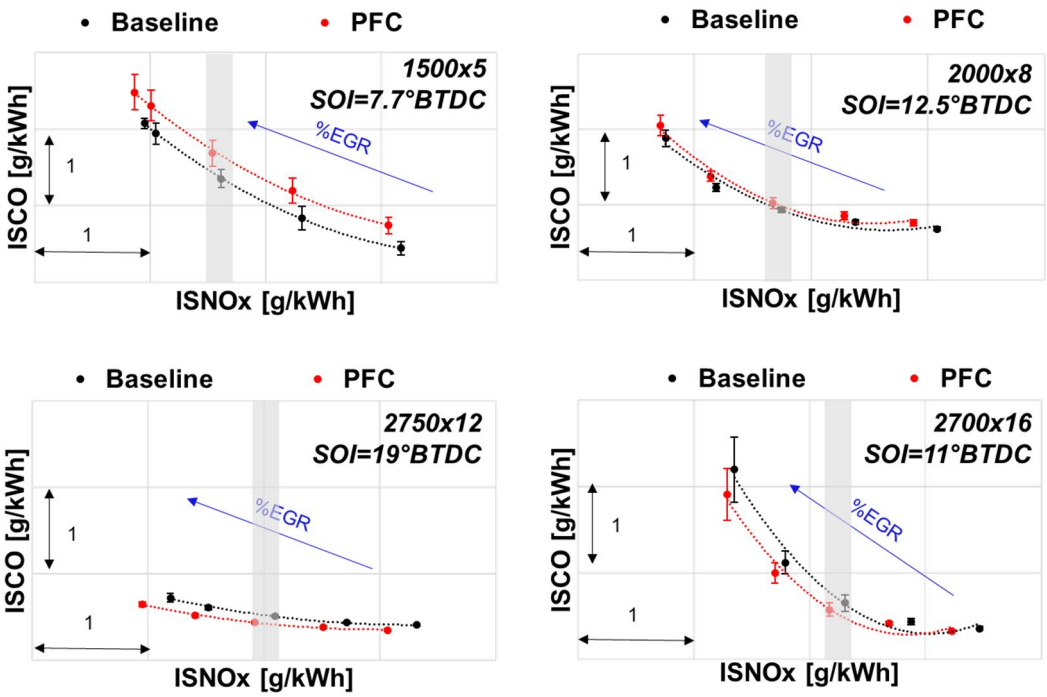

Figure 4.15 - ISNO$_x$-ISCO trade-offs at 1500x5, 2000x8, 2750x12 and 2000x16. Average values over 5 tests performed on different days. Grey bands highlight the points which were analyzed through the burn rates

The trade-offs NOx-SOOT, obtained through the EGR sweeps are shown in Figure 4.16. At the lower load (1500x5), the Indicated Specific Soot emissions are slightly higher in the case of PFC, probably due to the worst combustion efficiency and the mixture-wall interaction during the soot oxidation process (as illustrated in Figure 4.9), while, at the medium and high loads, where the indicated efficiencies and burn rates are comparable for both configurations, the soot emissions are generally unchanged.

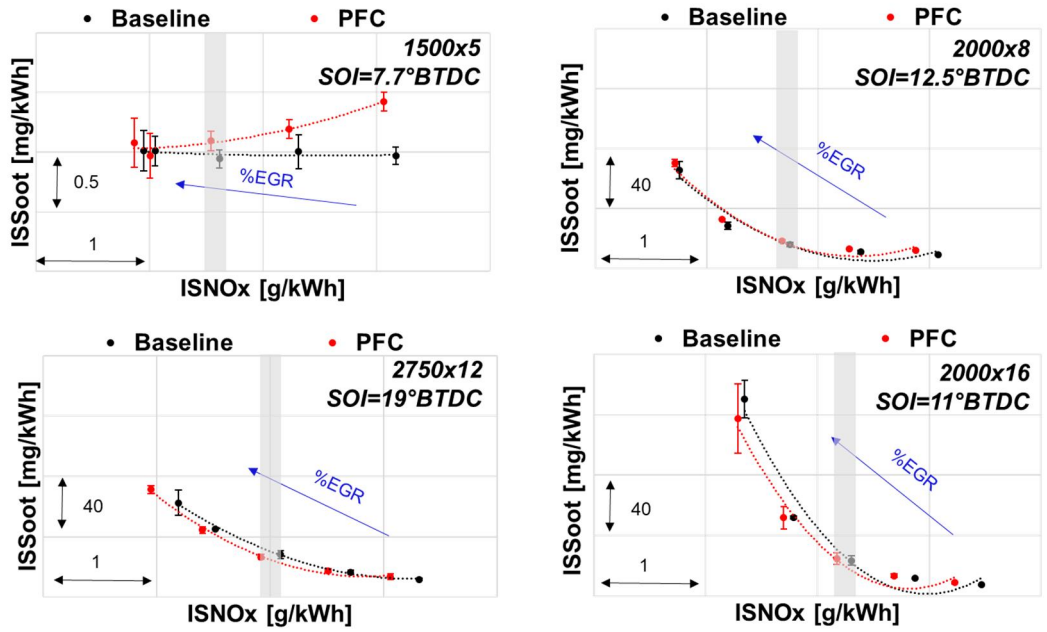

Figure 4.16 - ISNO$_x$-ISSoot trade-offs at 1500x5, 2000x8, 2750x12 and 2000x16. Average values over 5 tests performed on different days. Grey bands highlight the points which were analyzed through the burn rates

Vice versa, small reductions in the Indicated Specific NO_x emissions occur in all the tested operating points, because of the shorter ignition delay of PFC.

Conclusions

In this *Thesis*, the effects of using Thermal Barrier Coatings to exploit the Low Heat Rejection Engine concept in a passenger car diesel engine have been evaluated employing both numerical simulation and experimental tests on a prototype engine.

The review of the state-of-the-art TBCs technologies has allowed identifying a large number of mechanical, chemical and thermo-dynamical issues related to this technology. In the automotive research field ceramics, and in particular zirconia, have been the most extensively employed material for LHREs. In addition to the traditional TBCs, a new kind of coatings, based on the so called "thermal swing" concept has been studied. This concept is based on the reduction of the temperature difference between the gas and the coated surfaces during the entire engine cycle, which helps in achieving the engine thermal losses reduction without any negative impacts on engine volumetric efficiency and pollutant emissions. The innovative TBCs must exhibit very low thermal inertia and conductivity to be able to heat up and cool down very quickly following the gas temperature. Moreover, low-density and high-porosity are key factors for the innovative coating because of their direct impact on heat capacity and conductivity. Anodized aluminum, which is characterized by these two properties, resulted in the most promising material, despite of its high costs and long time necessary for the coating deposition.

Successively, a numerical 1D CFD model of a 1.6 l diesel engine has been used to evaluate the most promising thermal insulation technologies for the engine efficiency enhancement and the heat loss reduction.

The investigation of the complete and ideal insulation of the engine components (piston, firedeck, liner, and valves) has pointed out that piston insulation results to be the most efficient technology for improving BSFC (ideally up to 10%), due to its high potential in heat transfer reduction (45%). These results can be explained by the greater surface of the piston exposed to the in-cylinder gas during the combustion if compared with the other components. Furthermore, the combustion is intentionally directed towards the piston, causing higher turbulence and temperature near its surface and, consequently, a greater heat flux through this component.

Afterwards, the numerical analysis has been addressed to the evaluation of the most efficient piston TBC, using a lumped-mass thermal model directly coupled with the engine model. The simulations of anodized aluminum TBC have shown on average 0.8% in BSFC improvement and 5% in heat transfer reduction if a thickness of 100 μm is used.

The effect of the TBC thickness on the engine efficiency was also evaluated using the numerical model. Higher wall temperature peaks are obtained with thicker coatings, which lead to more important reduction in heat flux and in BSFC. However, the thicker coatings present higher wall temperatures during the intake and compression phases which cause increments in intake air temperature and

engine out NO_x emissions. Vice versa, thinner coatings present minor benefits for heat loss and BSFC reductions, due to their lower wall temperature peaks, but limited risk of intake air heating. Consequently, the optimal thickness for an anodized aluminum TBC should not exceed 200 μm.

The potential of a traditional TBC, like Y-PSZ, characterized by much higher thermal conductivity and heat capacity than anodized aluminum, has also been investigated using the numerical model. As expected, Y-PSZ piston coating has shown lower potentials in heat loss and BSFC reductions due to its lower wall temperature swings if compared with the anodized aluminum TBC.

The simulation outputs were successively used to set the guidelines for designing the theoretically most suitable piston TBC, which was then tested on a real automotive application.

The last part of the *Thesis* focuses on the results of an experimental campaign carried out on a prototype automotive diesel engine, for evaluating the effects deriving from the use of full coated pistons, respect to the traditional ones (aluminum-made).

The engine tests showed that, differently from the simulations, a worse indicated efficiency was obtained with the coated piston configuration, especially at the lower load and speed (1500x5), where ISFC increments greater than 2% were observed, while at the higher loads, the difference between the two configurations was considerably reduced below 1%.

The burn rates of coated configuration have shown shorter ignition delays, probably due to the higher in-cylinder temperatures at the beginning of combustion, which promote more advanced premixed combustion. This phenomenon resulted beneficial for the indicated efficiency only with retarded injection events, when the combustion begins after the TDCF, and with higher EGR rates.

Furthermore, the burn rate analysis has revealed that the coated configuration presents a slower mixing-controlled combustion phase, and a consequent combustion shift towards the late combustion phase, which are the main causes of the indicated efficiency worsening. The higher surface roughness and porosity of the coating (R_a 8 μm of coating vs. R_a 3.2 μm of aluminium) may have an effect in the combustion slowdown for different reasons [59,62]:

- Increased heat losses due to the lower flame velocity near the piston walls and longer residence time of the mixture into the piston bowl;
- increased heat losses due to the mass flow of hot gasses inside the pores;
- trapped fuel within or on the surface of the coating, which is avoided from burning until much later in the engine cycle;
- reduced compression ratio generated from the porosity permeability.

The surface roughness and porosity can also be responsible for the increased soot, unburned hydrocarbons and CO emissions at lower load (1500x5) due to:

- the increased equivalence ratio near the piston wall, produced by the slower flame velocity;

- the reduced burned fuel fraction at the end of combustion, caused by the trapped fuel within the pores of the coating, which promotes the formation of the incomplete combustion products (as CO and HC).

In addition, the analysed piston TBC does not affect the NO_x emissions, despite the supposed higher piston wall temperature. This effect could probably be ascribed to the ignition delay reduction, which even supports a NO_x reduction in case of high EGR rates.

Furthermore, the differences between the numerical predictions and the experimental results could be ascribed to side effects of the coating on the in-cylinder flow and combustion (i.e., due to the surface roughness and porosity) which cannot be captured with 1D CFD models, and would require further investigations by means of 3D CFD simulations.

In conclusion, the main outcomes of this *Thesis* can be summarized in the following points:

- Considering the high costs and the long time required by the coating deposition process, the use of TBC should be limited to the piston only, because it has exhibited the greater benefit in term of engine efficiency.
- TBC applied on the piston bowl is detrimental for the engine efficiency due to the interaction between the impinged fuel spray and the rough coating surface, therefore the use of TBC should be limited to the piston crown only.
- Effective TBCs should be characterized by low thermal conductivity and heat capacity, combined with small thickness, in order to exploit higher wall temperature swing, which promotes reduction in heat loss without penalties in term of volumetric efficiency and pollutant emissions.
- An opportune sealing of the coating pores is fundamental for reducing the coating surface roughness and porosity, which are both detrimental for engine efficiency and pollutant emissions (especially soot and unburned hydrocarbons).
- Even though not deeply analysed in this *Thesis,* the cost-benefit issue of TBCs could be overcome by combining LHRE with new engine calibration strategies, exploiting the reduced need for catalyst heating thanks to the higher exhaust gas temperatures.

References

[1] FEV, Future Mobility Contribution of Advanced Internal Combustion Engines, Turin, 2018.

[2] U. Tietge, CO2 emissions from new passenger cars in the EU: Car manufacturers' performance in 2017, ICCT. (2018). https://www.theicct.org/publications/co2-emissions-new-passenger-cars-eu-car-manufacturers-performance-2017.

[3] Z. Yang, Fuel-efficiency technology trend assessment for LDVs in China : Transmission Technology, (2018).

[4] ICCT, Shifting Gears: The Effects of a Future Decline in Diesel Market Share on Tailpipe CO2 and NOx emissions in Europe, (2017).

[5] EEA, No improvements on average CO2 emissions from new cars in 2017 — European Environment Agency, (2018). https://www.eea.europa.eu/highlights/no-improvements-on-average-co2 (accessed March 19, 2019).

[6] ACEA, CO2 from new cars up as petrol overtakes diesel, 2017 data shows, (2018).

[7] U. Tietge, 2017 year in review: European diesel down, electric vehicles on the rise, (2018). https://www.theicct.org/blog/staff/2017-year-review-european-diesel-down-electric-vehicles-rise (accessed March 19, 2019).

[8] Jato, CO2 Emissions rise to highest average since 2014, 2019. https://www.jato.com/wp-content/uploads/2019/03/CO2-Europe-2018-Release-Final.pdf.

[9] Fuels Institute, Tomorrow's Vehicles – A projection of transportation fuel demand through 2025, (2017). http://www.fuelsinstitute.org/ResearchArticles/Tomorrows Vehicles Brief.pdf.

[10] ICCT, Estimated cost of emission reduction technologies for LDVs, 2012.

[11] ICCT, Diesel Technology Developments, (2017).

[12] J. Dornoff, J. Miller, P. Mock, U. Tietge, The European Commission regulatory proposal for post-2020 CO 2 targets for cars and vans: A summary and evaluation, ICCT. (2017). https://www.theicct.org/sites/default/files/publications/ICCT_EU-CO2-proposal_briefing_20180109.pdf.

[13] U. Dornoff, J., Miller, J., Mock, P., Tietge, The European Commission regulatory proposal for post-2020 CO 2 targets for cars and vans: A summary and evaluation, Icct. (2017).

[14] J.B. Heywood, Internal Combustion Engine Fundamentals, Internatio, 1988.

[15] X.Q. Cao, R. Vassen, D. Stoever, Ceramic materials for thermal barrier coatings, J. Eur. Ceram. Soc. (2004). doi:10.1016/S0955-2219(03)00129-8.

[16] R. Vaßen, M.O. Jarligo, T. Steinke, D.E. Mack, D. Stöver, Overview on advanced thermal barrier coatings, Surf. Coatings Technol. (2010). doi:10.1016/j.surfcoat.2010.08.151.

[17] H. Kosaka, Y. Wakisaka, Y. Nomura, Y. Hotta, M. Koike, K. Nakakita, A. Kawaguchi, Concept of "Temperature Swing Heat Insulation" in Combustion Chamber Walls, and Appropriate Thermo-Physical Properties for Heat Insulation Coat, SAE Int. J. Engines. 6 (2013) 142–149.

doi:10.4271/2013-01-0274.
[18] Y. Wakisaka, M. Inayoshi, K. Fukui, H. Kosaka, Y. Hotta, A. Kawaguchi, N. Takada, Reduction of Heat Loss and Improvement of Thermal Efficiency by Application of "Temperature Swing" Insulation to Direct-Injection Diesel Engines, SAE Int. J. Engines. 9 (2016) 1449–1459. doi:10.4271/2016-01-0661.
[19] K. Kokini, Y.R. Takeuchi, B.D. Choules, Surface thermal cracking of thermal barrier coatings owing to stress relaxation: Zirconia vs. Mullite, Surf. Coatings Technol. (1996). doi:10.1016/0257-8972(95)02647-9.
[20] S. Rangaraj, K. Kokini, Interface thermal fracture in functionally graded zirconia-mullite-bond coat alloy thermal barrier coatings, Acta Mater. (2003). doi:10.1016/S1359-6454(02)00396-8.
[21] M. Azadi, G.H. Farrahi, A. Moridi, Optimization of air plasma sprayed thermal barrier coating parameters in diesel engine applications, J. Mater. Eng. Perform. (2013). doi:10.1007/s11665-013-0629-5.
[22] A. Gilbert, K. Kokini, S. Sankarasubramanian, Thermal fracture of zirconia-mullite composite thermal barrier coatings under thermal shock: A numerical study, Surf. Coatings Technol. (2008). doi:10.1016/j.surfcoat.2008.08.003.
[23] T. Kogo, Y. Hamamura, K. Nakatani, T. Toda, A. Kawaguchi, A. Shoji, High Efficiency Diesel Engine with Low Heat Loss Combustion Concept - Toyota's Inline 4-Cylinder 2.8-Liter ESTEC 1GD-FTV Engine -, SAE Tech. Pap. (2016). doi:10.4271/2016-01-0658.
[24] A. Kawaguchi, H. Iguma, H. Yamashita, N. Takada, N. Nishikawa, C. Yamashita, Y. Wakisaka, K. Fukui, Thermo-Swing Wall Insulation Technology; - A Novel Heat Loss Reduction Approach on Engine Combustion Chamber, SAE Tech. Pap. (2016). doi:10.4271/2016-01-2333.Copyright.
[25] Oerlikon Metco, Atmospheric Plasma Spray, (n.d.). https://www.oerlikon.com/metco/en/products-services/coating-services/coating-services-thermal-spray/thermal-spray-processes/processes-atmospheric-plasma/ (accessed January 15, 2019).
[26] Oerlikon Metco, High Velocity Oxygen (Gas) Fuel Spray, (n.d.). https://www.oerlikon.com/metco/en/products-services/coating-services/coating-services-thermal-spray/thermal-spray-processes/processes-hvof-gas-fuel/ (accessed January 15, 2019).
[27] J.W. Diggle, T.C. Downie, C.W. Goulding, Anodic oxide films on aluminum, Chem. Rev. (1969). doi:10.1021/cr60259a005.
[28] E.N. Pugh, G. Patermarakis, K. Moussoutzanis, Mathematical Models for the Anodization Conditions and Structural Features of Porous Anodic Al2O3 Films on Aluminum, J. Electrochem. Soc. (1995). doi:10.1149/1.2048527.
[29] S. Dewitt, K. Thornton, Model for anodic film growth on aluminum with coupled bulk transport and interfacial reactions, Langmuir. (2014). doi:10.1021/la500782d.
[30] S. Liu, S. Tang, H. Zhou, C. Fu, Z. Huang, H. Liu, Y. Kuang, Fabrication of AAO films with controllable nanopore size by changing electrolytes and electrolytic parameters, J. Solid State Electrochem. (2013). doi:10.1007/s10008-013-2034-2.
[31] A.P. Li, F. Müller, A. Bimer, K. Nielsch, U. Gösele, Hexagonal pore arrays with a 50-420 nm interpore distance formed by self-organization in anodic alumina, J. Appl. Phys. (1998). doi:10.1063/1.368911.
[32] L. Zaraska, G.D. Sulka, J. Szeremeta, M. Jaskuła, Porous anodic alumina

formed by anodization of aluminum alloy (AA1050) and high purity aluminum, Electrochim. Acta. (2010). doi:10.1016/j.electacta.2009.12.054.
[33] S. Luca, Anodizzazione dell'Alluminio, n.d. http://www.ing.unitn.it/~colombo/Anodizzazione/cap_3.htm.
[34] H. Tanaka, M. Fujita, T. Yamamoto, H. Muramatsu, H. Asoh, S. Ono, Anodizing method for aluminum alloy by using high-frequency switching electrolysis, SAE Tech. Pap. (2011) 2011–32. doi:10.4271/2011-32-0645.
[35] Swain Tech Coatings, Automotive Coatings Price Sheet, (n.d.). http://swaintech.com/race-coatings/automotive-coatings/automotive-coatings-price-sheet/ (accessed April 27, 2019).
[36] T. Morel, R. Keribar, A Model for Predicting Spatially and Time Resolved Convective Heat Transfer in Bowl-in-Piston Combustion Chambers, SAE Tech. Pap. (1985). doi:10.4271/850204.
[37] T. Morel, E.F. Fort, P.N. Blumberg, Effect of Insulation Strategy and Design Parameters on Diesel Engine Heat Rejection and Performance, SAE Tech. Pap. 850506 (1985). doi:10.4271/850506.
[38] T. Morel, S. Wahiduzzaman, E.F. Fort, Heat transfer experiments in an insulated diesel engine, SAE Tech. Pap. (1988). doi:10.4271/880186.
[39] M.J. Jennings, T. Morel, A Computational Study of Wall Temperature Effects on Engine Heat Transfer, SAE Tech. Pap. (1991). doi:10.4271/910459.
[40] T. Morel, R. Keribar, P.N. Blumberg, E.F. Fort, Examination of Key Issues in Low Heat Rejection Engines, SAE Tech. Pap. 860316 (1986). doi:10.4271/860316.
[41] D.N. Assanis, J.B. Heywood, Development and Use of a Computer Simulation of the Turbocompounded Diesel System for Engine Performance and Component Heat Transfer Studies, SAE Tech. Pap. 860329 (1986). doi:10.4271/860329.
[42] Y. Miyairi, Computer Simulation of an LHR DI Diesel Engine, SAE Tech. Pap. (1988). doi:10.4271/880187.
[43] D.D. Anderson, The Effects of Ceramic Port Insulation on Cylinder Head Performance in a Diesel Engine, SAE Tech. Pap. (1996). doi:10.4271/961745.
[44] P. Tamilporai, N. Baluswamy, P.M. Jawahar, S. Subramaniyam, S. Chandrasekaran, K. Vijayan, S. Jaichandar, J.J. Rani, K. Arunachalam, Simulation and Analysis of Combustion and Heat Transfer in Low Heat Rejection Diesel Engine Using Two Zone Combustion Model and Different Heat Transfer Models, SAE Tech. Pap. 2003-01–10 (2003). doi:10.4271/2003-01-1067.
[45] H. Jaaskelainen, M. W. Addy, In-Cylinder Thermal Barrier Coatings, (2015). https://www.dieselnet.com/tech/engine_coat.php (accessed January 17, 2019).
[46] G. De Paola, F. Rabeau, V. Knop, W. Willems, J.M. Zaccardi, Modelling investigation of design approaches for Low Heat Rejection Diesel Engines, in: SIA Powertrain, Rouen, 2016.
[47] J.R. Serrano, F.J. Arnau, J. Martin, M. Hernandez, B. Lombard, Analysis of Engine Walls Thermal Insulation: Performance and Emissions, SAE Tech. Pap. (2015). doi:10.4271/2015-01-1660.
[48] C. Binder, F. Abou Nada, M. Richter, A. Cronhjort, D. Norling, Heat Loss Analysis of a Steel Piston and a YSZ Coated Piston in a Heavy-Duty Diesel Engine Using Phosphor Thermometry Measurements, SAE Int. J. Engines.

(2017). doi:10.4271/2017-01-1046.
[49] N. Uchida, H. Osada, A New Piston Insulation Concept for Heavy-Duty Diesel Engines to Reduce Heat Loss from the Wall, SAE Int. J. Engines. (2017). doi:10.4271/2017-24-0161.
[50] D. Gatti, M. Jansons, One-Dimensional Modelling and Analysis of Thermal Barrier Coatings for Reduction of Cooling Loads in Military Vehicles, SAE Tech. Pap. (2018). doi:https://doi.org/10.4271/2018-01-1112.
[51] K. Uchihara, M. Ishii, H. Nakajima, Y. Wakisaka, A Study on Reducing Cooling loss in a Partially Insulated Piston for Diesel Engine, SAE Tech. Pap. (2018). doi:https://doi.org/10.4271/2018-01-1276.
[52] A. Poubeau, A. Vauvy, F. Duffour, J.-M. Zaccardi, G. de Paola, M. Abramczuk, Modeling investigation of thermal insulation approaches for low heat rejection Diesel engines using a conjugate heat transfer model, Int. J. Engine Res. 20 (2019) 92–104. doi:10.1177/1468087418818264.
[53] A. Broatch, P. Olmeda, X. Margot, J. Gomez-Soriano, Numerical simulations for evaluating the impact of advanced insulation coatings on H2 additivated gasoline lean combustion in a turbocharged spark-ignited engine, Appl. Therm. Eng. 148 (2019) 674–683. doi:10.1016/j.applthermaleng.2018.11.106.
[54] Gamma Technologies, GT-SUITE Flow Theory Manual, (2018).
[55] A. Piano, F. Millo, G. Boccardo, M. Rafigh, A. Gallone, M. Rimondi, Assessment of the Predictive Capabilities of a Combustion Model for a Modern Common Rail Automotive Diesel Engine, SAE Tech. Pap. (2016). doi:10.4271/2016-01-0547.
[56] A. Piano, F. Millo, L. Postrioti, G. Biscontini, A. Cavicchi, F.C. Pesce, Numerical and Experimental Assessment of a Solenoid Common-Rail Injector Operation with Advanced Injection Strategies, SAE Int. J. Engines. 9 (2016) 565–575. doi:10.4271/2016-01-0563.
[57] E.M. Afify, D.E. Klett, The Effect of Selective Insulation on the Performance, Combustion, and NO Emissions of a DI Diesel Engine, SAE Tech. Pap. (1996). doi:10.4271/960505.
[58] C.D. Rakopoulos, D.C. Rakopoulos, G.C. Mavropoulos, E.G. Giakoumis, Experimental and theoretical study of the short term response temperature transients in the cylinder walls of a diesel engine at various operating conditions, Appl. Therm. Eng. 24 (2004) 679–702. doi:10.1016/j.applthermaleng.2003.11.002.
[59] A. Kawaguchi, H. Iguma, H. Yamashita, N. Takada, N. Nishikawa, C. Yamashita, Y. Wakisaka, K. Fukui, Thermo-Swing Wall Insulation Technology; - A Novel Heat Loss Reduction Approach on Engine Combustion Chamber -, SAE Tech. Pap. (2016). doi:https://doi.org/10.4271/2016-01-2333.
[60] M. Durat, M. Kapsiz, E. Nart, F. Ficici, A. Parlak, The effects of coating materials in spark ignition engine design, Mater. Des. 36 (2012) 540–545. doi:10.1016/j.matdes.2011.11.053.
[61] Gamma Technologies, GT-SUITE Engine Performance Application Manual, (2018).
[62] P. Andruskiewicz, P. Najt, R. Durrett, R. Payri, Assessing the capability of conventional in-cylinder insulation materials in achieving temperature swing engine performance benefits, Int. J. Engine Res. 19 (2018) 599–612. doi:10.1177/1468087417729254.
[63] AVL, Avl Micro Soot Sensor Avl Exhaust Conditioning Unit Operating

Manual Product Guide, (2005).
[64] G. Woschni, A Universally Applicable Equation for the Instantaneous Heat Transfer Coefficient in the Internal Combustion Engine, SAE Tech. Pap. (1967). doi:10.4271/670931.
[65] Gamma Technologies, GT-SUITE Help Manual, (2018).

Appendix A

Predictive combustion model: DIPulse

As mentioned in *Chapter 3*, DIPulse predictive combustion model was implemented in the 1D CFD engine simulation code for the evaluation of the combustion burn rates. DIPulse model was developed by Gamma Technologies and is available in the simulation platform, GT-SUITE. It is based on the discretization of the cylinder contents in three thermodynamic parts, each with their temperature and composition: the Main Unburned Zone (MUZ), which includes all the air mass at intake valve closure, the Spray Unburned Zone (SUZ), which includes injected fuel and entrained gas, and Spray Burned Zone (SBZ), which contains the combustion products. The fundamental of the model is to follow the fuel history inside the cylinder: injection, evaporation, mixture with surrounding gas and burning [55]. The model can be applied to single or multiple injections, considering each injection event as a separate and independent pulse.

DIPulse model was calibrated on 28 engine operating points representative of different zones of the engine map: EGR area (lower loads), mid-load area and full load (see Figure A.1).

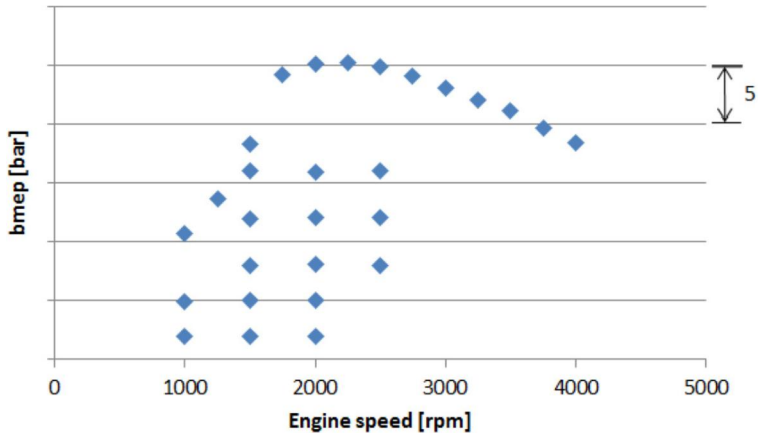

Figure A.1 – Operating points selected for the DIPulse calibration

The calibration was performed using a single cylinder model to reduce the time of the process. The calibration procedure allows to obtain a set of optimized calibration parameters, representative of the entire combustion process from spray penetration to diffusion combustion:

- Entrainment Rate Multiplier
- Ignition Delay Multiplier
- Premixed Combustion Rate Multiplier
- Diffusion Combustion Rate Multiplier

The goal of the calibration is to minimize the Improved Burn Rate RMS Error, which is the error between the burn rate predicted through the DIPulse and the experimental burn rate calculated from the measured in-cylinder pressure. Design of Experiment (DoE) method was employed to find the optimized calibration parameters, exploring 2000 set of combinations for each operating point.

In Figure A.2 are reported the validation results in terms of in-cylinder pressure and burn rate at different engine operating points. A good agreement between simulation results (red line) and experimental outputs (black line) was reached.

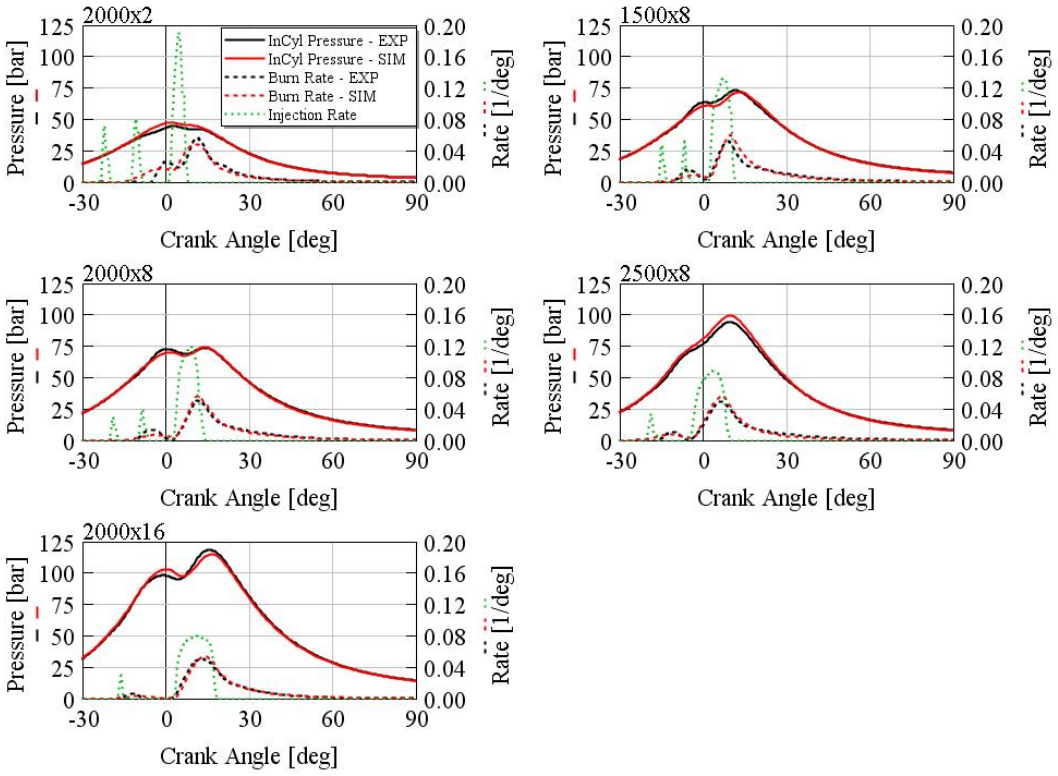

Figure A.2 - DIPulse combustion model results @ 5 different engine operating points – Experimental (black) and simulated (red) in-cylinder pressures (solid) and burn rates (dashed), injection mass flow rate (green dashed)

Satisfactory results were also obtained for the main combustion parameters, as displayed in Figure A.3. The DIPulse model can satisfactory reproduce the combustion process with errors which are lower than 5% on IMEP, 5 bar on maximum cylinder pressure, 2 degrees on MFB50 and crank angle of maximum cylinder pressure.

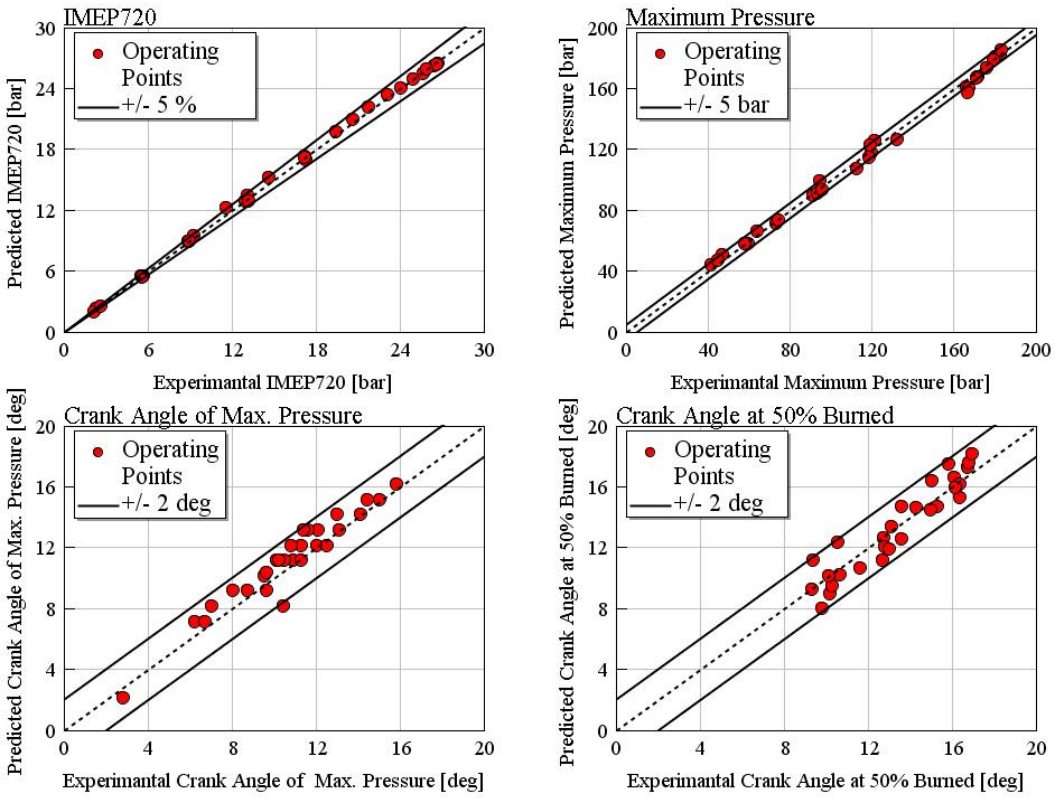

Figure A.3 - DIPulse combustion model results - Combustion parameters: IMEP (top-left), in-cylinder maximum pressure (top-right), crank angle of maximum pressure (bottom-left), crank angle at 50% fuel burned (bottom-right) (28 engine operating points)

After the DIPulse model calibration, the predictive NO_x emission model was implemented and calibrated using the experimental data.

The NO_x emission model is based on the extended Zeldovich mechanism [14] which includes the N_2 oxidation, N oxidation and OH reduction reactions described by Eq. 5, 6 and 7:

$$O + N_2 \leftrightarrow NO + N \quad (5)$$

$$N + O_2 \leftrightarrow NO + O \quad (6)$$

$$N + OH \leftrightarrow NO + H \quad (7)$$

The NO_x model calibration was performed using a DoE method to find the optimum set of the following parameters:

- NO_x Calibration Multiplier, that affects the NOx concentration;
- N_2 Oxidation Activation Energy Multiplier, that affects the reactions dependence on temperature.

Figure A.4 shows the model accuracy in the NO_x prediction. A satisfactory agreement between simulation and the experimental results has been reached in the low NO_x zone, corresponding to the operating points with high EGR rates.

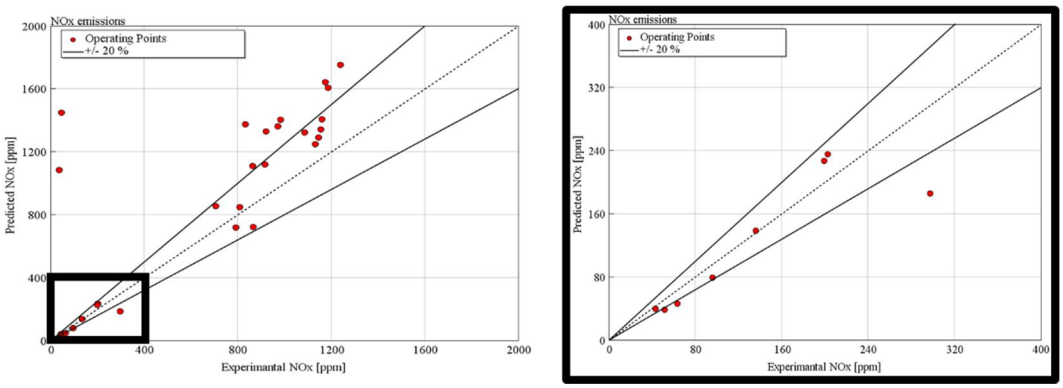

Figure A.4 - DIPulse combustion model results – NOx emissions: all operating points (left) and low NOx zone (right)

Appendix B

Effects of the convective heat transfer model

A sensitivity analysis on the convective heat transfer model was performed, comparing the Flow [36] model with that developed by Woschni [64], which is typically used in 1D CFD engine simulation. The main difference between the two models is that the Woschni model is based on an average cylinder gas velocity, while the Flow model is based on the in-cylinder gas motion, including swirl, and turbulence.

Figure B.1 shows the convective heat transfer coefficient and the heat transfer rate calculated with both the heat transfer models. The Flow model exhibits higher HTC around the TDC firing (0 CA deg), due to the model dependence on the in-cylinder gas velocity, swirl, and turbulence, which are particularly high in this engine cycle phase. Moreover, differences in HTC are also observed around the TDC scavenging (360 CA deg), where the Flow model takes into account the inflow gas through the intake valves and backflow gas through the exhaust valves, increasing the predicted HTC [65].

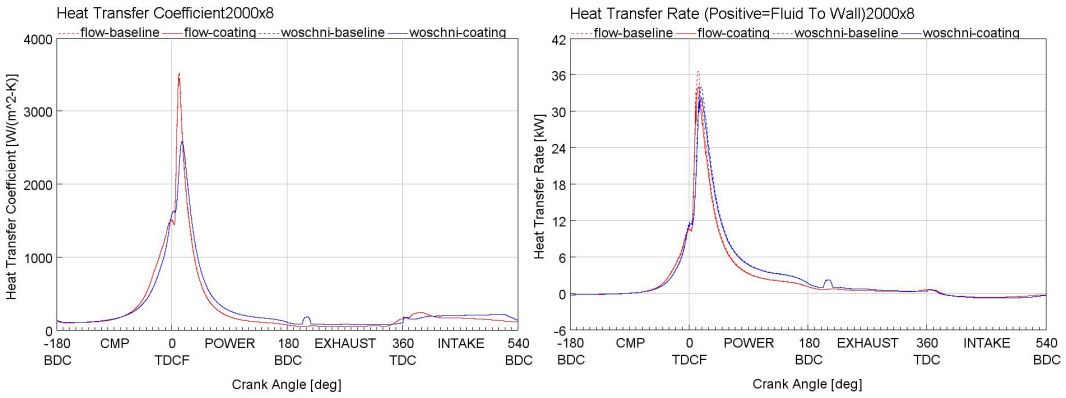

Figure B.1 - Heat Transfer Coefficients (left) and Heat Transfer Rates (right) calculated with Flow and Woschni models

Another important simulation outcome is that no important variations in convective HTCs have been found passing from the baseline to the piston coated configuration, which means that both the HT models do not take into account the wall temperatures for the HTC calculation. This hypothesis can lead to some inaccuracies in the results because the wall temperature can affect the heat transfer process, as discussed in the literature [38,39,44].

The heat transfer rates calculated from the two models are displayed in Figure B.1. For both models, the piston insulation produces a reduction of the heat transfer rate near the TDCF, due to the higher surface temperature of the coating (Figure B.2).

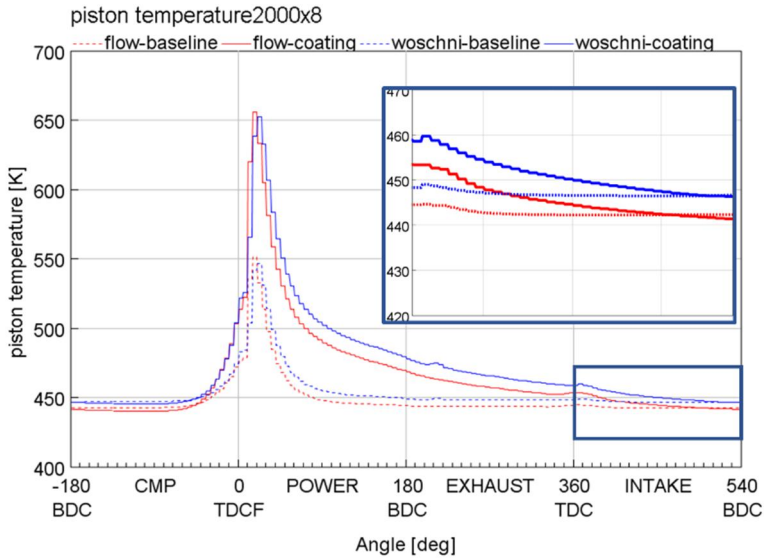

Figure B.2 - Piston wall temperature swings calculated with Flow and Woschni models

Moreover, the Flow model slightly overestimated the piston temperature swing, of about 10 K, in comparison with Woschni model.

The BSFC reductions deriving from the piston insulation are shown in Figure B.3. Woschni model tends to underestimate the piston insulation potentialities in improving engine efficiency. The main reason of this trend is the reduced share of the heat rejected through the piston predicted by Woschni model (as illustrated in Figure B.4), which can lead to estimate lower potential in heat transfer reduction using piston TBCs.

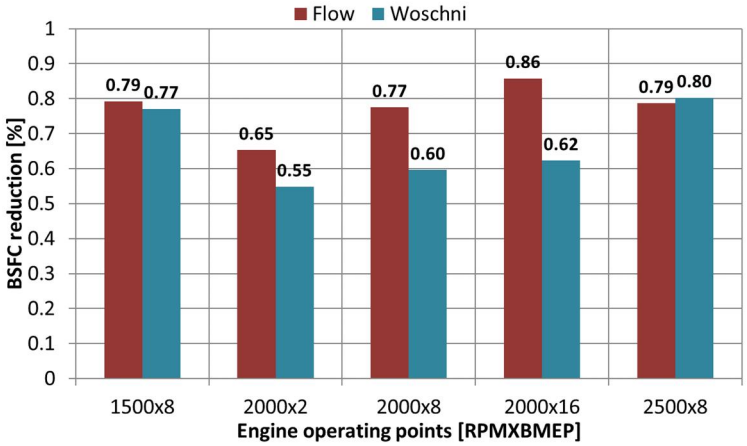

Figure B.3 - BSFC benefits due to piston coating (100 µm - anodized aluminum) using Flow and Woschni models

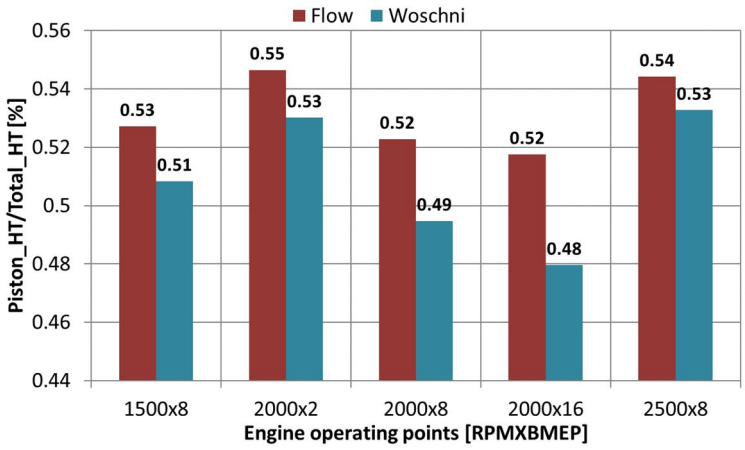

Figure B.4 - Fraction of the piston heat loss respect to the total for the baseline condition